8-2014

Mechanical Properties of Low Dimensional Materials

Deepika Saini
Clemson University, dsaini@g.clemson.edu

MECHANICAL PROPERTIES OF LOW DIMENSIONAL MATERIALS

A Dissertation
Presented to
the Graduate School of
Clemson University

In Partial Fulfillment
of the Requirements for the Degree
Doctor of Philosophy
Physics and Astrophysics

---

by
Deepika Saini
August 2014

Accepted by:
Dr. Apparao M. Rao, Committee Chair
Dr. Malcolm J. Skove
Dr. Dieter H. Hartmann
Dr. Timothy A. DeVol
Dr. Steven M. Serkiz

ABSTRACT

Recent advances in low dimensional materials (LDMs) have paved the way for unprecedented technological advancements. The drive to reduce the dimensions of electronics has compelled researchers to devise newer techniques to not only synthesize novel materials, but also tailor their properties. Although micro and nanomaterials have shown phenomenal electronic properties, their mechanical robustness and a thorough understanding of their structure-property relationship are critical for their use in practical applications. However, the challenges in probing these mechanical properties dramatically increase as their dimensions shrink, rendering the commonly used techniques inadequate. This dissertation focuses on developing techniques for accurate determination of elastic modulus of LDMs and their mechanical responses under tensile and shear stresses.

Fibers with micron-sized diameters continuously undergo tensile and shear deformations through many phases of their processing and applications. Significant attention has been given to their tensile response and their structure-tensile properties relations are well understood, but the same cannot be said about their shear responses or the structure-shear properties. This is partly due to the lack of appropriate instruments that are capable of performing direct shear measurements. In an attempt to fill this void, this dissertation describes the design of an inexpensive tabletop instrument, referred to as the *twister*, which can measure the shear modulus (G) and other longitudinal shear properties of micron-sized individual fibers. An automated system applies a pre-determined twist to

the fiber sample and measures the resulting torque using a sensitive optical detector. The accuracy of the instrument was verified by measuring *G* for high purity copper and tungsten fibers. Two industrially important fibers, IM7 carbon fiber and Kevlar® 119, were found to have *G* = 17 and 2.4 GPa, respectively. In addition to measuring the shear properties directly on a single strand of fiber, the technique was automated to allow hysteresis, creep and fatigue studies.

Zinc oxide (ZnO) semiconducting nanostructures are well known for their piezoelectric properties and are being integrated into several nanoelectro-mechanical (NEMS) devices. In spite of numerous studies on the mechanical response of ZnO nanostructures, there is not a consensus in its measured bending modulus (*E*). In this dissertation, by employing an all-electrical *Harmonic Detection of Resonance* (HDR) technique on ZnO nanowhisker (NW) resonators, the underlying origin for electrically-induced mechanical oscillations in a ZnO NW was elucidated. Based on visual detection and electrical measurement of mechanical resonances under a scanning electron microscope (SEM), it was shown that the use of an electron beam as a resonance detection tool alters the intrinsic electrical character of the ZnO NW and makes it difficult to identify the source of the charge necessary for the electrostatic actuation. A systematic study of the amplitude of electrically actuated as-grown and gold-coated ZnO NWs in the presence (absence) of an electron beam using an SEM (dark-field optical microscope) suggests that the oscillations seen in our ZnO NWs are due to intrinsic static charges.

In experiments involving mechanical resonances of micro and nanostructured resonators, HDR is a tool for detecting transverse resonances and *E* of the cantilever material. To add to this HDR capability, a novel method of measuring the *G* using HDR is presented. We used a helically coiled carbon nanowire (HCNW) in singly-clamped cantilever configuration and analyzed the complex (transverse and longitudinal) resonance behavior of the nonlinear geometry. Accordingly, a synergistic protocol was developed which (i) integrated *analytical*, *numerical* (i.e., finite element using COMSOL ®) and *experimental* (HDR) methods to obtain an empirically validated closed form expression for the *G* and resonance frequency of a singly-clamped HCNW, and (ii) provided an alternative for solving 12^{th} order differential equations. A visual detection of resonances (using *in situ* SEM) combined with HDR revealed intriguing non-planar resonance modes at much lower driving forces relative to those needed for linear carbon nanotube cantilevers. Interestingly, despite the presence of mechanical and geometrical nonlinearities in the HCNW resonance behavior, the ratio of the first two transverse modes f_2/f_1 was found to be similar to the ratio predicted by the Euler-Bernoulli theorem for linear cantilevers.

DEDICATION

I dedicate my work to my parents, Raj and Surinder Saini, and brother, Sahil Saini, for their unconditional love and incredible support throughout my PhD. I also dedicate this to my fiancée, Arijit Mitra, and his parents for being so understanding and believing in me. I take this opportunity to extend my sincere gratitude towards all my family and friends for their encouragement and guidance.

ACKNOWLEDGMENTS

I am grateful to my advisor Dr. Apparao M. Rao, for giving me this invaluable opportunity to work in his research group. His constant guidance, motivation and relentless patience were instrumental in the progress of my graduate studies. He encouraged me to be an independent thinker and grow as a researcher. He is indeed my greatest inspiration, and I thank him for making my PhD an incredible learning experience.

Completing this dissertation work would have been impossible without Dr. Malcolm J. Skove. He often looked-over-my-shoulders through my projects, and his wisdom and knowledge has undoubtedly enriched my PhD experience. He was always available for answering my questions and discussing new ideas. I thank Dr. Steven M. Serkiz for his encouragement and support which enabled me to work on several exciting projects, many of which will be published in peer-reviewed journals. I also express my gratitude to Drs. Dieter Hartmann and Timothy DeVol, for their advice and discussions which have enhanced the quality of this dissertation.

I would like to take this opportunity to thank Lamar, Jonathan and Barrett for their timely assistance at the machine shop. Many of my projects would not have completed without the components they built. I extend my gratitude to Dr. Terry Tritt for allowing me to work on the SEM in his lab, and members of the electron microscope facility, especially

Dr. Taghi Darroudi and Dr. Haijun Qian for their help in operating the electron microscope.

I would not have completed this dissertation without the support of my colleagues: Dr. Ramakrishna Podila whose guidance and constant motivation helped me sharpen my skills, organize my PhD and sort my career goals, Herbert Behlow for designing the instrumentation, assisting me through the late night HDR experiments and data analysis, Dr. Jay Gaillard for introducing me to the HDR technique, Dr. Pooja Puneet for helping me with the SEM 3400, and my lab mates at the Clemson Nanomaterial Centre (Mehmet, Jingyi, Luciana, Kiran, Ted, Anthony, Fengjiao, Sunil, Achyut, Yong-chang and Bishwambhar) for their support.

I am thankful to Sigma –Xi Research Society and American Physical Society for their generous fellowships awarded during my graduate studies.

Finally I would like to thank all my friends in India and US for their support and encouragement. Particularly, I would like to thank Harshad, Akash, Priyanka, Satish, Aman, Aesha and her parents, Keyur, Tanzeel, Misha and Anirudh who made my stay in Clemson truly memorable.

TABLE OF CONTENTS

Page

Table of Contents (Continued) Page

LIST OF TABLES

LIST OF FIGURES

List of Figures (Continued)

Figure Page

List of Figures (Continued)

Figure Page

List of Figures (Continued)

Figure Page

List of Figures (Continued)

Figure Page

List of Figures (Continued)

Figure Page

List of Figures (Continued)

Figure Page

List of Figures (Continued)

Figure Page

CHAPTER 1

INTRODUCTION

As Richard Feynman had foreseen in his famous 1959 lecture, scientists have discovered that there indeed is “plenty of room at the bottom.” The advent of micro and nanotechnology has virtually revolutionized the scientific ideologies and methods. Researchers since then have discovered the enormous potential of low-dimensional materials both in fundamental science and technological applications. The effect is tangible in the fields of energy storage, biomedical research, homeland security, wireless communication and artificial intelligence. The superior properties and unique applications of these smart materials have created unparalleled synergy between previously independent fields of science. The technological achievements have reached new milestones, radically advancing the society.

1.1 Low Dimensional Materials: Brief Introduction

Materials with at least one physical dimension in the scale of micro/nanometers, intermediate between atomic and bulk, are referred to as low- dimensional materials (LDMs). The interest in size reduction burgeoned with the advent of sophisticated lithographic and micro fabrication techniques. Micromachining and fabricating integrated circuitry (IC) in silicon became a reality, drastically reducing the size of electronics. The past fifteen years has seen an outstanding progression in the capabilities of conceiving

extremely complex structures and operational devices.[1] Often movable, a variety of these structures, including cantilever beams, gears and suspensions can perform complex mechanical and analytical functions with high precision. Their reduced size, improved performance and diverse functionalities have led to intriguing innovations.[2, 3] Through their lab-on-chip ability, these microelectro-mechanical entities (MEMS) have miniaturized the current technology. They form an integral part of the existing world of smart gadgets and superfast computers, and are the "brains" in many of the 21st century's advanced systems[4] including unmanned aerial and ground vehicles, robots and non-destructive evaluation devices.

In conjunction with MEMS which are typically top down devices, high performance micro fibers (diameter ~1-100 μm) similarly have demonstrated extraordinary capabilities. Generally synthesized using bottom up approaches, their light weight and ultrahigh strength have lent a pronounced robustness to many macro devices and instruments. These thin highly flexible filaments can be bundled or woven to a desired shape or form. Carbon fibers (CF) such as IM7 and organic fibers (including Kevlar® and spider silk) have marked their niche and can now be found in energy storage applications[5], flexible electronics[6] and composite reinforcements[7]. In fact, CF has been successfully used in spacecraft components and many other aerospace application([8] and references therein). They not only reduce the effective weight of these machines but simplify their maintenance. Their strength has also been exploited in

defense for ballistic impact protection and surveillance drones. Microfiber properties have been tailored for highly specific chemical purification and water filtration.

The nanoscale regime (typically 1 - 100 nm) also offers a myriad of fascinating morphologies, intriguing phenomena and extraordinary properties. Geometries of the nanomaterials can vary from simple linear (for eg. multiwalled nanotubes or nanowires) to complex non-linear (for eg. coiled carbon nanotubes, Y-junctions nanotubes and tetrapods). A few such geometries are shown in Fig. 1.1.

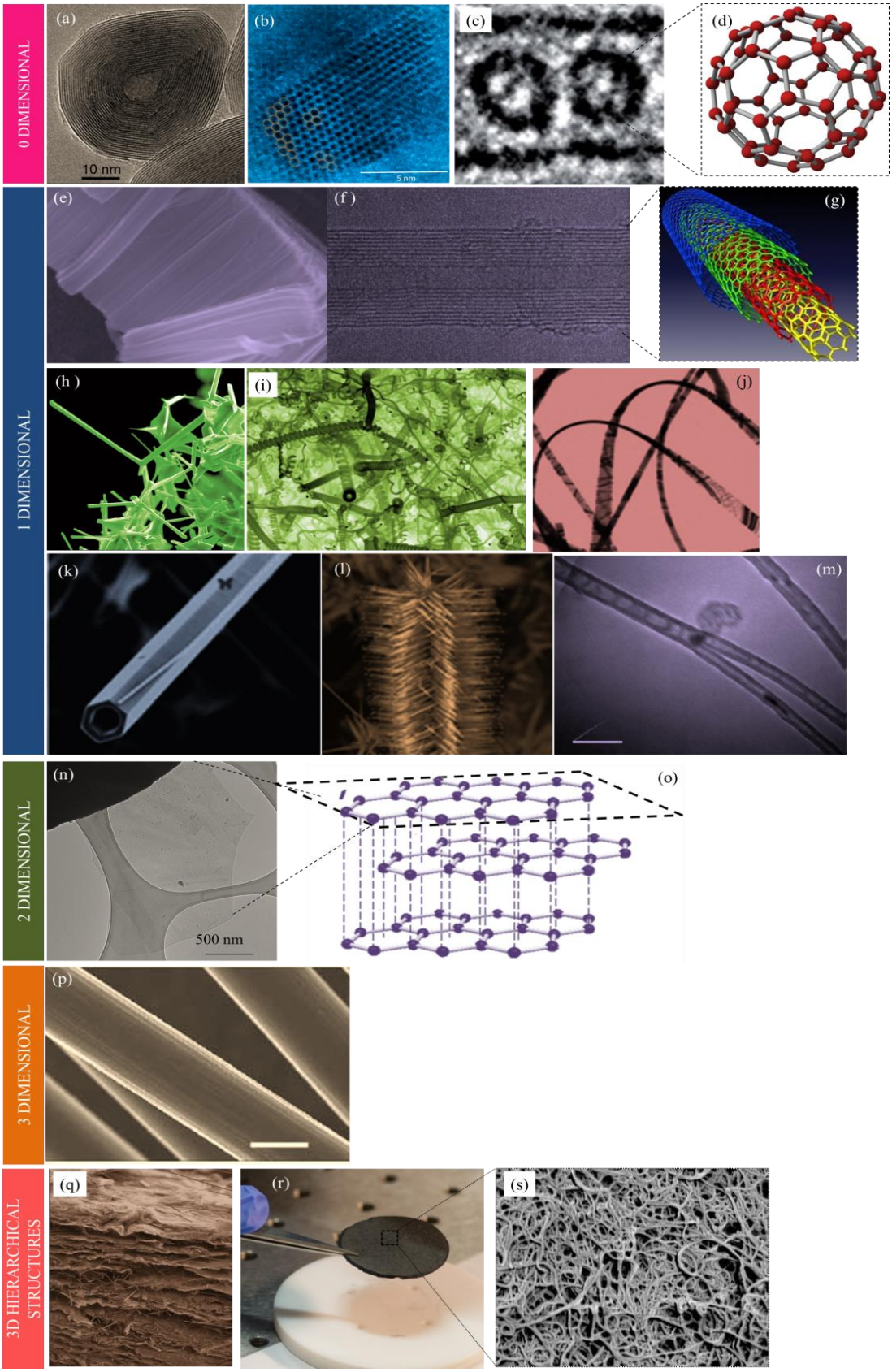
0 DIMENSIONAL
1 DIMENSIONAL
2 DIMENSIONAL
3 DIMENSIONAL
3D HIERARCHICAL STRUCTURES
(a)
10 nm
(b)
5 nm
(c)
(d)
(e)
(f)
(g)
(h)
(i)
(j)
(k)
(l)
(m)
(n)
500 nm
(o)
(p)
(q)
(r)
(s)

Figure 1.1 Examples of some morphologies of low dimensional materials. *Zero dimensional* (0D) (a) MoS_2 fullerene having onion-like structure (TEM),[9] (b) graphene quantum dot (HRTEM) in which the hexagonal arrangement of the carbon atoms is visible[10], (c) Buckminster fullerene carbon (C_{60}) molecules (TEM) are closed molecules of 60 or more carbon atoms exhibiting a truncated icosahedron structure; model shown in (d),[11] *One dimensional* (1D) (e) SEM image of as grown vertically aligned carbon nanotubes (CNTs) (f) Concentric shells of a multiwalled CNT (MWCNT) (TEM) (g) A schematic drawing of a MWCNT (h) Four pronged tetragonal Zinc oxide (ZnO) nanostructure (SEM) (i) helically coiled carbon nanowires (HCNWs) (SEM)[12] (j) ZnO nanobelts (SEM)[13] (k) ZnO nanowires (SEM)[13] (l) comb like ZnO (SEM)[13], (m) Y-junction carbon nanotubes (SEM)[14]. *2 Dimensional* (2D) (n) SEM image of a single layer graphene sheet with its schematic as seen in (o). *3Dimensional* (p) micron size IM7 carbon fibers (CF) (SEM). *3Dimensional* (3D)*hierarchical* CNT and CF can be self-assembled to synthesize macrostructures that possess the qualities of its components (q) SEM image of a buckysponge made from CNT and CF (r) optical image of a buckypaper made from self-assembled CNTs. (s) SEM image of the top surface of the buckypaper. SEM: Scanning electron microscope; (HR)TEM: (High- resolution) transmission electron microscope.

Although the study of nanomaterials can be traced back centuries, it was mostly the advent of electron microscopes, state-of-the-art spectroscopes and the drive to continuously shrink semiconductor devices that gave nanoscience its current-scientific interest. Nanomaterials are not just reduced forms of bulk materials, but are often fundamentally different physical systems. As the material size is reduced towards the atomic scale, small enough to confine only a few electrons or phonons, the fraction of surface atoms in comparison with the bulk atoms considerably increases. Consequently, these materials have very a high surface area. Different coordination number and unsatisfied bonds at the surface atoms induces a scaling effect in its properties such as its boiling point. On the other hand, quantum confinement of electrons alters the density of states and thus varies its band gap energies. A similar effect has been found in layered metal dichalcogenides. [15, 16] Exfoliating them into a few layers or single layer 2D systems transforms them from an indirect to a direct band gap material. Nanoscience has also provided us the world's stiffest material, the sp^2 hybridized carbon nanotubes (CNTs).[17] This amazing robustness is solely due to its chemical bond nature. However, in general, LDMs are found to exhibit enhanced mechanical properties partly due to lower point defect density, dislocations and grain boundaries. Their distinct band structures result in improved electrical conductivity and high charge mobility.[18, 19] These promising electrical properties have been leveraged to devise high performance electronics including transistors[20], switches[21] and even superconductors[22].

These enhanced electrical and mechanical functionalities have made them ideal for use in nanoelectro-mechanical (NEMS) devices, a natural and logical step towards miniaturization of MEMS. Materials such as carbon nanotubes and ZnO nanowires have been implemented into sensors[23], power generators[24], memory storage[25] and advanced nanorobotic applications.[26] The next section briefly introduces cantilevered electromechanical devices and the pronounced advantages of using LDMs as cantilevered NEMS/MEMS structures.

1.2 Cantilevers as Resonators

Cantilevers can arguably be called one of the most popularly applied mechanical structures. It is thus not surprising that these structures are deep rooted in the realm of MEMS and NEMS. Their small size allows for unprecedented sensitivity to environmental parameters including temperature[27, 28], pressure[29], and humidity[27], and improved dynamic performance. By coating the cantilevers with a thin chemically selective receptor layer, they can be made to respond selectively to specific chemical and biological species[30]. This response has been extensively utilized to detect low levels of contaminants in fluids[31], and to sense the dew point[32] and lubricity of a fluid.[33] Recently, many MEMS/NEMS applications in bio-sensing [34-36] and bio-medical[37-40] have garnered significant attention. The sensitivity of micro/nanocantilevered structures has been explored with cantilevered systems used successfully to detect mass as low as a few zeptograms (10^{-21} g). [41] Inducing differential stress through selective

coating is a sensitive technique enabling high selectivity and using the ambient pressure to manipulate the quality factor (full width half maximum of the power spectrum; *Q-factor*) of the mechanical resonance is also highly useful. These features make micro and nanocantilevers ideal candidates for a wide variety of sensing applications and attractive alternatives to traditional sensing technologies. Microcantilevers generally consist of lithographically fabricated monolithic cantilevers (commercially available cantilevers are typically ~ 300 μm x 25 μm x 2 μm) or clamped microfibers. Fabricating nanocantilevers is highly challenging due to large surface stresses. Hence, high aspect ratio nanomaterials such as carbon nanotubes or nanowires are used are cantilevers. As an added advantage, bottom up nanomaterials have fewer defects[42], and their different chemical structures offer varied mechanical properties.

While the optical detection of mechanical oscillations has proven useful for determining motion in microcantilevers, the reflected beam intensity is insufficient for nano-sized cantilevers. To address this problem, MEMS and NEMS systems employ electrical detection of mechanical motion at a very small scale. From an application viewpoint, the electrical detection of motion, such as a capacitive readout of the mechanical motion, is highly desirable because it can be readily integrated with NEMS devices that are fully compliant with standard complementary metal oxide semiconductor (CMOS) technologies.

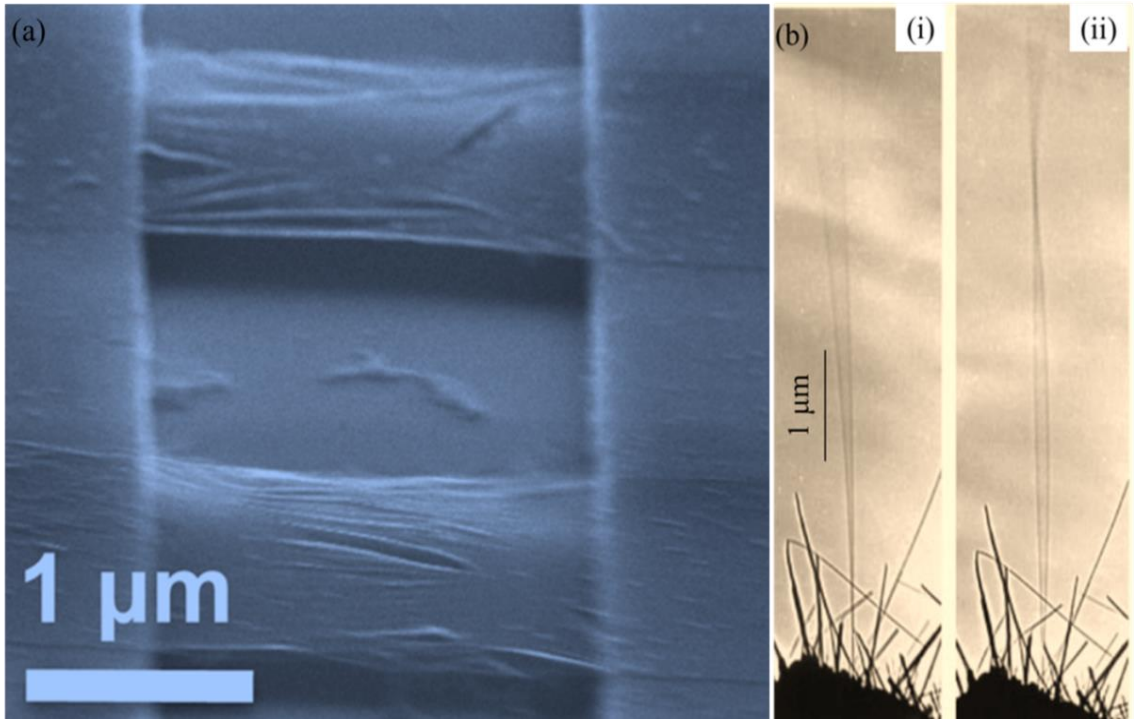

Figure 1.2: Various LDMs may be used as cantilevered structures to probe their mechanical properties (a) A doubly clamped (guitar like) single carbon atomic thick layer graphene sheet[43] across a trench (b) The first (i) and second (ii) transverse resonance modes of a singly-clamped (diving board like) CNT. [44]

Sazonova *et al.*[45] electrically actuated and measured the resonant frequency of a doubly-clamped single-walled carbon nanotube (SWCNT) using a mixer technique, which is based on the CNT's transistor properties. Although valuable for a beam in a doubly clamped guitar-string like configuration, the mixer technique cannot be applied to a singly-clamped cantilevered nanostructure. Alternatively, a technique for detecting nanoscale displacements has been demonstrated using a single electron transistor[46]. However, this device operates at low temperatures (30 mK) and in a relatively high

magnetic field (8T). Electrically induced mechanical oscillations in multi-walled carbon nanotubes (MWCNTs) have also been recorded using non-electrical detection methods that utilized a transmission electron microscope (TEM), [44] scanning electron microscope,[47] field emission microscope[48] or an optical microscope.[49] For use in practical applications, however, the resonating system must be portable, and therefore a capacitive readout of the mechanical motion as described above for microcantilevers may be preferable to other techniques.

In the following section commonly used actuation (input signal → mechanical response) and detection (mechanical response → output signal) techniques that are applicable to both the "diving board" singly clamped cantilevers and the "bridged" doubly clamped cantilevers are discussed. It will also be established that the Harmonic Detection Resonance (HDR), see section 1.5 for details, method may be useful, for both organic and inorganic materials (as referenced above) for detecting oscillations in nano-sized cantilevers.

1.3 Actuation Techniques

Of the various transduction mechanisms that result in a mechanical motion of the cantilever, three popular techniques are discussed below.

1.3.1 *Piezoelectric:* One of the most extensively applied techniques entails the use of a piezoelectric material that generates a mechanical strain when subjected to an electric

field. This method is used in two geometries. Either the cantilever may be driven by an external piezoactuator mounted close to it or for more control, a thin layer of suitable piezoelectric material, e.g. lead zirconium titanate is deposited on the cantilever. Upon the application of an electric field, the piezoelectric film either expands or contracts, which in turn bends the cantilever. Piezoactuation is notably used in atomic force microscopy (AFM) and is used for both static and dynamic deflection modes. Similar actuators are also used in inkjet systems [50, 51] and disk readers. Though this is an efficient transduction method, the post process deposition of the piezoelectric layers makes it complicated and costly for mass production.

1.3.2 *Electrostatic:* The electrostatic actuation mechanism is based on Coulomb's law, from which it follows that two oppositely charged elements will experience an attractive force. In this method, an alternating potential difference is applied across a conducting microcantilever and counter-electrode (CE) resulting in an attractive electro(quasi)static force. In response to this force, the cantilever deflects. This actuation mechanism, which is the desirable technique for applications demanding high forces for small displacements, is quite common, efficient and straightforward to fabricate[52]. If the elements are modeled as a parallel plate capacitor, the electrostatic force, F_E, is given by Equation 1.1

$$F_E = \frac{\varepsilon A V^2}{2d^2} \qquad (1.1),$$

where ε is the permittivity of the medium separating the electrodes, A is the plate area, V is the applied voltage, and d is the separation distance. Continuing efforts have been made to develop the applicability and efficiency of this technology, such as either reducing the applied voltage, [53] or increasing the frequency.[54]

1.3.3 *Magnetic:* A current carrying element placed in a magnetic field experiences a Lorentz force in a direction perpendicular to both the current and magnetic fields. This mechanism is the basis for magnetic force microscopy and scanning hall probe microscopy. [55] Also, a magnetic micro-actuator has been developed that utilizes an electroplated permalloy that possesses a high magnetic permeability. [56] However, the limited number of magnetic materials compatible with existing micro-manufacturing processes, and only planar coils, make it difficult to generate magnetic fields on a chip; thus the applicability of the magnetic transduction to MEMS and NEMS has been somewhat limited.

In addition to the above mentioned techniques, a cantilever may also be actuated through the radiation pressure from an optical source to induce resonance. [57] An electro-thermal actuation[58] method was also developed that is based on the heat produced by electric current when it is passed through a cantilever, which in turn bends the cantilever, similar to a bimetallic effect, owing to the different expansion coefficients of two different materials.

1.4 Detection Mechanisms

Detection involves converting either the static deflection or the dynamic response of the cantilever into a useful output signal, which usually is electrical in nature. The dynamic response may include shifts in the natural resonance frequency, changes in vibrational amplitude (A) and phase (ϕ), or changes in *Q-factor*.

1.4.1 *Optical*: A laser beam is employed to optically detect the motion of the cantilever surface. There are two common methods for such detection:

a) Laser Beam Deflection: A laser spot is focused on the cantilever and the reflected beam is directed to a position on the photo-detector, which acts as a position sensitive device (PSD). The beam spot is deflected while resonating and is detected by the PSD to calculate the frequency and other parameters.

b) Interferometric Detection: This optical detection system utilizes the sensitivity of interferometry between the incident and reflected beams. An optical beam illuminates the reverse side of the cantilever. The reflected light and the incident light form an interference pattern which is focused on a PSD. When the cantilever actuates, the interference pattern shifts, which used to calculate the displacement, resonance frequency, and force. Various types of interferometer, such as homodyne,[59, 60]or heterodyne,[61, 62] may be used. Though interferometry can measure a deflection in 1 pm range, positioning the optical elements is difficult.

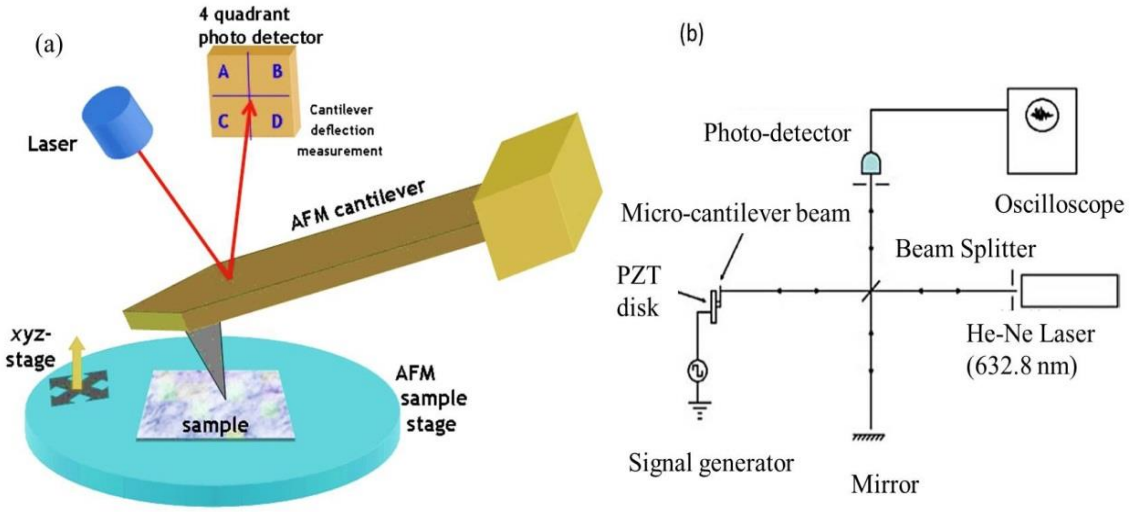

Figure 1.3: Laser Beam Deflection configuration to detect the motion of the micro cantilever: (a) A laser beam is focused on the cantilever surface with the reflected beam directed on a position sensitive photo detector.[63] (b) Interferometer used to detect the resonance of a cantilever.[64]

1.4.2 *Piezoelectric/piezoresistive:* Piezoresistance is the change in resistivity of a material with applied stress. This variation of resistivity can be used to detect the deflection of micro-cantilevers. The intrinsic piezoresistivity of silicon can be enhanced by doping, making piezoresistive detection highly compatible with CMOS processes. Piezoresistive elements are typically placed at the base of the cantilever where the stresses from bending are greatest, and are usually arranged in a Wheatstone bridge configuration in order to negate such common mode effects as thermal variations.[30]

1.4.3 *Capacitive*: This detection method is based on the principle of the change in capacitance between a resonating cantilever and a CE in proximity. As the cantilever deflects, the capacitance of the arrangement varies, causing charge to either move on or off the cantilever as a function of the oscillating displacement.[65] If this charge or current can be measured, the mechanical vibration of the microcantilever can be inferred. The capacitive detection method avoids the need for an optical system and its associated alignment requirements. Additionally, cantilevers suitable for capacitive detection do not require some of the elaborate fabrication steps generally pertaining to piezoresistive detection elements. These advantages make it a versatile technique.

Though electrostatic actuation is easy to implement, conventional capacitive detection has proven difficult, mostly because of the parasitic signal that obscures the dynamic signal from the resonating cantilever. This parasitic signal includes both the static capacitance of the microcantilever and CE and all the stray capacitance of nearby circuit elements. Several methods have been proposed to enhance the dynamic capacitance or lower the parasitic capacitance of the system, such as the use of single electron transistors, [66] and controlling the direct wafer bond line width[67] and the use of comb drives. [68, 69] Also, since the ratio of dynamic to parasitic signal depends on the ratio of cantilever deflection to total gap distance, attempts have been made to minimize the parasitic effects by positioning cantilevers extremely close to the CEs. In addition to the pull-in problems imposed by designs with a small gap distance, each of these solutions increases the complexity, cost of production, and potential for device malfunction or

failure. However, there are two methods that allow a sensitive electrical detection of resonance signal. The first method discussed in section 1.5 is the HDR method that is based on continuous driving of cantilever and performs the detection at a higher harmonic of the driving frequency. The second method discussed in section 1.6 is based on transient motion of a resonating cantilever and monitors the ring down of the cantilever once the driving force has been removed. The advantages and applications of both these methods are briefly discussed in the respective sections.

1.5 Continuously Driven: HDR

HDR is a capacitive detection method that was developed to avoid the parasitic capacitance without significantly increasing the complexity of the device. The nonlinear electrostatic force on the cantilever from a nearby CE induces a rich harmonic structure in the resulting electrical signal from the cantilever.[70] These higher harmonic signals, integral multiples of the driving frequency, do not suffer from significant parasitic effects. Hence, by measuring the dynamic response of microcantilevers at these harmonic frequencies, it is possible to obtain significantly higher signal-to-background ratios (*SBR*) and *Q-factors*, resulting in a greatly improved sensitivity in HDR based sensing devices. In that HDR is a completely electrical actuation and detection scheme, it is directly scalable to micro- and nano-devices with a straightforward integration into standard micro-lithographic processes. This scalability allows for simple portable HDR based sensing devices that require no complicated components, such as lasers, magnets or

piezoelectric elements. Consequently, it reduces the cost and makes the device highly reliable. HDR does require circuitry to detect the higher harmonics, but this should be possible to realize on a single chip. In addition, the possible gap distances over which HDR is applicable are relatively high, allowing for precise alignment, higher stability and voltage control. The HDR scheme meets these requirements and provides several unique advantages not present in other detection techniques.

1.5.1 Experimental Set up

A typical HDR assembly consists of a pre-amplifier, a signal generator, a dc power supply, and a lock-in amplifier (details later in the section), Fig. (1.4). Here, a cantilever (micro or nano) was manipulated over an optical dark-field microscope to position it near the CE (an electrochemically etched tungsten tip; W-tip) obviating the need for time consuming lithographic processes.

Depending on its dimensions, the cantilever is placed parallel to and within 1–10 μm from the CE. An electrostatic force is generated by applying an ac peak voltage, V_{ac} (to induce periodic motion), with a dc offset, V_{dc} (to overcome work potentials). To avoid a zero crossing in the net excitation voltage ($V_{net} = V_{ac}+V_{dc}$), V_{dc} is maintained at values higher than V_{ac}. The experiments can be performed under ambient conditions, demonstrating that HDR does not require any elaborate apparatus to control temperature or pressure.

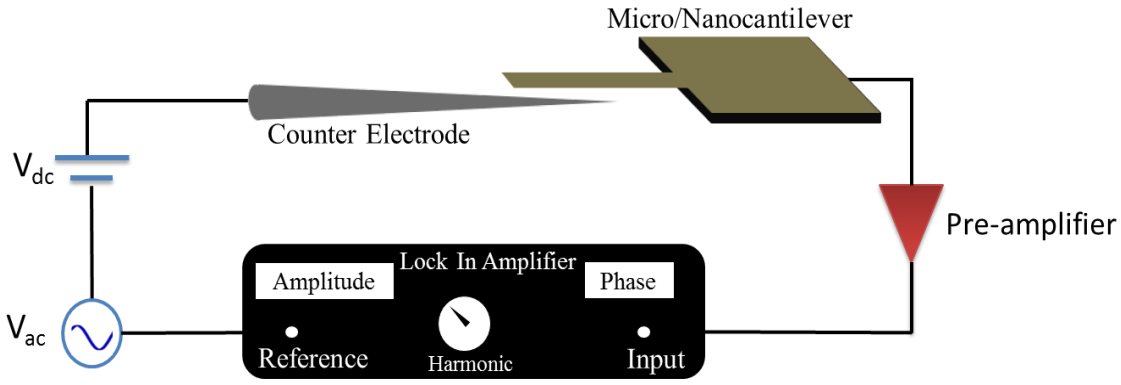

Figure 1.4: A schematic of the HDR experiment. The driving signal consists of a tunable frequency ac signal (V_{ac}) with a dc (V_{dc}) offset. The tungsten tip (W-tip) counter electrode (CE) actuates the micro/nanocantilevers to resonance. The signal from the resonating cantilever is amplified using a pre-amplifier. This amplified signal reaches the lock-in amplifier which detects it at higher harmonics. HDR allows the detection without using any optical elements.[71]

In order to minimize the crosstalk between the metal contacts holding the cantilever and counter electrode, a Faraday cage is used, which surrounds the metal contact for the CE and extends around the probe tip leaving about 2 mm of the tip exposed. This helps increase the *SBR*, a noise reduction consideration that is crucial when working at the nanoscale. The lock-in amplifier detects the output of the pre-amplifier, which is proportional to the current, at a harmonic (integer multiple) of the oscillator driving frequency, Ω.

It is worthwhile to briefly describe the operation of lock-in amplifiers since they are such an integral component of the HDR detection system. Lock-in amplifiers are electronic instruments capable of extracting extremely small signals of known frequency from otherwise noisy signals. For this reason they are ideally suited for measuring the higher harmonic components which can be many orders of magnitude smaller than the first harmonic of the cantilever's electrical response. In lock-in amplifiers the reference frequency signal, in this case the driving frequency $V_{\text{ref}}\cos(\Omega t)$, is mixed with (multiplied by) the output signal from the cantilever, $V_{\text{in}}(t)$, (Equation 1.2) and averaged over many periods of the reference frequency. If the signal from the cantilever has a Fourier component at the reference frequency, the result is proportional to the amplitude of that component. The input signal is also multiplied by $V_{\text{ref}}\sin(\Omega t)$ so that both the phase and amplitude of the input signal can be determined. If the reference frequency is set to a multiple of the driving frequency, the amplitude and phase or harmonic components may be determined. The result is a signal that is proportional to the amplitude of a Fourier component of the output signal from the cantilever at the reference frequency.

$$V_{\text{mix}} = V_{\text{in}}(t)\cdot V_{\text{ref}}(t) = V_0\cos(\Omega t)\cos(\Omega t) = \frac{1}{2}V_0\left[1+\cos(2\Omega t)\right] \tag{1.2}$$

The outputs of typical lock-in amplifiers are the quadrature (90^{o} out of phase) components of the input signal at the reference frequency, from which the overall amplitude and phase of the output signal from the cantilever can be determined. Early lock-in amplifiers multiplied the input signal by a square wave reference signal, which

includes many higher harmonics. The availability of lock-in amplifiers, based on digital signal processing (*e.g.*, the Stanford Research Systems Model SR830) which multiplies the input signal by a sinusoidal reference signal, avoids this problem. Consequently, only the amplitude of a single Fourier component of input signal is given, thereby providing more accurate harmonic measurements.[72]

1.5.2 Electrical Response Spectra and Skove plots of resonance

A micro-cantilever exhibits a variety of resonance peaks, which are evident when the amplitudes of the electrical HDR signals are plotted over a wide range of frequencies. The nature of the resonance peaks are often more thoroughly elucidated with an examination of their polar representations, called Skove plots, in which A is plotted versus ϕ with the driving frequency as the parameter. A single-degree-of-freedom oscillator shows a counterclockwise circle. In the HDR polar plots, overlapping curves occur for each resonance peak (primary and super-harmonic) existing in the harmonic spectrum. One such plot for a microcantilever for one of its resonance peaks is shown in Fig 1.6. The resonance frequency may be determined from the polar graph by noting where the phase changes most rapidly. In some cases the polar representation shows that the resonance is no longer circular, but rather is closely approximated by a class of curves known as limaçons.[73] Limaçons result from highly nonlinear systems where two separate terms contribute to the electrical signal, neither of which can be neglected.

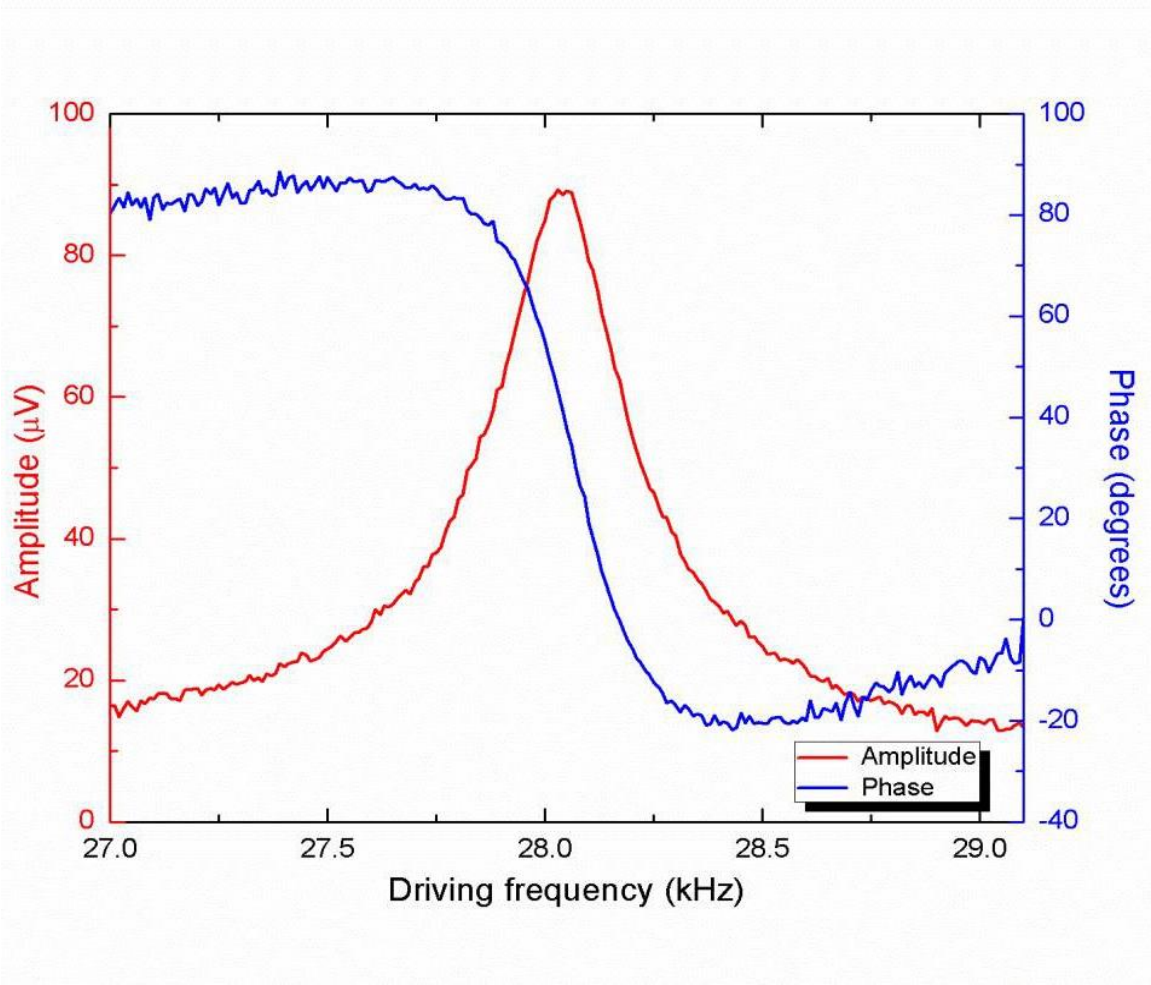

Figure 1.5: A typical amplitude and phase response measured by the HDR system in the second harmonic of the signal near resonance frequency, ω_0, for a silicon microcantilever 300 μm long, 35 μm wide, and 2 μm thick.

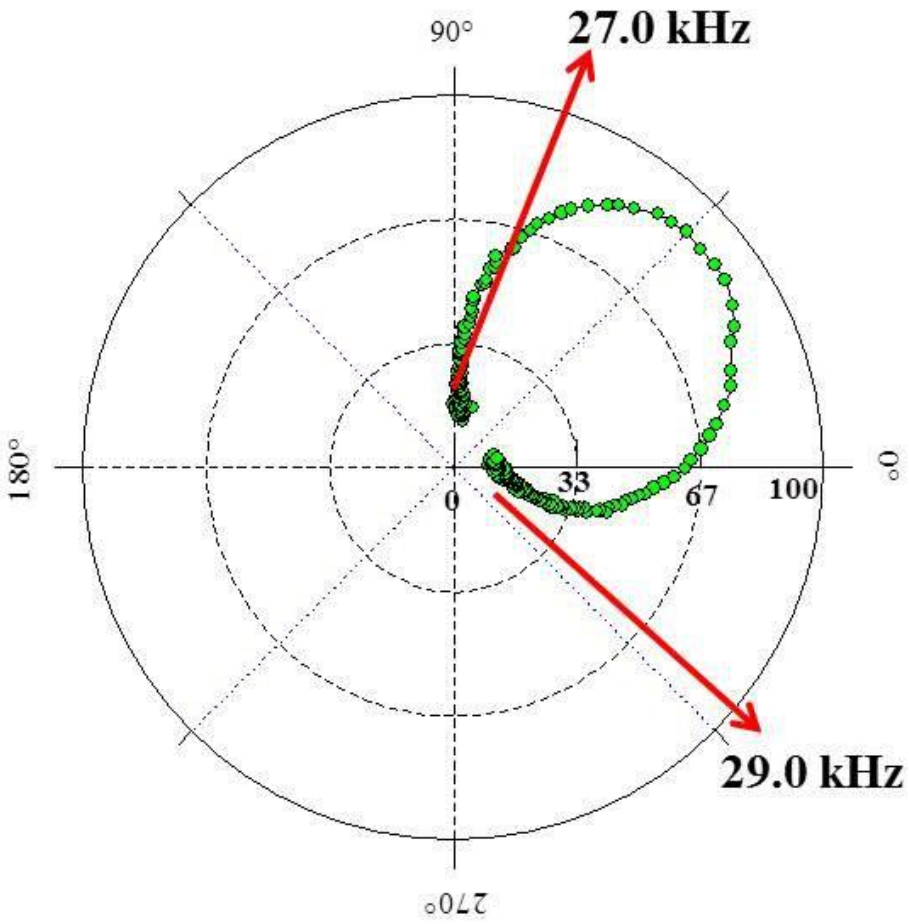

Figure 1.6: Skove (polar) plot of a silicon micro-cantilever corresponding to the signal in Fig. 1.5. The frequency is a parameter, with the beginning and ending frequencies indicated. The plot illustrates the circle that a resonance displays on a Skove plot.

Though the cantilever is a continuous system in which masses and forces are distributed along its length, it can be modeled more simply as a discrete multiple-degree-of-freedom system using classical Euler-Bernoulli beam theory (EB theory) and a classical method known as the Assumed Modes Method[74] for the calculation of the natural vibration frequency of a structure. In this model each mode of vibration is governed by the typical

second order linear differential equation of motion (EOM) of a driven damped harmonic oscillator (Equation 1.3). This model, which applies equally for micro and nanocantilevers assuming they are slender, homogeneous, and isotropic, is expressed as:

$$\left[m\ddot{z}(t) + b\dot{z}(t) + kz(t) = F(t)\right]_m \qquad (1.3)$$

where $z_m(t)$ is the tip deflection of the m^{th} mode. The effective modal parameters: mass, m_m, damping assumed to be linearly dependent on the velocity, b_m, stiffness, k_m, and force, $F_m(t)$.[75]

1.5.3 Modes of Vibration

The mode shapes are the fundamental shapes that a vibrating structure can assume, or equivalently the Eigen functions of its governing equation. All possible motions of a vibrating structure can be decomposed into a sum of these independent mode shapes. Scanning Electron Microscope (SEM) images indicating the first two modes of vibration of a microcantilever beam are shown in Fig. 1.**7**.

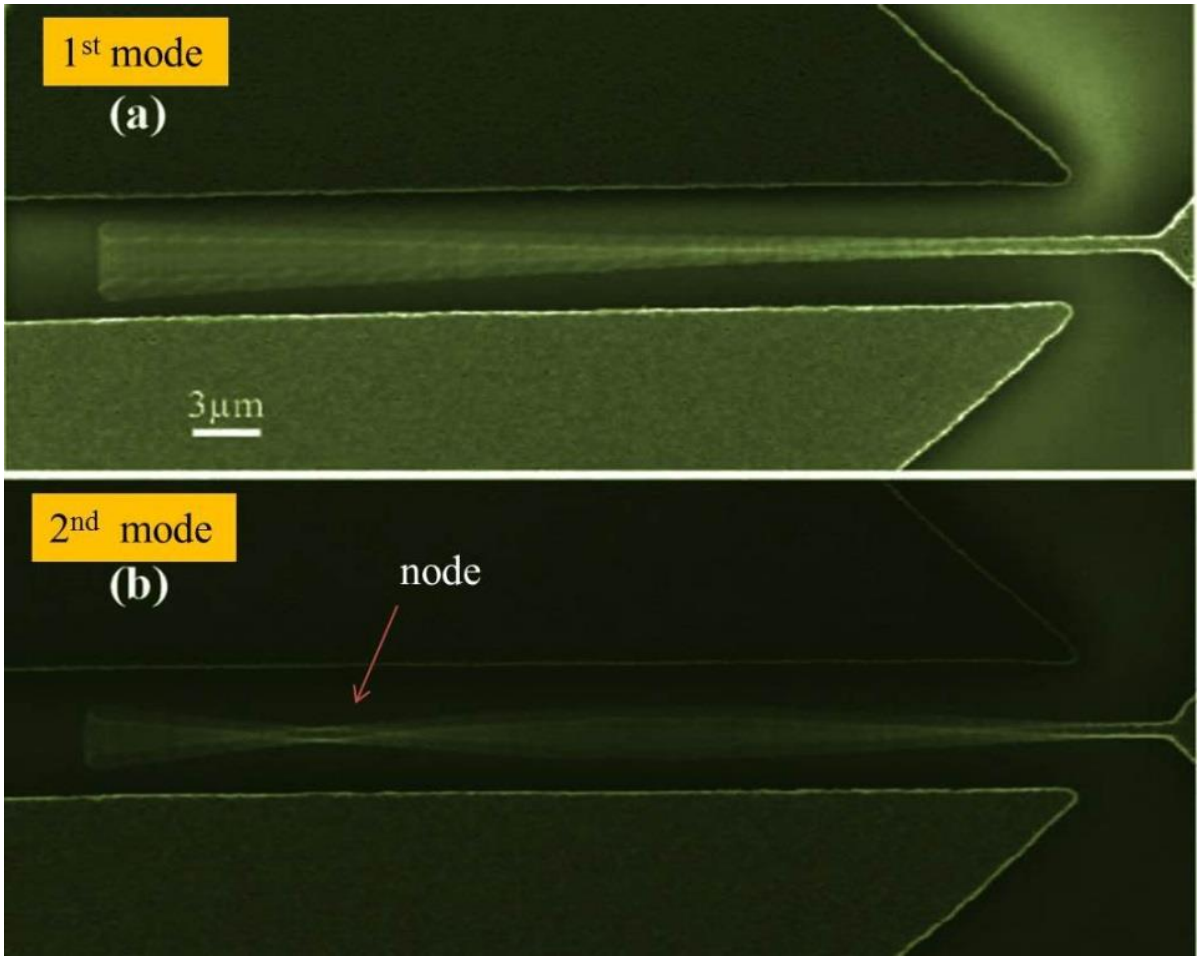

Figure 1.7: SEM images of the same cantilever vibrating at (a) the fundamental mode and (b) the second mode. The dimensions of this cantilever are w = 2 μm, h = 800 nm and l = 40 μm.[76]

Note the distinction between modes and harmonics. Often the term "harmonic", which is defined as being an integer multiple of some fundamental frequency, is confused with the modes of vibration. The confusion arises because for doubly clamped structures, *e.g.*, violin strings, where the frequencies of higher modes of vibration are all integer multiples of the first mode frequency. Thus for doubly clamped systems, harmonic and modal

frequencies are essentially interchangeable. For singly clamped cantilevers, however, the frequencies of the higher modes are *not* integer multiples of the first, and thus the harmonic and modal frequencies are not equivalent.

The natural frequency (ω_m) of the m^{th} mode for a general cantilever of length L is given by Equation 1.4 where E is Young's modulus of the material and ρ is density. For the rectangular cross-sections, *e.g.*, the silicon micro-cantilevers examined in this work, the area moment of inertia (I) is $I = wh^3/12$, and the cross-sectional area is $A = wh$, where w and h are the width and thickness of the cantilever respectively.

$$\omega_m = (\beta_m L)^2 \sqrt{\frac{EI}{\rho A L^4}} \qquad (1.4).$$

Equation 1.4 gives the frequency of the first mode of a singly clamped (cantilever) beam where $\beta_m L = 1.875$ for $m = 1$. As discussed previously, the higher mode frequencies are *not* integer multiples of the first (fundamental) mode and so should not be called harmonics.

This thesis is generally concerned with only the first mode of vibration for several reasons. The first mode has the greatest tip deflection and bends everywhere toward or away from the counter electrode, which facilitates both actuation and detection. In general, the amplitudes of the higher modes are negligible, hence detecting them is

challenging. Finally, the lock-in amplifier used has a limited frequency range; therefore, harmonics of most of the higher modes could not be measured.

1.5.4 LDMs : Ultrasensitive Resonators

Qualitatively, *Q-factor* is a measure of the efficiency of an oscillator and is related to the sharpness of the resonance peak. It is defined, in general, as the ratio of the natural frequency, ω, and bandwidth, $\Delta\omega_{FWHM}$, of the power spectrum (A^2 squared Vs Ω) resonator. For a simple harmonic oscillator, the *Q*-factor is also related to the dimensionless damping ratio, γ_0, as shown in (Equation 1.5) where $\Delta\omega_{FWHM}$ is the bandwidth of the resonance peak.

$$Q - factor = \frac{\omega_0}{\Delta\omega_{FWHM}} = \frac{1}{2\gamma_0} \quad (1.5)$$

In cantilever sensing applications a high *Q-factor* is desirable. Differentiating the fundamental resonant frequency $\omega_0 = (k/m)^{1/2}$, combining with (Equation 1.5), and assuming that the minimum detectable frequency shift is proportional to $\Delta\omega_{FWHM}$, results in (Equation 1.6), in which it is evident that the minimum measurable mass change, $\Delta m_{\min}$, of a cantilever sensor requires both a high *Q-factor* and resonant frequency.

$$\Delta m = \frac{-2k}{\omega_0^{\,3}} \Delta\omega_0 \propto \frac{1}{\omega_0^{\,2} Q} \tag{1.6}$$

Clearly, for increasing the sensitivity of the resonator, a high resonance frequency is desired. Due to their extremely low mass, LDMs can operate at a much higher fundamental frequency and so are highly suitable for ultrasensitive detection.

1.5.5 Nonlinearity and Duffing-like Effects

A characteristic feature of many MEMS devices of recent research interest is the nonlinear response to ac driving signals.[77] It has been postulated that nonlinear spectral features may allow for a greater dynamic range and enhance the sensitivity.[78] While studying the behavior of electrostatically driven and measured cantilevers, it was noticed that it is possible to drive them hard enough to observe Duffing-like jumps in their amplitude-frequency behavior.[79] Duffing-like behavior provides the ability to engineer the ultra-high-sensitivity of this bi-stability.[80, 81] Typically in a Duffing resonator, above some critical driving amplitude, the response becomes a multi-valued function of frequency in some finite frequency range. The presence of a bi-stable region results in a dramatic jump transition from a near-zero solution to that of high amplitude, perhaps useful in sensing technologies.[82] Nonlinearity effects on resonance are often described using the classical Duffing equation [83], given by

$$\ddot{z} + \omega_o^2 z = -2\varepsilon\gamma_0 \dot{z} - \varepsilon\alpha_0 z^3 + F_{\mathrm{E}}(t) \qquad (1.7),$$

where ε is a small parameter, F_{E} is an externally applied force, γ_0 is the positive viscous damping, ω_{o} is the resonant frequency, and α_0 can be either a positive (spring hardening) or a negative (spring softening) constant. The externally applied force is typically sinusoidal, (Equation 1.8),

$$F_{\mathrm{E}}(t) = K\cos\Omega t \qquad (1.8),$$

where K is a constant.

The response curves for the cantilevers have two stable states in some frequency range caused by nonlinearities which lead to the so-called "jump" phenomena. When the driving frequency is slowly increased at constant amplitude, the response amplitude will jump up at a frequency less than the ω_0 that is measured at low amplitude. The response amplitude will also jump to a frequency lower than ω_0 when the frequency is decreased from well above ω_0. The "hardening" and "softening" of springs occurs in which the dynamic spring constant $k_{\mathrm{d}} = dF_E/dz$ either increases or decreases as z increases. For spring hardening, the resonance curve bends toward the higher frequency. For spring softening, such as in the experiments described here, the resonance peak bends toward lower frequencies. For a given frequency, at which two stable steady-state solutions exist, the initial conditions determine which of these represents the actual response of the

system. Thus, in contrast with linear systems, the steady-state solution of a nonlinear system depends upon the initial conditions. [84]

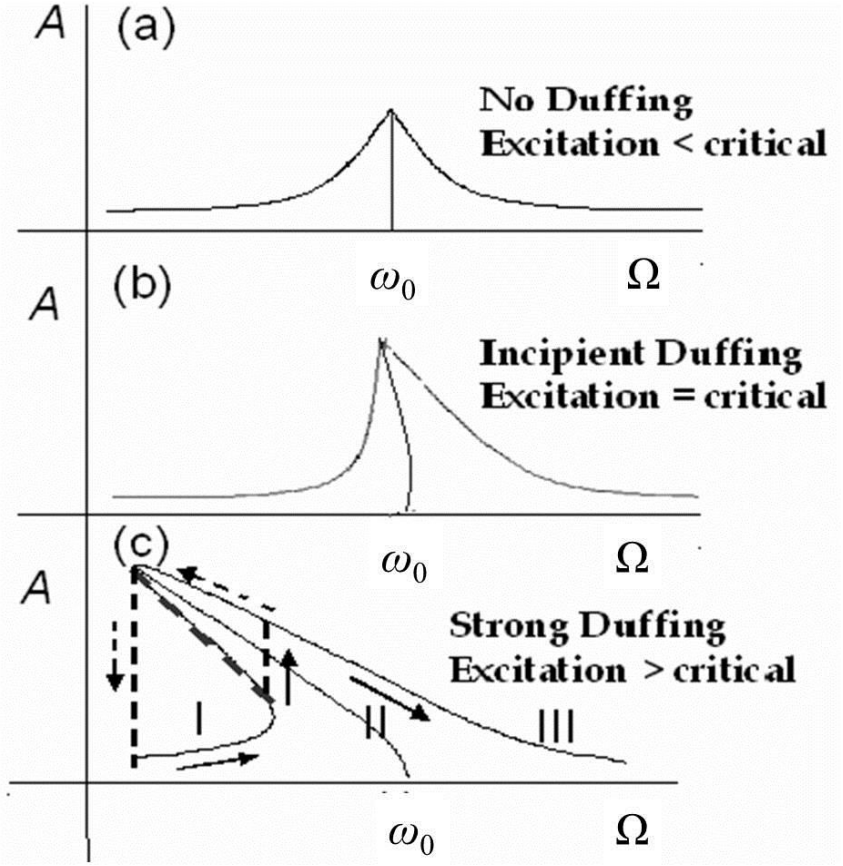

Figure 1.8: Steady state solutions under different excitation amplitudes *A* showing three stages of Duffing behavior. The natural resonance frequency, ω_0, is shown by the central line which differs from the driving frequency. In region (III) the system has only one stable solution which with decreasing frequency bifurcates into a stable solution and an unstable (dashed curve) solution. This stable solution grows in amplitude higher than the stable solution accessible with increasing frequency as Ω continues to decrease (region II). When the slope becomes infinite, this stable solution drastically collapses to the low

amplitude solution which is stable again (shown by dashed arrows in region I). (c) shows what one would expect in the first harmonic for a large third order non-linearity.[85]

A schematic of the stable steady state solutions under different excitation amplitudes is provided in Fig. 1.8. Here, some terminologies are defined in the A vs. Ω curves which are used in the experimental data analysis. If the excitation amplitude A (in our case, a function of V_{ac}) is less than the critical amplitude, only one solution exists, and no bi-stability is possible, Fig. (1.8a). If the excitation amplitude equals the critical amplitude, the system is on the edge of the bi-stability, in which a single point exists where A vs. Ω has an infinite slope showing incipient Duffing, Fig. (1.8b). If the excitation is greater than the critical value, the system is in the bi-stable regime with three possible solutions over a range of frequencies, Fig. (1.8c). Two of these solutions are stable. With increasing frequency the solution jumps from the low amplitude stable solution (region I) to another high amplitude stable solution (as shown by solid arrows) bypassing the unstable (experimentally unobservable) solution (shown dashed in region II). The large amplitude solution is stable and decreases with increasing Ω and finally enters into region III.

1.6 Pulsed Ring-Down Method

Similar to the capacitive HDR method, which is a continuous excitation technique, an alternative method incorporating intermittent actuation has been developed to overcome

the problem of parasitic capacitance. The pulsed ring-down method [86, 87] exploits the capacitive ring-down of a resonating cantilever upon a pulsed electrical excitation. A lock-in amplifier is unnecessary for signal detection, and a feedback loop is not needed to adjust the driving signal to the cantilever resonance. The experimental configuration in Fig. 1.9 is similar to that used for HDR, except the lock-in amplifier has been replaced by a digital storage oscilloscope.

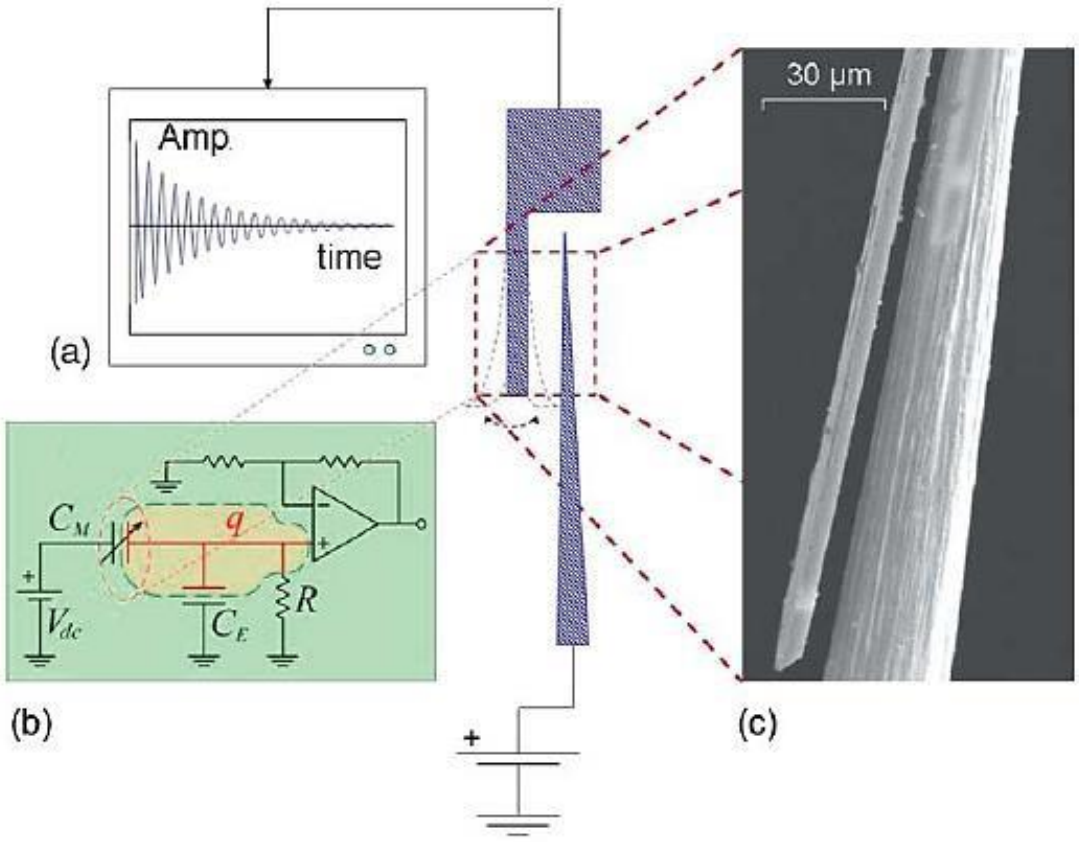

Figure 1.9: Experimental setup. (a) dc voltage source, microcantilever/counter-electrode (MCCE) system, and digital storage oscilloscope. (b) Equivalent circuit of MCCE system and amplifier. The inner shaded area denotes region of isolated electric charge, q. C_M is

the capacitance of the MCCE system, about 0.087 pF; C_E is the external capacitance, about 38 pF; R is the drain resistor, about 100 MΩ; and V_{dc} is the applied constant potential, about 9.24 V. Typical amplitude and ring-down time was 37 mVpp and 3.7 ms. (c) Edge view SEM image of MCCE geometry in the overlap region.[86]

The detection method is based on the principle of mechanical ring-down resulting in decaying oscillations in the capacitance when the excitation signal is withdrawn (Fig.1.9). This technique has important applications for concurrently measuring the density and viscosity of a either surrounding gas or gas mixture. Though this concept was previously proposed, only recently has a simple, robust, and accurate method of creating, measuring, and analyzing the ring-down signal been developed. Here, in a microcantilever resonating as a damped oscillator in a fluid environment, the free ring-down waveform contains information about the gas density and viscosity, which are often called the imaginary and real parts of the complex drag force. There is also an electrostatic force that acts on the system, resulting from the capacitance and voltage between the microcantilever and CE. Calculating this force requires modeling the MCCE geometry, which may be approximated by a series of wire segment/truncated-plane capacitive elements, where the wire segment represents the CE and the plane represents the cantilever. From the sum of the forces acting on the cantilever, its motion may be calculated. Finally, from the equivalent circuit of the MCCE (Fig.1.9b) the output voltage may be expressed as a function of displacement.

A microcantilever is made to undergo ring-down in the presence of various gases. Using the data collected, the voltage $V(x)$ as a function of the displacement x was adequately modeled, and x was deduced from V, (Fig. 1.9). The function $V(x)$ depends on the geometry of the capacitor model, and its accuracy is reflected in how well the calculated waveform matches the experimental data. The increase in frequency during the ring-down (caused by a decrease in spring softening with a decrease in amplitude) is essential for determining the electrical parameters (capacitor geometry), because a ring-down signal that varies in both amplitude and frequency requires a very particular fit, thus enabling a better empirical determination of $V(x)$.

The ring down approach has been successfully employed to measure the density ρ and viscosity η mixtures of gases. Fig. 1.10 depicts the experimental comparison of results to NIST reference values for various gases at ambient temperature and pressure. The method provides the high degree of accuracy for determining the composition of three-component mixtures of known gases. The high sensitivity of this technique enables distinction between mixtures of H_2 and D_2 to ±1% D_2. Though the densities of H_2 and D_2 are almost identical, the composition of their mixture can be determined accurately due to a significant difference in their viscosities. If the system is calibrated with the specific components, an even more precise quantification of gas mixture composition is possible.

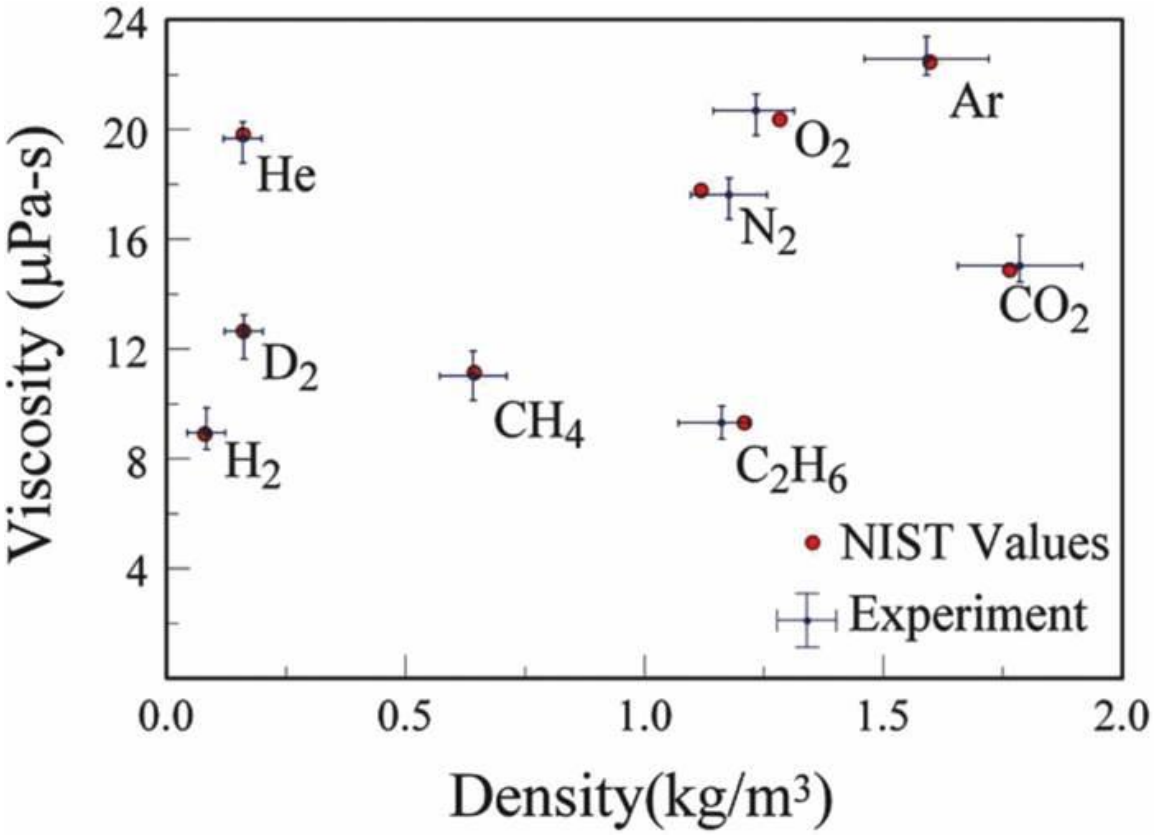

Figure 1.10: Plot of simultaneous measurement of viscosity and density. Error bars show the associated uncertainties resulting from the damping force correction functions applied to compensate for limitations, in the oscillating sphere model, for fluid damping.[86]

The use of a pulsed ring-down in a capacitive system is advantageous in that it eliminates the need for a lock-in amplifier for either detection or a feedback loop to adjust the driving signal to the cantilever resonance. Also the data collection is quick (~100 ring-downs/s), can be averaged, and does not involve scanning a frequency range to obtain entire resonance peak shapes. Not only does the nonlinear capacitance give greater sensitivity in the electrical signal, but it also perturbs the motion of the cantilever,

introducing some harmonic content, and causing the frequency to increase as the amplitude decreases. These characteristics aid in the determination of an accurate capacitance model, as well as in analysis of the ring-down waveform, important aspects of the pulsed ring-down method.

1.7 Conclusion

The HDR method is one of the few detection methods applicable to the nanoscale, and it is certainly a simple to implement. The vast potential of nanotechnology is only beginning to be realized, and it is anticipated that capacitive detection will be increasingly utilized in even smaller cantilevers. Though the HDR method, as reviewed in this work, was only implemented for singly-clamped cantilevers, extending this technique to a doubly-clamped (fixed–fixed) geometry can lead to greater range of applications. Due to their versatility and simplicity, micro and nanocantilevers will almost certainly be an integral component of many future MEMS and NEMS devices. As such, there will always be a need for a simple and effective sensing and actuation method, and for this there is perhaps no better choice than HDR.

CHAPTER 2

MECHANICAL PROPERTIES OF SOLIDS

The reduced size of LDMs offers new scientific possibilities and technical advantages. The size effects of LDMs are intriguing but are yet to be completely understood. Some of their material properties are steered by quantum mechanics and thus differ from the usual classical behavior.[16, 88] The ability to predict the mechanical response is a prerequisite to engineer materials with tailored properties. The desire to have a complete control of the ensuing behavior of a material has motivated researchers worldwide to design innovative methods to determine its mechanical nature. This collaborative effort has led to LDMs becoming integral components in next generation computer chips[89], ballistic impact protection[90], high frequency electronics[91, 92] and longer lasting satellites.[93]

The next section briefly introduces the mechanical parameters usually studied in elastic solids.

2.1 Mechanical Properties of Structural Solids

Material properties of solids pertain to their crystal structure and bond strengths. Under a stress (σ), a solid body changes shape resulting in a strain (ε). When this stress is small, the strain is linear with the stress. Provided this stress is below the elastic limit of the

material, its removal results in the body recovering to its undeformed state. This elasticity correlates to the nature of forces acting between the atoms or ions and the interatomic potentials in the lattice. Like many other physical properties of crystalline material, elasticity may be highly anisotropic.

The response of structural materials under a deformation has been studied experimentally and theoretically for decades. The established well known relation is Hooke's Law of elasticity, named after Dr. Robert Hooke who discovered it in 1660. In Cartesian co-ordinates, Hooke's law can be written in a generalized form as:

$$\sigma_{ij} = C_{ijkl}\varepsilon_{kl} \quad \text{(i, j = 1,2,3)} \qquad (2.1),$$

where σ_{ij} is defined as the i*th* component of force acting on the j*th* component of unit area normal resulting in a strain ε_{kl} (Fig 2.1). C_{ijkl} is the stiffness constant and is a 4^{th} rank tensor[94]. The stress and strain relations can also be expressed in an alternate, and sometimes more convenient form:

$$\varepsilon_{ij} = S_{ijkl}\sigma_{kl} \quad \text{(i, j = 1,2,3)} \qquad (2.2).$$

where S_{ijkl} refers to an inverse stiffness tensor (or compliance tensor).

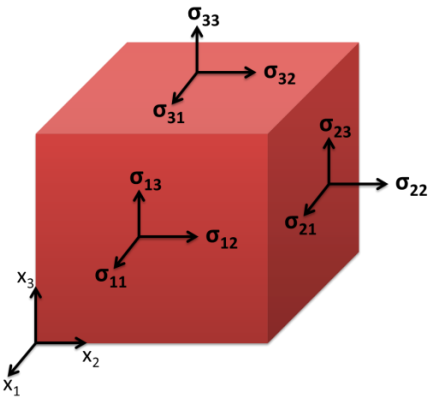

Figure 2.1: Direction of stress and strain components on a cube of material.

The stress and strain are rank 2 symmetric tensors i.e. $\sigma_{ij} = \sigma_{ji}$ and $\varepsilon_{ij} = \varepsilon_{ji}$, with 6 independent elements each. The compliance constant on the other hand is an 81 element tensor. However, it has been shown that

$$S_{ijkl} = S_{jikl} = S_{ijlk} = S_{klij}.$$

The symmetry of the S_{ijkl} and C_{ijkl} allows an introduction of a simple and concise matrix notation that facilitates reduction in number of suffices while dealing with higher order rank tensors. This is done by following transformation rule:

Tensor notation	11	22	33	13, 31	23, 32	12, 21
Matrix notation	1	2	3	4	5	6

Simultaneously, the 2 and 4 factors are introduced such that

$S_{ijkl} = S_{mn}$: when m and n are 1,2 or 3,

$2\ S_{ijkl} = S_{mn}$: when m or n are 4,5 or 6,

$4\ S_{ijkl}\ l = S_{mn}$: when m and n are 4,5 or 6.

Using these transformations, S_{mn} (or just $\boldsymbol{S}$) can be written as a 6x6 square matrix with 36 elements. The symmetry of the compliance (stiffness) tensor permits reducing it to a simpler form with "only" 21 independent elements that may be measured to completely describe the elastic properties of the material. The crystal symmetry can further reduce the number of independent elements to as few as 3 isotropic materials. Qualitatively, the diagonal elements of $\boldsymbol{S}$ correspond to the elasticity when the measured strain components

are in the same direction as the applied stress components. On the other hand, the off-diagonal elements describe the coupling between the applied stress and the deformations in the directions perpendicular to the applied stress components.

Different testing techniques probe different regions of this compliance matrix based on whether the material is subjected to bending, pulling or twisting. In the simplest case of a homogenous isotropic material, two independent stiffness constants E (S_{mm}; m=1,2,3), G (S_{mm}; m = 4,5,6) and their combinations, are enough to completely characterize its response under stress. The stiffness constants are then rendered independent of the direction and thus are equal in all directions. The elastic parameters E and G in isotropic materials are related through the Poisson ratio (υ) which is the negative ratio of the transverse to axial strain. The slope of the stress vs strain curve (Fig 2.2) can be used to measure the corresponding elastic constant. The shape of the curve also gives insights into the yield strength, its brittle or ductile nature and its ultimate strength.

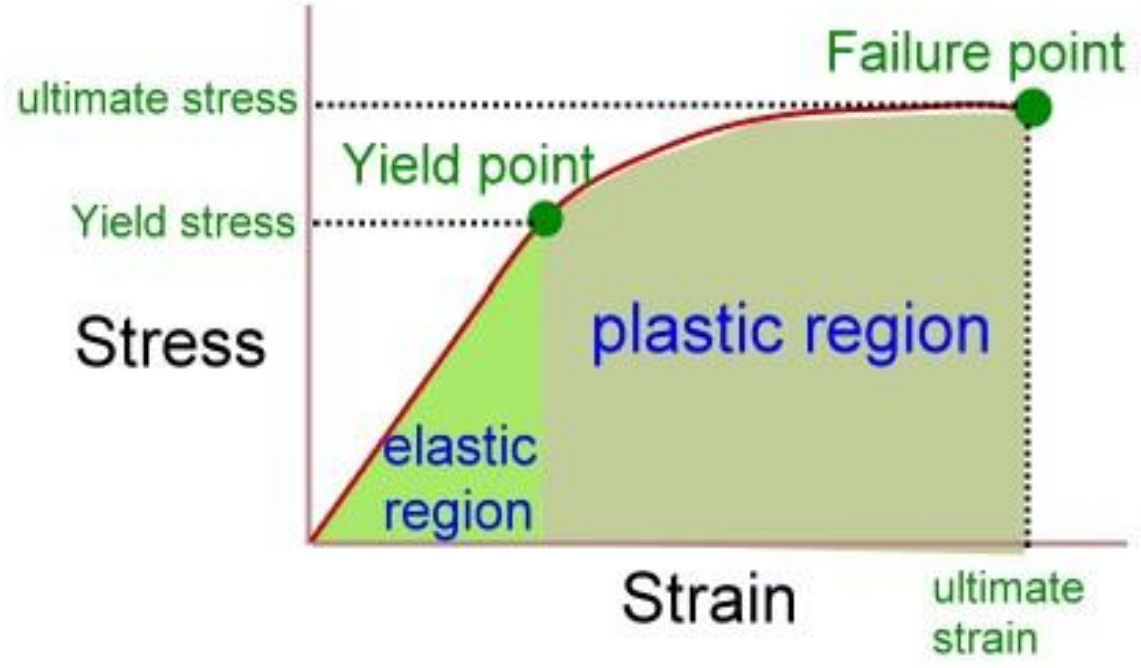

Figure 2.2: A typical stress vs strain curve. The initial linear regime is the elastic region following the Hooke's Law. Beyond the yield point, the materials begin to exhibit plasticity before it finally fails when the strain has reached its ultimate limit.

Changes in the crystal structure or defects in the solid modify its material parameters. The presence of grain boundaries as in a polycrystalline material or dislocations in a crystalline material allows slippage under stress and thus modulates the yield strength. It is worth noting that elastic modulus of the material indicates its stiffness to the applied stress which is many times mistaken for its strength. The strength of the material is judged by its resilience before fracture or specific deformations. Furthermore, strain in the material often results in dislocations which have the ability to move, allowing the

sample to extend plastically in the direction of the strain, also known as creep. By controlling the rate of stress (or strain) the creep mechanism can be probed. With a slow quasi-static increase in stress, the dislocations have enough time to move into an equilibrium position. However, when the stress is rapidly increased, the material doesn't have enough time to equilibrate or deform, as generally the case during sudden impacts resulting in a different stress vs strain curve. The sample can also be subjected to cyclic loading and unloading to study the effects of fatigue. Fatigue analysis is a critical study especially for device application as it probes the life of the device before the properties of the materials begin to degrade. To sum up, well characterized properties are imperative for accurate theoretical modeling that would result in rational designs and ensure the reliability of the device.

There exists a plethora of testing instruments that can perform measurements and characterize the mechanical nature of solid material. Instruments such as the INSTRON are standard techniques employed widely in research and industry. However, reduced physical dimensions of the materials acutely constraints the application of these well-established measurement methods. Hence, mechanical characterization of small scale materials such as fibers is often performed on bundles or yarns and statistically estimated for each strand. For example, IM7 carbon microfibers are usually delivered in a tow of 12000 fibers (Fig 2.3). An analysis of the tow, while necessary to characterize its properties, neglects the misaligned orientation and slipping of the fibers resulting in a

skewed measurement when extrapolated to represent an individual fiber, thus limiting the microscopic understanding of its material properties.

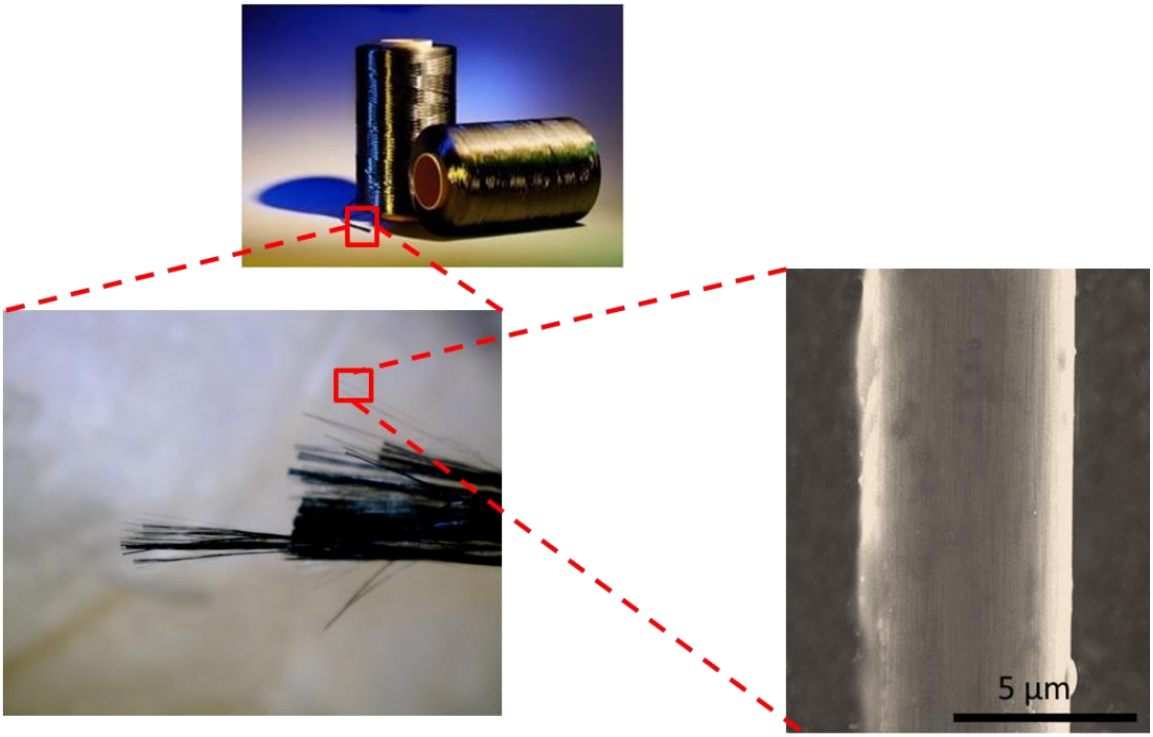

Figure 2.3: A tow of IM7 (top) consists of 12000 strands (bottom left) of carbon fiber. Each of these fibers (bottom right) is about 5 µm in diameter. Mechanical testing techniques should be designed to perform tests directly on the microfiber.

For an accurate analysis, the mechanical tests must be conducted on isolated materials. Some of the techniques that allow assessment on individual LDMs are discussed in the next section.

2.2 Current Testing Methodologies for Isolated LDMs

The past decade has witnessed major advancements in the development of newer, direct and indirect methods that probe the mechanical properties of small scale materials. Of all the possible methods, scaled-down INSTRON like techniques are by far the most utilized approaches to monitor the tensile/shear behavior of a yarn or fiber under a load. Typically a sample is mounted between two clamping ends, one of which is fixed. Preset strains are then applied to the sample and the corresponding stresses are measured. However, as the fiber dimension decreases and mounting becomes difficult, the utility of the instrument becomes limited. Alternate methods such as the fiber puller have proved to exhibit higher sensitivity[95]. The puller works using a capacitive detection scheme and is highly sensitive to small displacements. It also allows a study of higher order elastic constants, hysteresis and creep in the fiber. Recently, newer techniques have been used some of which are discussed below.

Nanoindentation: Scanning probe microscopy has proven to be a powerful tool to examine the surface topography and material hardness.[96] A high stiffness constant and sharp AFM tip is used to raster over the sample and provide a lateral load.[97] The ensuing deflection in the tip is optically detected using a reflected laser beam (Fig 2.4). The sharp cantilever tip (tip radius ~ 10 nm) allows local probing and displays unique accessibility. It may be used in either the static or dynamic mode. However, the static

mode is prone to errors due to slipping or shearing of the tip. In addition, it provides only a comparative idea of material hardness.

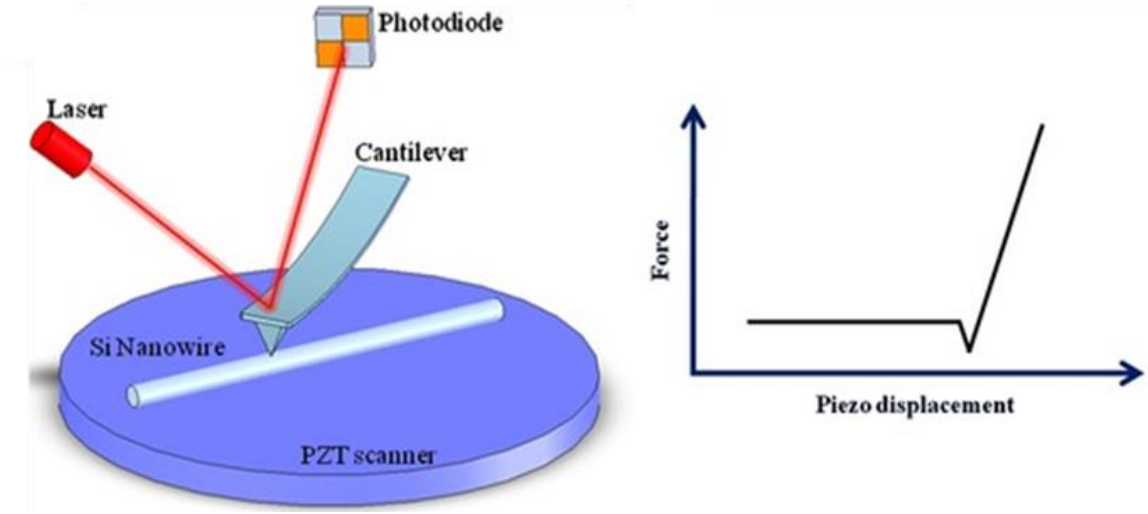

Figure 2.4: A schematic showing the use of a stiff AFM cantilever tip to provide stress (or strain) to an individual nanowire. The resulting displacement in the cantilever is detected optically. The ensuing force vs displacement curve is shown in the graph on the right. [98]

Three point bending test under electron microscope: A three point test is a standard testing scheme used in macro wires and beams. In the micro/nanoscale, the sample is usually laid over a trench which is usually micro-fabricated using lithographic techniques (Fig. 2.5).[99] The sample can be prepared for the test through drop casting or di-electrophoresis techniques. The ends are then secured using deposition methods such as the Focused Ion Beam (FIB) or electron beam deposition. A piezoelectrically controlled AFM cantilever is used to apply a pre-determined load on several points along the length

of the sample. The resulting strain is either visually measured under a transmission or scanning electron microscope or high speed camera. If the two ends are physically separate, then the same doubly clamped geometry can be used for examining the bending stiffness. This can be done by closing in the two ends of the substrate, forcing the LDM sample to bend or even buckle. However, this technique is limited to fairly conductive samples as the electron beam can induce defects on the samples. The electron beam can also potentially charge the sample making imaging increasingly difficult.

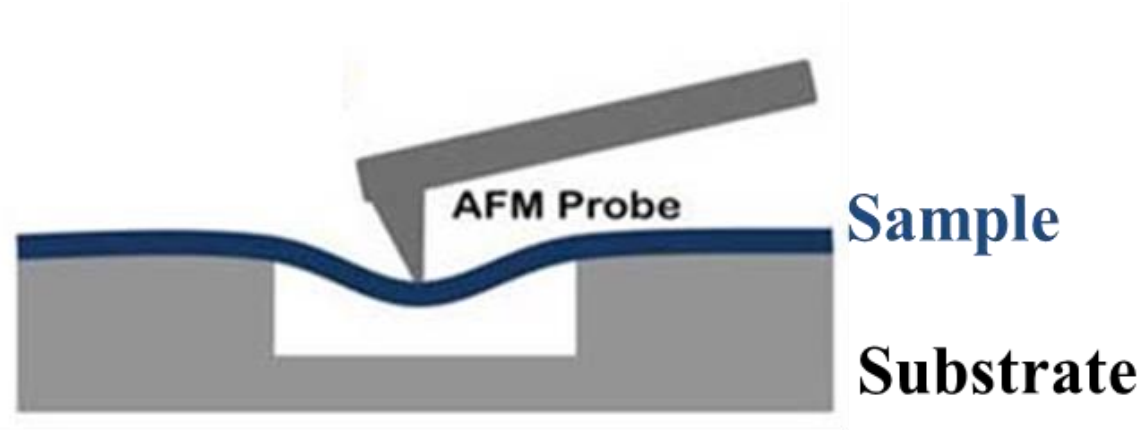

Figure 2.5: AFM probe used for applying a controlled stress on a doubly clamped LDM over a trench.[100]

Spectroscopy: Spectroscopy is a high resolution, non-destructive technique, used as an effective characterization tools for probing the surface atoms. Micro Raman spectroscopy was primarily a scientific research tool but instrumental advancement has now made it a commonly employed industrial method. The Raman spectrum is a signature of the vibrational response of atoms to the illuminated light and has been shown to be extremely sensitive to mechanical stress or structural changes.[101] Subtle alteration in the spectral

peaks can be used to monitor the material response. This high sensitivity has been recently used extensively to probe the mechanical structures of 2D layered materials.[102] Due to their high Raman cross section, carbon materials have been the most popular candidates studied through the Raman analysis. Under a stress, the material bond stiffening leads to a shift in characteristic Raman peaks such as the G band. This shift can be used to calculate an elastic modulus of the material. This technique however, can only be effectively employed if the sample is Raman active. Resonant Acoustic spectroscopy is another effective tool where the propagation of long wavelength acoustic waves through the solid can be studied.[103] Measuring parameters such as the frequency, velocity and attenuation allows the investigation of a variety of physical properties of the material. Propagation of elastic surface acoustic waves along the sample surface can be monitored and offers an easy probing technique especially when only one side of the sample is accessible.

Electromechanical resonators: One of the most prevalent methods of examining Young's modulus ($1/\boldsymbol{S}_{11}$) is to measure the resonant electrostatic deflection in singly or doubly clamped cantilever geometry.[44] A cantilever consisting of the material to be tested is subjected to an alternating electrical signal by applying an ac voltage to a closely placed counter electrode, inducing time dependent charge induction. The induced charge deflects the cantilever at a frequency which can be tuned by the driving signal. When the driving frequency matches the resonance frequency of the cantilever, the vibrational amplitude reaches its maxima. This resonance frequency of a cantilever is a function of the

cantilever geometry and its material properties and hence its precise detection can be used for accurately probing the Young's modulus.[104] This sort of bending analysis also allows a study of the nonlinear behavior of free standing resonators such as the mechanical Duffing response, wave like buckling and rippling distortion. Due to its various advantages, electromechanical resonance tool was a natural choice for probing the mechanics of the cantilevered LDMs of interest to this dissertation.

2.3 Difficulties Accompanying Current Techniques

Diverse techniques, as discussed above, have been designed to analyze specific aspects of the material's structure. Though techniques with very high sensitivities have been reported, the small scale of LDMs still poses several challenges in efficiently employing these techniques in a scalable fashion. Some of the major difficulties are:

(a) Isolating individual fiber/nanomaterials: Synthesized nanomaterials such as the nanotubes/nanowires are grown as aligned or randomly oriented forests. Separating individual tubes/wires requires sophisticated imaging and manipulation tools and can be time consuming even when possible.

(b) Micromanipulation requires specialized devices e.g. piezocontrollers or nano-tweezers, capable of holding and moving the sample in steps comparable to its own size.

(c) Mounting and securing: Due to their small dimensions, the sample can get damaged while mounting if it is not properly handled. Once mounted, appropriate

clamping methods must be selected. Epoxy polymers suitable for macro wires may fail when used to secure the micro/nanomaterials.

(d) Finding suitable actuation and detection techniques: Imaging at small dimensions requires modern tools such as state of the art electron microscopes. These instruments are bulky and extremely expensive.

Electrostatic actuation has been acknowledged as a highly versatile technique that has been successfully applied to micro and nanoscale materials. Detection techniques however have posed a bigger challenge. Some of the detection mechanisms are known to affect the material properties and thus lead to incorrect measurements. The capacitive detection scheme suffers greatly due to presence of high parasitic capacitance that overwhelms the very small electric current (usually in nA) from the resonating micro/nano cantilevers. As recognized in chapter 1, the HDR technique provides an easy route to electrically detect resonance signals at the higher harmonics of the driving frequency, circumventing the parasitic signal. Since the actuation geometry can be used for detection as well, additional apparatus or bulky imaging instruments are unnecessary.

HDR is sensitive to the varying gap distance between cantilever and CE. Hence, it is primarily based on the bending (or tensile) characteristics of the cantilever and is not suitable for directly probing the shear properties of materials. In fact, shear characterization is an often neglected front of mechanical characteristics. The research conducted during this dissertation is focused on designing new techniques for measuring

shear and tensile properties of isolated LDMs. The dissertation is hierarchically structured into following three divisions:

1. Developing a technique to enable direct measurement of the shear modulus of single microfibers: A twister apparatus was designed, built and tested.[105] (Chapter 3)

2. Elucidating the effects of detection techniques in measurement of the mechanical properties of low dimensional nanomaterials: We examined low frequency oscillations and transverse mechanical resonance of pristine and gold coated (Au-ZnO) ZnO nanowhiskers (NW) under an optical microscope and scanning electron microscope. By simultaneous HDR detection we decoupled the contribution of the electron beam on the measured resonance parameters.[106] (Chapter 4)

3. Probing mechanical behavior of a geometrically nonlinear cantilever *via* a helically coiled nanowire (HCNW): Transverse resonance of a helically coiled geometry was used as an alternate method of measuring the shear modulus of the comprising material. Using experimental and computational results we developed an empirical formula that can calculate the resonance frequencies of first two transverse modes. We also study the interesting planar and non-planar mechanical resonance modes resulting from exotic morphology of the coiled cantilever.[107] (Chapter 5)

The following sections briefly introduce the statement of the research work, the details of which can be found in the subsequent chapters.

2.4 Direct Measurement of the Shear Modulus of Individual Microfibers

High-performance fibers with multifunctional capabilities are now manufactured routinely for industrial, scientific and commercial applications and devices. Knowledge of their mechanical properties is invaluable as an engineering aid and in our understanding of the molecular structure and internal bonding. In contrast to tensile studies, the measurement of shear behavior has received comparatively little attention, even though shear characteristics are important in the design of high strength materials.

Two well-known methods for determining the shear properties of individual fibers are the torsion pendulum[108, 109] and the Kawabata torsion tester[110] (Fig 2.6). The torsion pendulum measures the natural frequency of rotational oscillation of a mass (whose moment of inertia is known) suspended by the fiber sample. Though simple in design, the dynamic nature of the torsion pendulum makes the study of creep or hysteresis very difficult. Gravitational force on the mass results in a pre-stress on the fiber which may be significant, particularly when the size of the fiber is less than a few microns. Moreover, the torsion pendulum does not lend itself to measuring shear yield, fracture, fatigue, or nonlinear behavior. The quasi-static system developed by Kawabata overcomes many of the limitations of the torsion pendulum and is used industrially, but is bulky and

expensive. Its torque detector, which uses a pair of linear differential transformers, would appear to have a significant moment of inertia (resulting in a longer response time), thereby limiting hysteresis measurements.

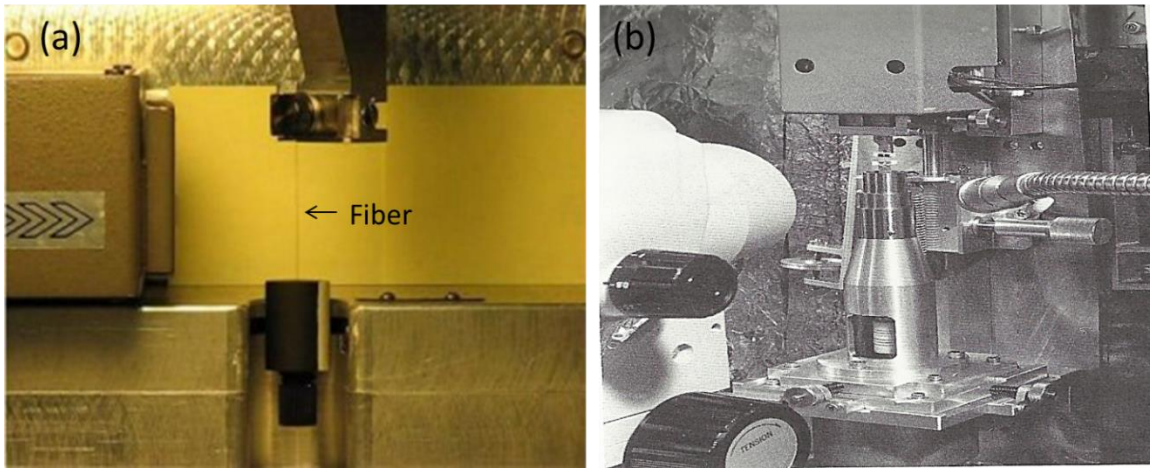

Figure 2.6: (a) A set up of a torsional pendulum. A known mass is suspended by the fiber. Upon actuating, the natural frequency of rotational oscillations can be used for calculating the shear modulus of the fiber[111] (b) Kawabata torque tester twists the fiber with a pre- determined strain and the ensuing stress is measured using linear differential transformers.[110]

The design and working principle of an inexpensive bench-top prototype, referred to as the "*twister*" is discussed in Chapter 3. The instrument uses a quasi-static method to measure the longitudinal shear properties of an individual microfiber. In the setup, a sample fiber is subjected to a specified twist angle, and the resulting torque is measured by a sensitive optical detection system. The applied twist can be precisely controlled, so

that not only the shear modulus, but the yield and ultimate strength may be determined. In addition, other shear characteristics may be studied, including creep, hysteresis and nonlinearity. The system is fully automated, making cyclic loading for fatigue measurements easy to perform. The results with various known fibers matched closely with the literature values, warranting its precision. In addition, measured shear moduli for technologically important microfibers including IM7 and Kevlar® are reported.

2.5 Fundamental Mechanism for Electrically Actuated Mechanical Resonances of Zinc Oxide Nanowhiskers

Low dimensional inorganic materials have gained much deserved attention in the past decade. Owing to their semiconducting behavior and tunable band-gap, applications in flexible displays and photo-voltaics have been successfully developed. Of the large functional oxides family, ZnO is one of the most important II-VI semiconducting materials. It portends promising applications due to its wide and tunable direct band-gap (3.37 eV at 300 K) and high exciton binding energy (60 meV). Its interesting piezoelectric properties have led to the development of self-powered nano-generators,[24, 112, 113] transistors,[114] sensors[23, 115] and actuators.[116] In addition, ZnO displays a rich diversity in physical structure and can be found as straight or helically coiled wires, four pronged tetrapods, comb-like and many more (See Fig 1.1). These unique structural and electrical properties have led to the exploration of ZnO nanostructures as key components for innovative MEMS and NEMS and AFM tips.

These recent advances motivated researchers to characterize the mechanical properties of ZnO nanostructures. Knowledge of the elastic modulus is essential in formulating accurate theoretical models required for predicting the reliability and robustness of the proposed devices. Some of the techniques introduced in section 2.3 have been employed to determine the Young's modulus of ZnO nanowires. For example, Huang *et al.*[117] measured the Young's modulus of ZnO NWs (dia. 40-120 nm) to be 58 GPa (using mechanical resonance) while Ni *et al.*[118] found a value of 31 ±2 GPa (using a three-point bending test with an AFM). One of the popular techniques to investigate the mechanical properties is to study the static or dynamic flexural transverse motion of the cantilever. The singly or doubly clamped cantilevered nanomaterial is actuated electrically using a counter electrode and the resulting mechanical resonance is observed visually under a SEM or TEM. In this regard, Hoffmann *et al.*[119] measured a Young's modulus of ~ 100 GPa (bending under electron microscope) for a ZnO NW (dia. 60- 300 nm) while Chen *et al.*[120] showed that the Young's modulus is size dependent (~140 GPa (550nm radius) to > 200 GPa (radius < 50nm)). An existing incoherence was observed in the measured Young's modulus values, which seemed to be dependent on the measurement technique. It is worth noting that most of the techniques require an electron beam for imaging while the tests are conducted. Though SEM/TEM enables a high-resolution imaging, it makes the electron beam an indispensable part of the experiment. Subsequent research[121, 122] has shown that an impinging electron beam (e-beam) on a semiconducting nanostructure (as in the case of examining mechanical resonance in a ZnO nanowhiskers, named due to their very high aspect ratio, under an electron

microscope) can significantly affect its electronic properties, and thereby alter its resonant behavior. However, this e-beam effect has been largely neglected while measuring the resonance frequency of ZnO nanoresonators. Furthermore, visual detection techniques fail to provide complete quantitative information about the cantilever motion, including the phase of its oscillation and the nonlinear effects that lead to instabilities in its resonance behavior. In order to detect the ZnO resonance parameters without any external perturbation, we employed the HDR technique and studied the cantilever behavior under different regimes.

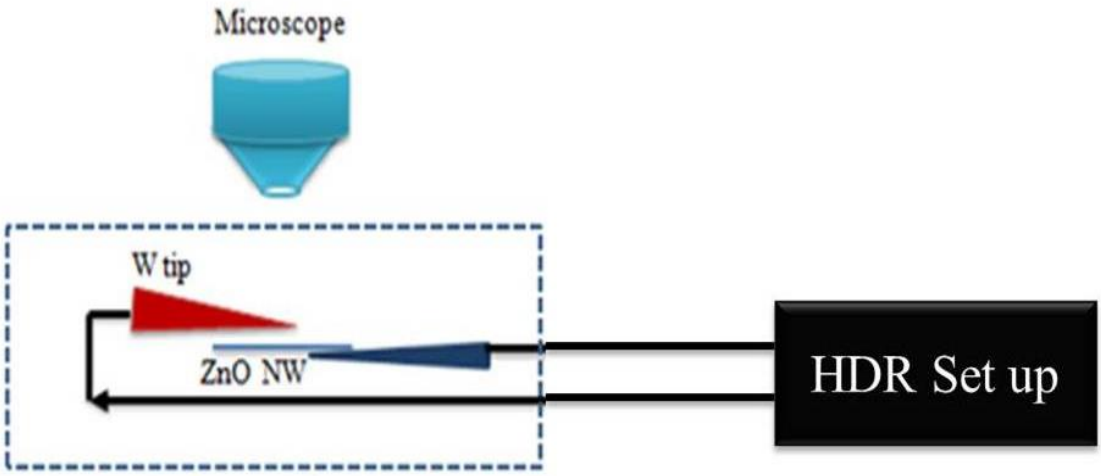

Figure 2.7: Schematic of a HDR set up coupled with the SEM. The microscopes used in this study were optical (Dark field) and electron (SEM). The optical set up allows measurement in ambient pressure whereas the SEM chamber may be used for studying in a vacuum environment.[106]

The basic HDR scheme, explained in the previous chapters, was employed. A conducting CE (usually a chemically etched tungsten tip; W-tip) is placed in close proximity (~ 5-10 μm) to the ZnO NW cantilever and V_{ac} with a dc offset (V_{dc}) is applied across the counter electrode-cantilever (CCE) arrangement. The lock-in amplifier detects the output of the pre-amplifier, which is proportional to the current, at a harmonic (integer multiple) of Ω.

In general, there are two possible mechanisms for the mechanical oscillations or actuation of the cantilevered NW. When a conducting cantilever is actuated electrically, on applying V_{ac} (the absence of V_{dc}) due to the nature of charge induction, the cantilever must vibrate at twice the driving frequency. Observation of this expected behavior confirms that the cantilever is properly grounded. In the *static charge mechanism*, stray (extrinsic) static charge is physically or chemically bound to the cantilever, and the electrical force on the cantilevered NW will correspond to the Coulomb force experienced by this bound charge due to the oscillating charge on the CE that is produced by the signal generator operating at Ω. As a result, the cantilever oscillation frequency will be Ω. This low frequency test is crucial to ensure a proper grounding of the cantilever and establish the source of the charge responsible for the observed vibrations.

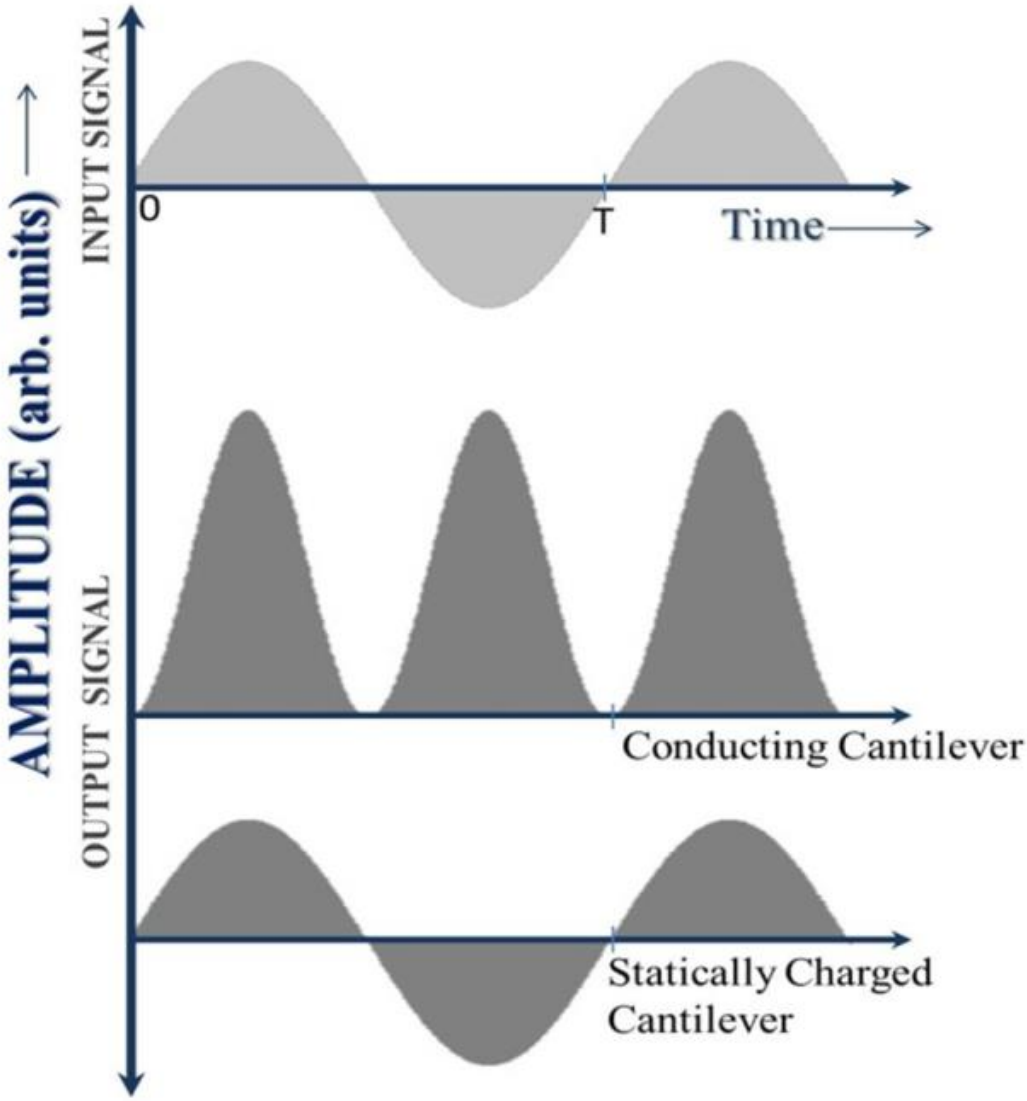

Figure 2.8: Schematic of the cantilever's amplitude dependence on the input signal. Under the influence of sinusoidal excitation, the oscillation frequency of the conducting cantilever is twice the driving frequency. In the presence of a static charge on a cantilever, the resulting oscillations will be at the driving frequency.[106]

As detailed in chapter 4, these low-frequency oscillations and the HDR resonance spectra of ZnO NW observed under an optical microscope are significantly different from results obtained under an electron microscope. This unusual behavior was further probed by varying the electron beam interaction with the sample and detecting its ensuing effects on the HDR signal. The designed experiments conducted were the following

(a) Examining the low frequency oscillations and first transverse mechanical resonance of pristine and gold coated (Au-ZnO) ZnO NWs under an optical microscope. The HDR method was simultaneously employed to detect the electrical signal of their resonances.

(b) Conducting similar resonance examination under an SEM. The e-beam was systematically varied by increasing the magnification of the instrument and noting the ensuing change.

Spectroscopic investigation provided further information regarding the mechanism to which this electron beam dependent resonance was attributed.

2.6 Probing Mechanical Resonance of a Helically Coiled Carbon Nanowire (HCNW)

Nature has inspired scientists through its multitude of nonlinear complex structures that exhibit tailored properties and diverse functionalities on multiple length scales. For example, biomolecules including DNA, bacterial flagella and various proteins adapt nonlinear geometries, particularly spring-like or helically coiled morphologies, for *e.g.*,

double-helix, α-coils or helices, which facilitate specific functionalities in living organisms. Indeed, this ubiquitous nanoscale helically coiled morphology has been proposed for enabling elastic memory devices,[123] flexible electronics,[124] impact protection,[90] nano-inductors, and efficient electromagnetic shielding.[125] Despite their enormous potential and their widespread applications, the mechanical behavior of helically coiled structures has evaded an accurate understanding at any length scale (nano to macro) mainly due to their geometrical complexity. Helically coiled topologies suffer from poor characterization, especially mechanical properties, and thus remain severely under-utilized in the realization of robust electronic, mechanical, and optical devices. While a few studies have focused on investigating the elastic properties using axial elongation[126]/compression[127] and atomic force microscopy (or force modulation microscopy)[128-130], an in-depth study of the dynamic mechanical response of helically coiled structures is incomplete due to the difficulties involved in exciting purely longitudinal/transverse resonances. This difficulty stems from the distinct helical geometry which exhibits convoluted shear and tensile motions when a singly-clamped coil is transversely driven. Theoretically, the resulting motion is described by a set of coupled 12^{th} order differential equations[131, 132] that are nearly impossible to analytically solve for the Eigen modes and their associated frequencies. In view of this mathematical complexity, helical coils are often treated as straight pillars[129, 133] without completely accounting for the shear/tensile component, thus preventing the acquisition of accurate Eigen modes and frequencies.

In chapter 5, we developed a synergistic protocol which (i) integrated *analytical*, *numerical* (i.e., finite element using COMSOL ®) and *experimental* (HDR) methods, to obtain an empirically-validated closed-form expression for approximating the *G* and *resonance frequency* of a singly clamped HCNW, and (ii) circumvented the need for solving 12*th* order differential equations. From the experimental standpoint, a visual detection of resonances (using *in situ* SEM) combined with HDR revealed intriguing non-planar resonance modes at much lower driving forces than those needed for linear carbon nanotube cantilevers. Interestingly, despite the presence of mechanical and geometrical nonlinearities in the HCNW resonance behavior the ratio of the first two transverse modes (f_2/f_1) was found to be similar to the ratio predicted by the EB theorem for linear cantilevers. We employed the HDR method[71, 134] to experimentally resonate isolated HCNWs and deduced their *G* by concurrently validating the experiments with analytical and numerical models.

In particular, we developed an analytical model that elucidates the contribution of shear stress when a helical coil is subjected to a transverse moment. By collating the individual components of shear and bending stresses, we derived a closed-form expression for the fundamental transverse resonance frequency of HCNWs as a function of both *E* and *G*. The values of *G* obtained in our analytical model provided only a coarse estimate due to several limitations imposed by our assumptions. Accordingly, we employed the numerical finite element COMSOL ® technique to estimate more accurate *G* values started from the coarse analytical estimates. Furthermore, we observed intriguing

resonance modes (e.g., a circularly polarized mode) in HCNWs with a characteristic signature in the HDR signal, thus facilitating the electrical detection of nonlinear resonance modes. In general, we demonstrated that the HDR technique, in tandem with our analytical model and COMSOL® simulations can serve as a standard protocol circumventing the need for solving 12^{th} order differential equations for probing the shear properties of coiled geometries.

CHAPTER 3

DIRECT MEASUREMENT OF THE SHEAR MODULUS OF MICROFIBERS

3.1 Experimental Setup

The twister,[105] shown schematically in Fig. 3.1, incrementally applies an angular displacement (θ) to one end of a fiber sample and measures the resulting torque using the torsional deflection (θ_{ref}) of a reference tube coupled with an optical sensor. Note that the twist in the sample (θ_{sample}) = $\theta - \theta_{ref}$, however $\theta_{ref}/\theta < 10^{-4}$ so that $\theta_{sample} \approx \theta$ (within 0.01%); therefore we will use θ_{sample} to refer to the twist provided by the stepper motor as well as to denote the sample twist.

The setup consists essentially of two parts – the driving and the detecting units. Each unit incorporates a length of 304 stainless-steel hypodermic tubing *viz.* a short (~ 3 mm) driving tube (D-tube) and a long (~72 mm) thin (310 μm OD, 190 μm ID) reference tube (R-tube) as shown in Fig. 3.1a. The opposing ends of these coaxially configured tubes, separated by an adjustable distance, serve as the mounting points for the sample fiber.

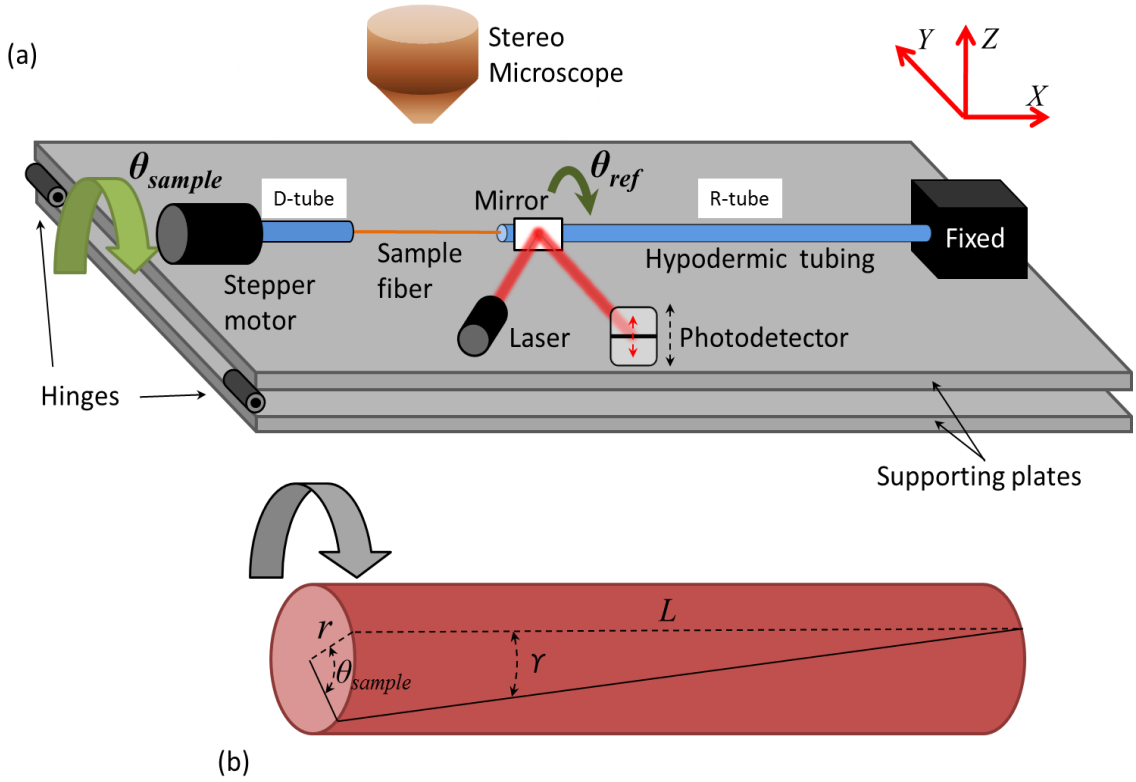

Figure 3.1: (a) Schematic of the twister setup. (b) Diagram of a fiber to define sample parameters: length L, radius r, twist angle θ , and shear strain γ . Note $\gamma = r\theta_{sample}/L$. [105]

The free end of the D-tube is coupled to a stepper motor, providing a high-resolution angular displacement (±1.57 mrad) in increments of 31.4 mrad to the sample. To accommodate a range of sample gauge lengths, the stepper motor is mounted on an *X*-axis micrometer stage, allowing the stepper motor/D-tube assembly to be moved parallel to the sample axis, varying the distance between the two sample mounting ends. In addition, the stage provides a means to adjust the slack in the mounted fiber or to apply tension to the sample, if desired. In our setup, sample lengths up to 20 mm can be

accommodated; however, this may be increased with only slight modifications to the design. The R-tube, at its opposite end, is fixed to an immovable block.

The optical detection system comprises a small mirror (aluminized glass microscope cover slip, ~2 mm x ~4 mm x ~0.17 mm) attached to the R-tube close to its sample end, and oriented so that its plane is parallel to the axis of the tube. A low-power red laser (BEA Lasers, model #201-1-650) is reflected off the mirror and collected by a position sensitive detector (PSD) which uses a dual-element photodiode (Hamamatsu 3096-02) in an arrangement similar to that in an AFM. A simple op-amp circuit (Fig. 3.2) amplifies the signal to produce an output voltage that varies linearly with the position of the laser spot.

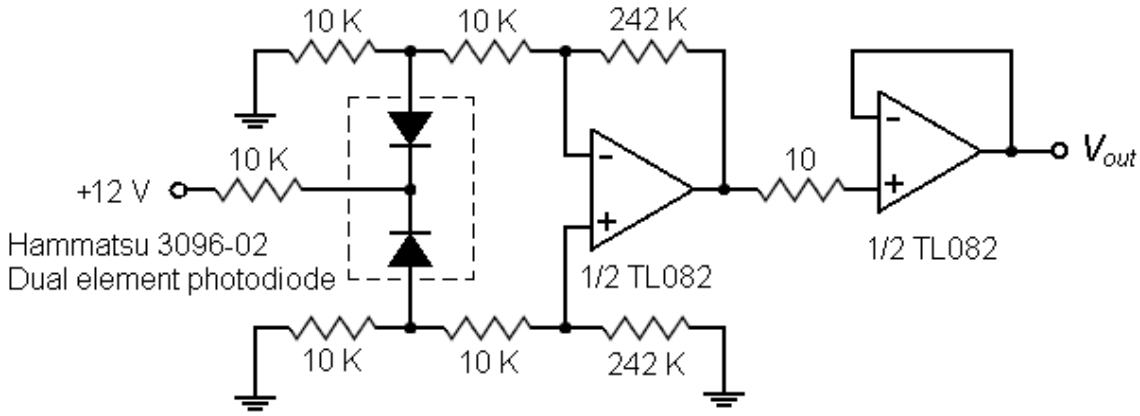

Figure 3.2: Dual element PSD amplifier circuit. The output voltage (V_{out}) is linear with displacement of the laser spot on the detector.[105]

The laser can be adjusted to optimize the position of the spot on the mirror. The PSD is attached to a *Z*-axis micrometer stage, which is used to calibrate the detector and assure its linearity, as will be discussed later. The entire setup is mounted on a thick aluminum base that acts as an optical bench and helps reduce vibrational noise.

LabVIEW© assisted control and data acquisition allows a broad range of experimental parameters. For example, the stepper motor can be programmed to increment by a specified angle, dwell for a specified duration (to study the creep in the fiber, if desired) during which data acquisition from the PSD occurs, and then repeat the sequence for a specified number of increments or decrements. The output voltage from the PSD is interfaced using an analog-to-digital card. The minimum angular increment of the stepper motor is 0.0314 rad, but if necessary, a servomotor motor may be substituted to provide increased resolution or rotation rate. A sample is subjected to a maximum twist sufficient (typically between 3.14 and 62.8 rad depending on its torsional stiffness) to produce an optimal response in the PSD. The shear strain (γ) at the fiber surface (where it is the largest), is given by $\gamma = r\theta_{sample}/L$, where r and L are the sample radius and length, respectively. The shear strain was calculated for the maximum twist angle for each fiber (Table I). The overlap of the twisting and untwisting data (see Fig. 3.6) indicates that no sample damage occurred due to shear strain. The detector (mirror and R-tube) has a low moment of inertia, permitting instant rotation and short dwell times, so that the system may be used to study hysteresis and fatigue strength, in addition to shear modulus, yield strength, ultimate shear strength, nonlinearity, and creep.

3.2 Calibration of the R-tube

The thick aluminum base consists of two parallel aluminum plates hinged together at one end. The top plate can be rotated to an upright position, perpendicular to the horizontal bottom plate (Fig. 3.3). This allows the R-tube to hang vertically.

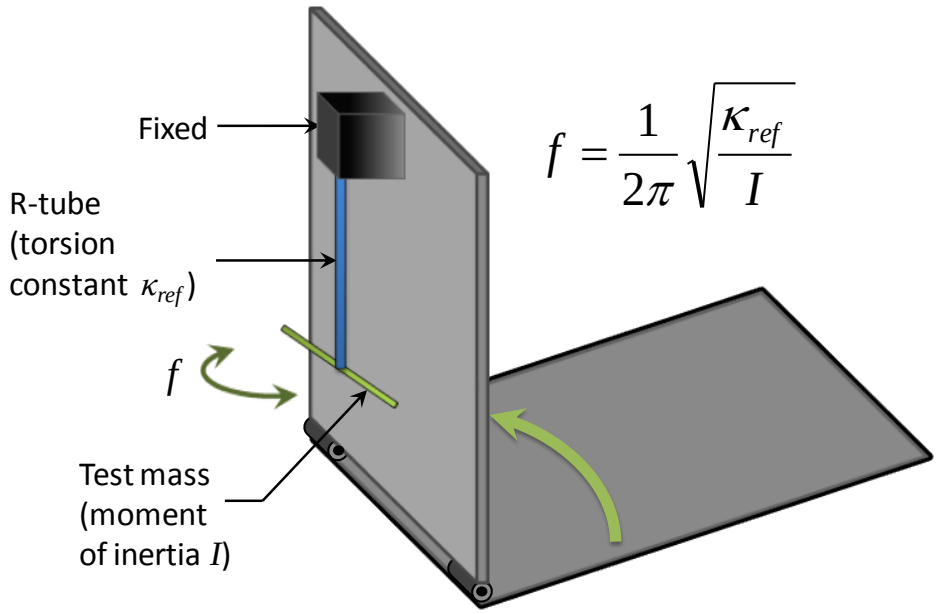

Figure 3.3: Schematic of reference tube calibration. The upper plate is rotated vertical to convert the R-tube into a torsion pendulum. The torsion constant (κ_{ref}) is calculated from the resonance frequency (f) and the moment of inertia (I) of a test mass. [105]

A mass with an appropriate I about the rotation axis is then attached to form a torsion pendulum (I = 2.931x10^{-5} kg·m^2 in our calibration). On providing and releasing a small initial torque, we actuate the free rotational oscillation of the system and measure its

resonance frequency (f), from which we calculate the torsion constant (κ_{ref}) of the R-tube. Analogous to the spring constant in Hooke's law, κ is defined by

$$T = -\kappa\theta \qquad (3.1),$$

where T is the torque and θ is the torsion angle. Assuming negligible damping,

$$\kappa_{ref} = 4\pi^2 I f^2 \qquad (3.2).$$

On calibrating the reference tube, we obtained $\kappa_{ref} = 0.76 \pm 0.01$ nN·m/μrad.

3.3 Calibration of the photo-detector

The optical system that measures the torsion in the R-tube is calibrated by measuring the change in voltage resulting from a known displacement of the laser spot on the PSD. Rather than move the laser, we manually move the PSD a specified distance using the attached Z–axis micrometer. At its center position, with equal intensity on both photodiode elements, the PSD produces zero output voltage. As the laser spot is displaced, conductance is decreased in one photodiode and increased in the other, producing an output that is linear over a range of ±4 V (Fig. 3.4). This corresponds to a displacement of approximately ±40 μm, which is equivalent to an R-tube rotation of ±100 μrad. The rotation of the R-tube as a function of the PSD displacement is found using elementary optical geometric principles as shown in Fig. 3.5. In our setup, the distance from the mirror to the PSD is 0.20 m, giving a proportionality constant of 2.5 μrad/μm.

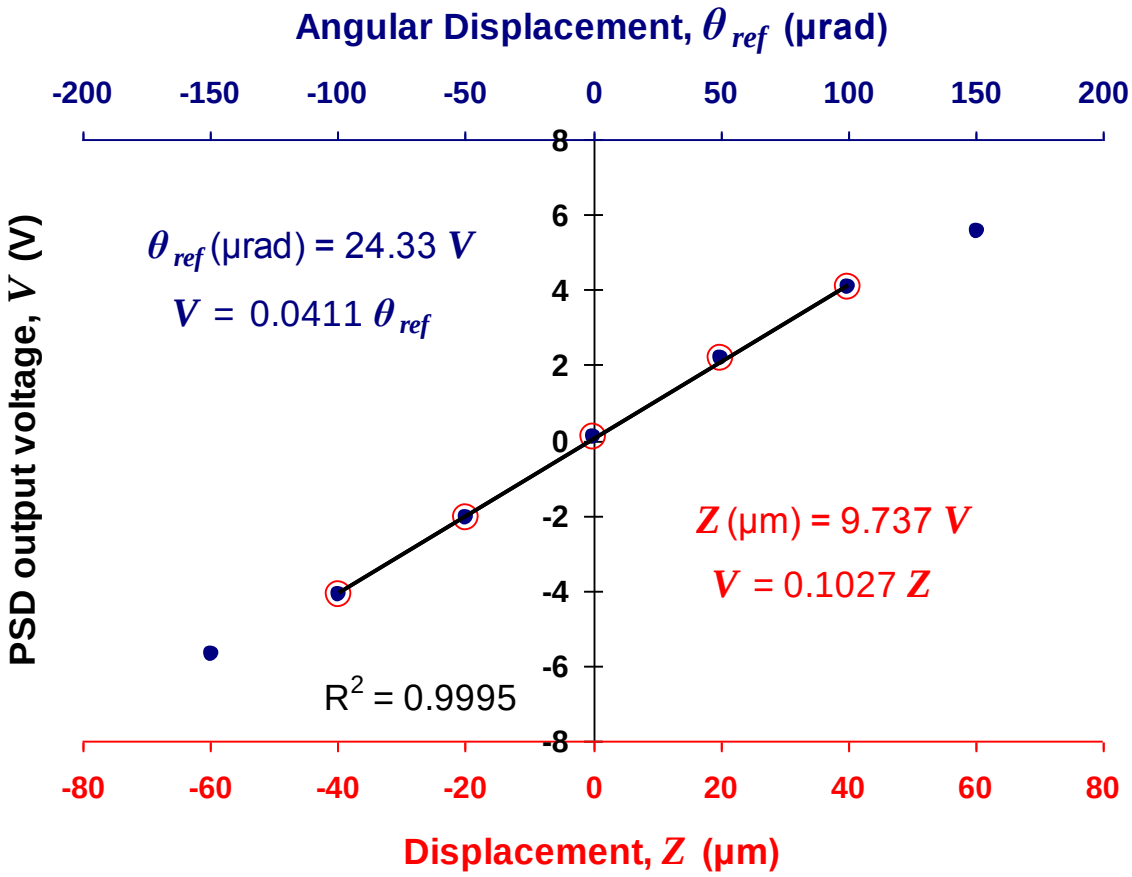

Figure 3.4: Typical calibration curve for the photodetector is a plot of output voltage of the photo detector vs linear displacement of the laser (lower X-axis) and its corresponding angular displacement (upper X-axis). Experimental measurements fall within the linear range. Note that the torque $T = \theta_{ref}\,\kappa_{ref} = 24.33V\mu\text{rad} \cdot 0.76\ \text{nN·m/}\mu\text{rad} = 18.5V\ \text{nN·m}$. [105]

Accordingly, we apply this factor to the calibration curve to give θ_{ref} directly from the detected output voltage, facilitating calculation of the torque as a function of output

voltage. To ensure reliable results, a calibration curve is obtained before and after data collection for each sample. The PSD response is ~103 mV/μm which is equivalent to 41.2 mV/μrad in terms of θ_{ref} . With our κ_{ref}, the linear range of ±4 V corresponds to a torque of ±76 nN·m.

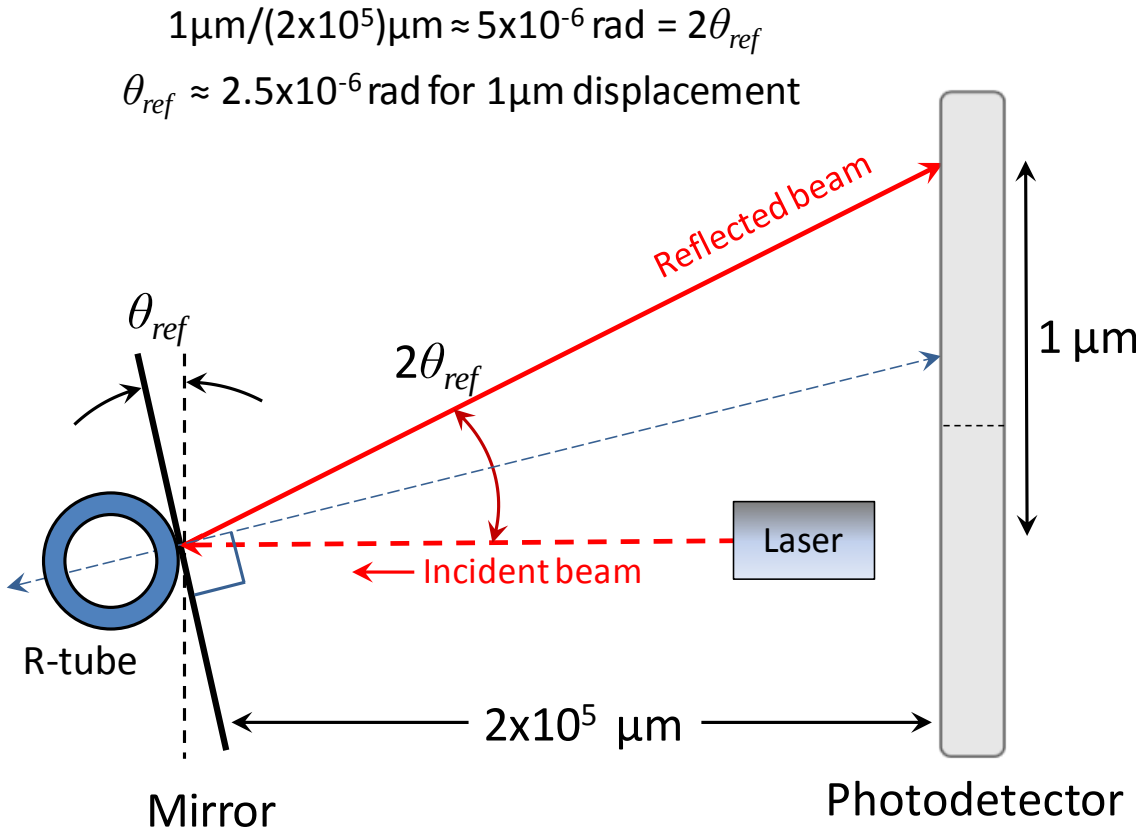

Figure 3.5: Schematic of optical detector system (not to scale). Note that if the R-tube rotates by θ_{ref}, the laser beam angle changes by $2\theta_{ref}$.[105]

3.4 Mounting the Sample Fiber

We isolated a single strand of the microfiber to be measured, and mounted it with the aid of a stereo microscope. Any initial twists or bends were carefully avoided. The sample ends were inserted into the tube and secured using high strength epoxy glue (Devcon). Capillary action at the end of the tube draws the glue slightly into the tube, aiding in centering the fiber on the axis and increasing the strength of the bond. Though the labeled curing time for the epoxy was a few hours, we found that allowing it to remain overnight held the fiber more securely.

3.5 Operation of the twister

During a test, the stepper motor rotates the D-tube a specified angle (θ_{sample}) applying a twist to the fiber (Fig.3.1b). The fiber experiences a shear stress and transmits the torque to the R-tube. This produces an angular displacement (θ_{ref}) in the R-tube, rotating the attached mirror by θ_{ref} as well. The reflected laser beam rotates by $2\theta_{ref}$ (as illustrated in Fig. 3.5) displacing the laser spot on the PSD, and the output voltage V is recorded. The calibration curve allows us to calculate θ_{ref} from V, and multiplying it by κ_{ref} we obtain T. Since T is equal in the sample and the R-tube, Equation 3.1 may be written as:

$$T = -\kappa_{sample}\theta_{sample} = -\kappa_{ref}\theta_{ref} \qquad (3.3)$$

A typical plot of T vs. θ_{sample} (which was linear for our samples) is shown in Fig. 3.6.

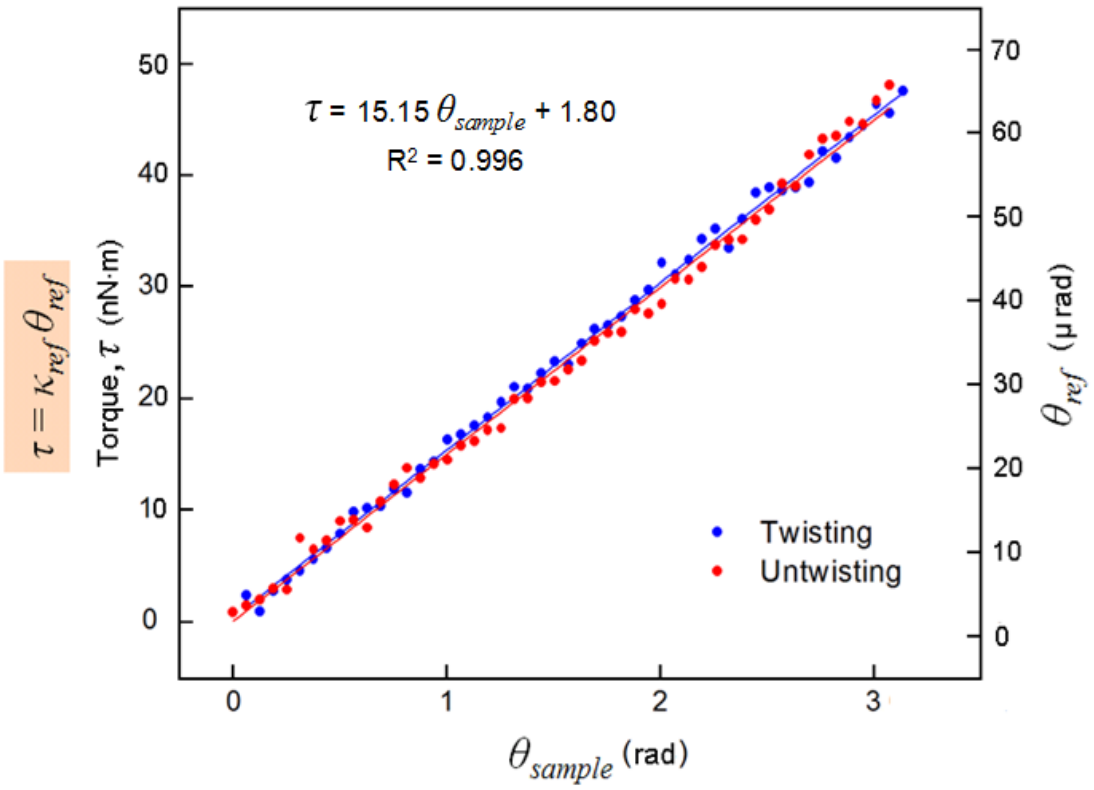

Figure 3.6: Typical data from one twisting and untwisting sequence of a single Cu wire (r = 7.5 μm, L = 16.5 mm). The average slope is 15.15 nN•m/rad, which is the torsion constant of the sample (κ_{sample}).[105]

The slope $dT/d\theta_{sample}$ is the torsion constant of the sample (κ_{sample}) from Equation 3. The shear modulus (G) of the fiber material may then be calculated from:

$$G = \left(\frac{L}{J}\right)\frac{dT}{d\theta_{sample}} = \left(\frac{L}{J}\right)\kappa_{sample} \qquad (3.4),$$

where L is the sample length and J is the second moment of inertia. Assuming a circular cross-section for the fiber, $J = ½\,\pi\, r^4$, where r is the radius.

3.6 Results and Discussion

The accuracy of the twister results was verified by testing a 7.5 μm diameter tungsten wire (gauge length 17.6 mm) and a 15 μm diameter copper wire (gauge length = 9 mm). The diameter of the samples was measured within ±3 % using an SEM (Fig. 3.7). Note that this implies a ±12 % uncertainty in *G*.

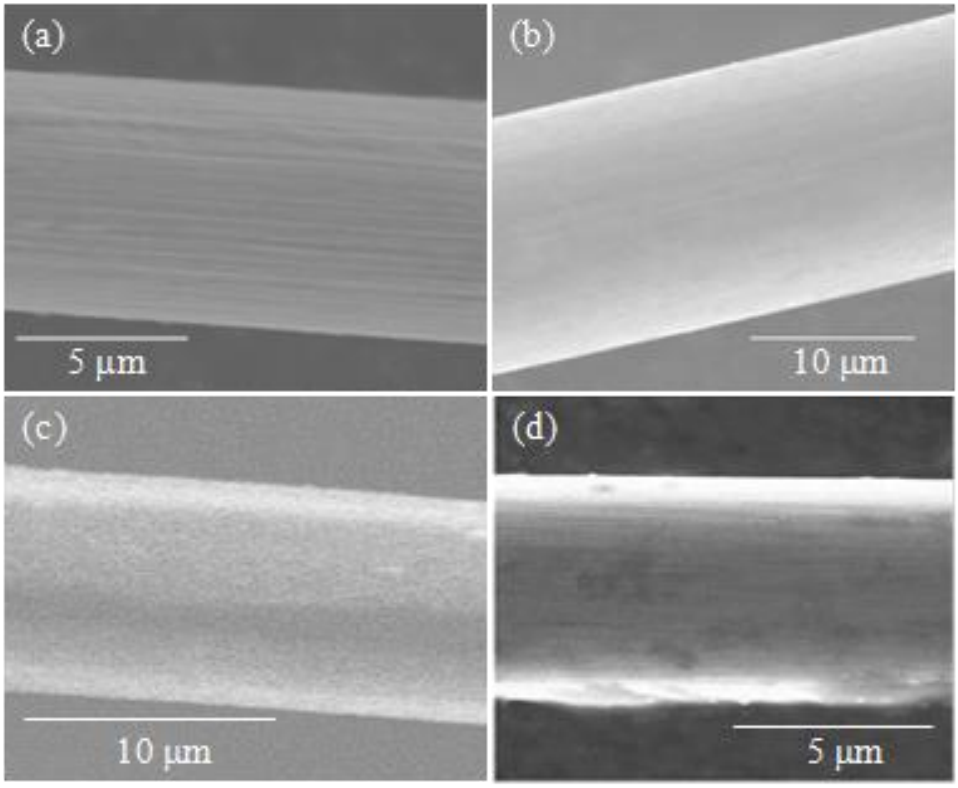

Figure 3.7: SEM images of fiber samples; (a) tungsten, (b) copper, (c) Kevlar® 119, and (d) IM-7. [105]

In addition, we measured the shear modulus of a few industrially important fibers, two of which have not been previously reported (IM-7 and Kevlar® 119). The gauge length did not make a significant difference in measured properties.

Material	Dimensions		Max sample twist	Shear modulus G			Shear strain	Refs.
	Dia.	Length	θ	Meas.	Lit.	Diff.	γ	
	μm	mm	rad	Gpa		%	mrad	
Copper	15	16.5	3.14	41.4	45.4	-8.8	2.6	NIST
Tungsten	7.5	17.6	31.4	156	160.6	-2.9	6.7	JAP
Kevlar® 119	11	17.6	62.8	2.42	NA	NA	19.6	Note 1
IM7	5.3	17.5	62.8	16.5	NA	NA	9.5	Note 2

Table 1: Shear modulus measurements. Note 1: The *G* of Kevlar® 119 has not been previously reported. Note 2: IM6 (a fiber similar to IM7) has a reported[109] *G* = 10.1 GPa, and unspecified PAN based carbon fibers have a reported *G* ranging from 14-18.GPa.[135]

The shear moduli of the metal fibers are consistent with the published values of *G* for the bulk isotropic material, indicating that these fibers are isotropic as expected, although it is possible for fabrication processes to introduce anisotropy in metals.

In contrast, *G* for the polymer and carbon fiber samples was much lower than would be expected if the fibers were isotropic. For example, IM7 fiber has *E* = 280 GPa and the measured *G* = 16.5 GPa. If the material were isotropic, the resulting Poisson ratio is *v* =

$E/2G - 1 = 7.2$. Because it is extremely rare for materials to have $\nu > 0.7$, we suggest that IM7 may only be transversely isotropic, with properties different in the axial and radial directions, and possibly the core of the fiber being different than at its surface, as has been shown for some carbon and Kevlar® fibers that have a core/skin structure[136]. Note that if the skin thickness is the same in two fibers of different diameter, then the thickness may be calculated from measurements of G for the two fibers. For Kevlar® 119 fiber, in a similar analysis, the Poisson ratio is $\nu = 53.9/4.84 - 1 = 10.1$, which again suggests a large anisotropy in accord with the reasons given above. Additionally, this observation is consistent with the proposed structure of Kevlar® fiber being comprised of polymer chains parallel to the fiber axis, with the attraction between the chains being much weaker than the covalent bonds in the chains themselves.

3.7 Conclusion

While the characterization of micron sized fibers has mostly been centered on their tensile properties, the measurement of shear properties is important for the design of high strength materials and for elucidating their anisotropy and non-uniformity, and thus their microstructure. The twister is a simple and inexpensive apparatus capable of accurately measuring the shear properties of individual fiber strands. The twister is expected to fill a niche among the various methods used for evaluating shear behavior of emerging fibers, thus enabling greater access to the measurement of their fundamental properties and development of new and useful devices.

CHAPTER 4

FUNDAMENTAL MECHANISM OF ELECTRICALLY ACTUATED MECHANICAL RESONANCES OF ZnO NANOWHISKERS

4.1 Synthesis and Characterization

ZnO NWs with diameters varying from 500 nm to 1 μm were synthesized via the vapor solid mechanism in a chemical vapor deposition (CVD) method (Fig 4.1).[137] Amalgamated Zn pellets (Fisher Scientific, 99.999 % pure) were mixed with anhydrous $Zn(Ac)_2$ (Fisher Scientific, 99.98 % pure, molar ratio of 10:1) and placed in a ceramic boat (Coorstek No. 600036). A Si (100) wafer was placed face down over the ceramic boat (to completely cover its downstream end), and the boat was heated to 650 ^{o}C under 40 sccm of flowing Ar in a 1" dia. quartz tube reactor. After attaining thermal equilibrium, the Ar flow was continued for 15 min, after which it was shut off and replaced with 20 sccm of flowing O_2 for another 15 min. Subsequently, the furnace and gas flow were shut off and the samples cooled to room temperature.

The as-grown ZnO NWs were characterized using Photoluminescence (PL), X-Ray diffraction (XRD), and Raman spectroscopic techniques. PL spectra (Fig 4.2a) showed the expected near band edge emission ~380 nm (3.37 ev) of semi-conducting ZnO. The

PL peak in the visible region (~512 nm) for ZnO NW is relatively broad due to presence of inherent defects in ZnO NWs. A detailed study of the origin of such defects was studied through PL and non-linear optical spectroscopy.[137] XRD diffractograms (Fig 4.2b) showed Bragg peaks that corresponded to the wurtzite ZnO structure with lattice parameters, *a* and *c*, of 0.327 and 0.524 nm, respectively. The Raman spectrum (Fig 4.2c); excitation at 514.5 nm in a Dilor XY triple grating spectrometer (equipped with TE cooled CCD) confirmed the wurtzite structure *via*. the presence of Raman peaks at ~407 cm^{-1} (E_1(TO)), 437 cm^{-1} (E_2), and 582 cm^{-1} (E_1(LO)).[116, 118] (Appendix A).

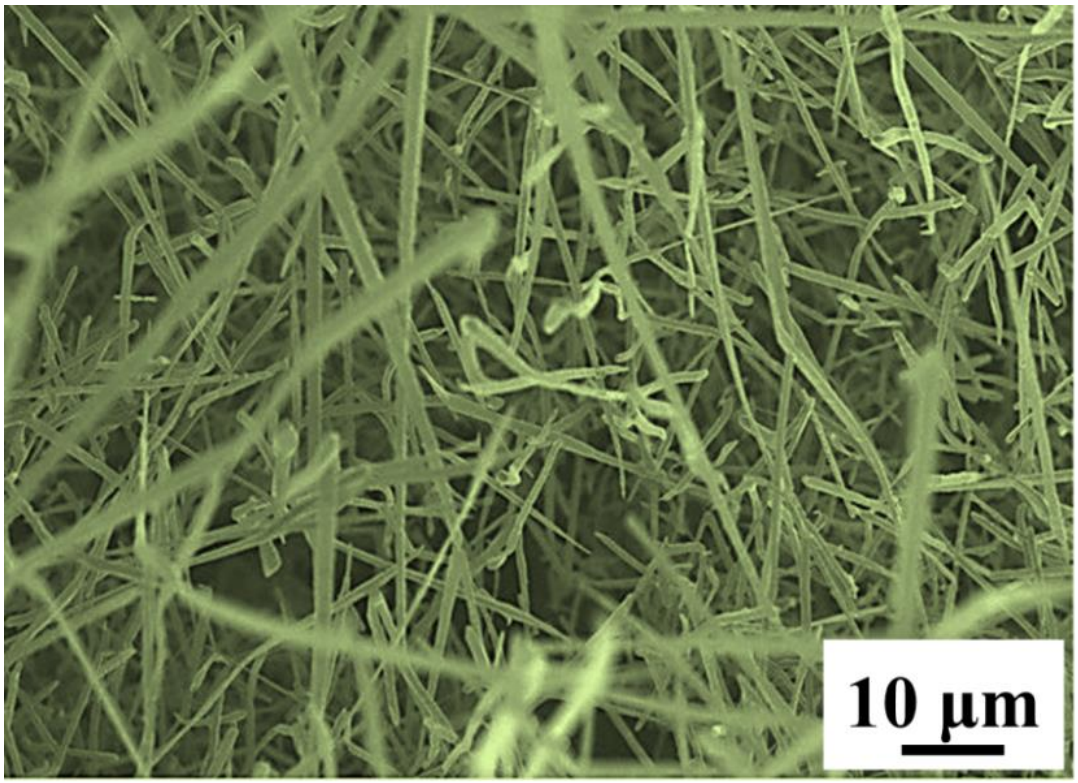

Figure 4.1: False colored scanning electron microscopy image of as-grown ZnO Nanowhiskers sample grown using chemical vapor deposition method. [106]

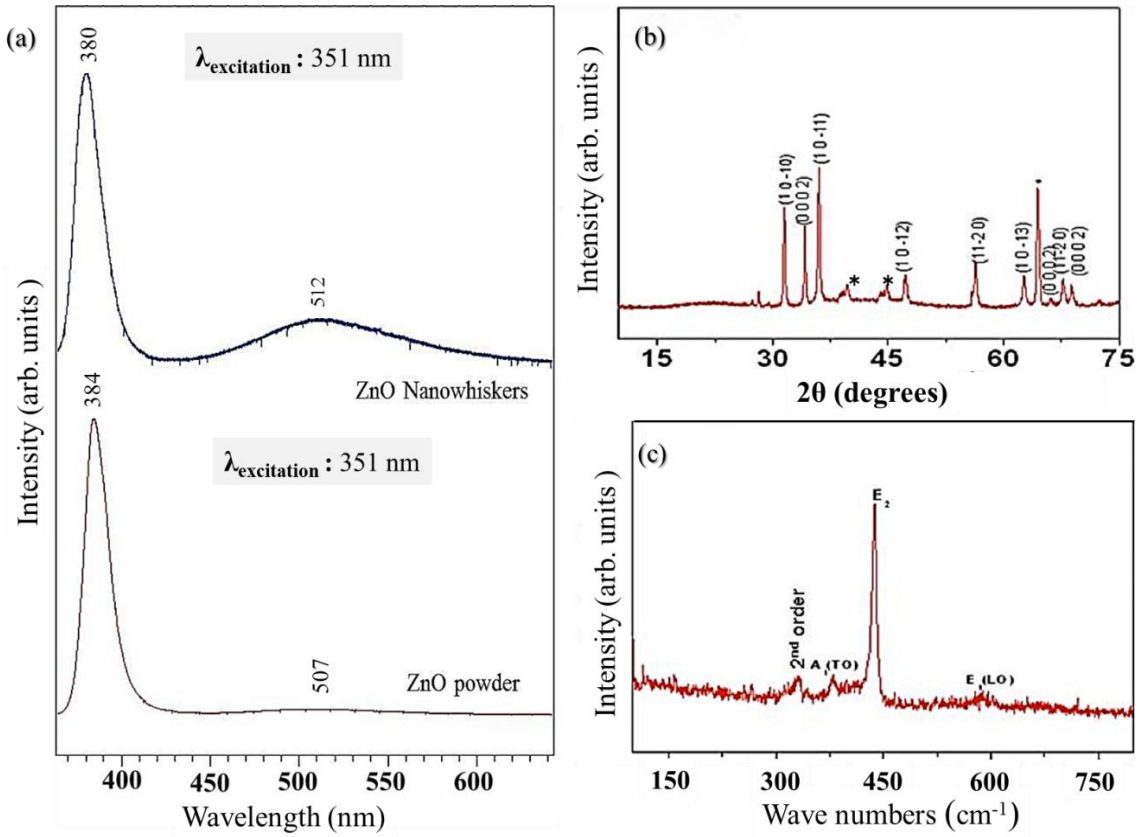

Figure 4.2: (a) Photoluminescence (PL) spectra of bulk and as-grown ZnO NWs excited at 351 nm. Both spectra show a prominent peak ~380-385 nm corresponding to the band-gap of ZnO. The hump in the yellow-green region (~520 nm) in the PL spectrum of ZnO NWs is due to the presence of defects which includes Zn and O vacancies. (b) An X-ray diffractogram of as-grown ZnO NWs in which the peaks indicated by the * correspond to the Al sample holder. (c) Raman spectrum of as-grown ZnO NWs which shows peaks corresponding to the wurtzite ZnO crystal structure, along with the second order Raman feature at ~331 cm^{-1}. [106]

For elucidating the mechanical properties of ZnO NWs in the presence of an impinging e-beam, we used two distinct setups, detailed in the following sections.

4.2 Dark-field Optical Microscope Set-up

The dark field setup did not employ an e-beam for visual detection of the oscillatory motion. As shown in Fig. 4.3a, a cantilevered ZnO NW (800 nm thick) was aligned parallel to an Au-coated W tip using micro-manipulators attached to a dark-field microscope. This arrangement allows the charged tip to serve as the CE for applying an electrical force proportional to the charge present on the tip. The cantilevered ZnO NW is actuated by a tunable AC signal (V_{ac} = 5 – 8 V) applied to the CE, from a signal generator (SRS DS345). The AC signal was swept through the desired frequencies, ranging from 0.5 Hz to 80 kHz, and the resulting oscillations were detected visually using a high-resolution camera (Spot Insight V 3.2) attached to the dark field microscope. The dark-field setup was used to observe the mechanical resonance of as-grown ZnO NWs and Au-coated (thickness ~30 nm) ZnO NWs (Fig 4.3a).

4.3 Scanning Electron Microscope Set-up

In this setup, resonating ZnO NWs were examined using an electron probe beam. The NWs, attached by SEM tape to a tungsten tip, were mounted on a custom made sample stage and loaded into an SEM chamber operating under high vacuum (Hitachi SU6600).

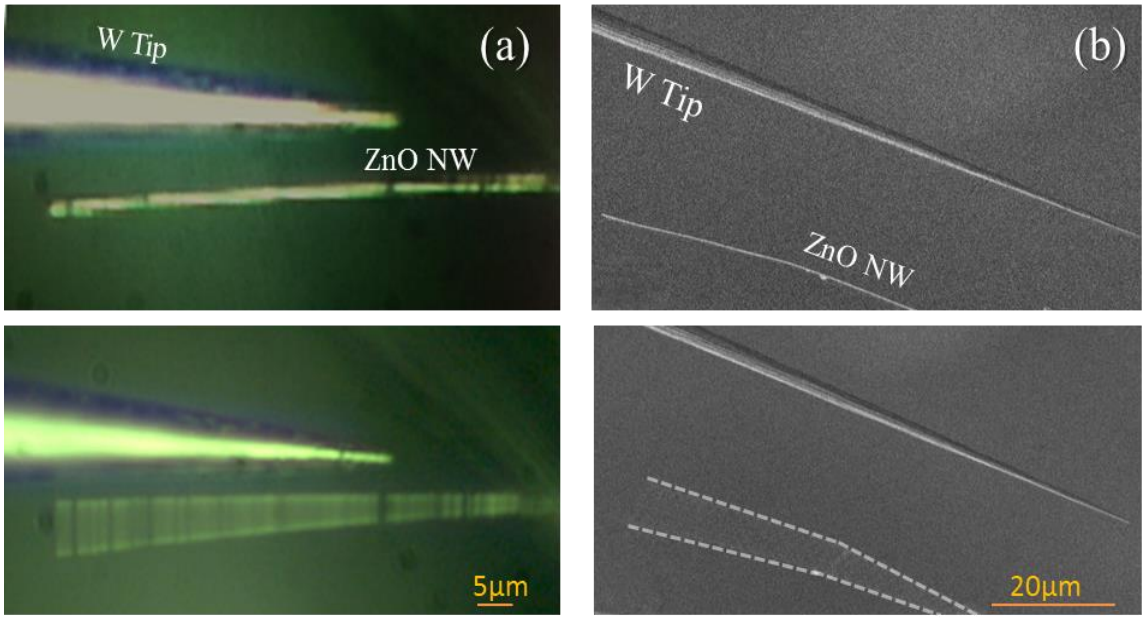

Figure 4.3: Two different microscopes were used in this study: (a) a *dark-field microscope* which uses white light for visual detection of resonance of the ZnO NW and (b) a *scanning electron microscope* which uses an e-beam for visual detection. The ZnO NW is off resonance in the top images in panels (a) and (b), and in resonance in the corresponding bottom images. The dashed lines in the bottom panel of (b) serve as a guide to the eye. [106]

For a more precise parallel alignment of the ZnO NW with the CE (Fig. 4.3b), a PI Block Nano Positioning piezodriven stage was used (see Appendix B). The electrical signal from the cantilever was collected using the electrical feed-throughs into the SEM chamber**.** The accelerating voltage was varied from 5 kV – 20 kV and the emission

current was fixed at 32 μA. The e-beam was incident in a nearly perpendicular direction to the NWs, and the images were captured using the secondary electrons.

We first examined the motion of as-grown and Au-coated ZnO NW cantilevers under high driving voltages (5-8 V) at very low frequencies (~ 1 Hz) under the dark-field microscope setup Interestingly, the as-grown ZnO NWs oscillated at the driving frequency, while the Au-coated ZnO NW oscillated at twice the driving frequency, the latter behaving similar to a conducting cantilever (Fig 2.8). Only a small charge can be induced onto the as-grown ZnO NW.

For a static charge on a semi-conducting ZnO NW, the force on the NW due to a charged CE a distance z from the cantilever is proportional to $Q_{NW}Q_{CE}/z^2$, Q being the respective charge in the NW or CE, and oscillating at the frequency of the voltage $V_{dc} + V_{ac}\cos(\Omega t)$ applied to the CE. In this case negligible current flows are implied and we see no charge flowing to and from the cantilever.

For a dynamic charge induced on a grounded conducting NW, the force on the NW is equal to the derivative of the energy ½ CV^2 stored in the capacitor (C) formed by the NW and the CE with respect to the distance z between the NW and the CE. This gives a force proportional to $dC/\mathrm{dz}\{V_{\mathrm{dc}}{}^2 + 2V_{\mathrm{dc}}V_{\mathrm{ac}}\cos(\Omega t) + \tfrac{1}{2}V_{\mathrm{ac}}{}^2[1 + \cos(2\Omega t)]\}$ which oscillates at both the frequency applied to the CE and at twice that frequency. In this case we see current flowing to and from the cantilever, with maxima at both the resonance frequency of the cantilever system and at half that frequency.

4.4 Results and Discussions

The mechanical response of ZnO NWs at low frequency suggests that the as-grown ZnO NWs follow the static charge mechanism in contrast to the dynamic charge induction observed in the Au-coated ZnO NW. Although a mechanical resonance was visually observed for both cantilevers under the dark field microscope, the as-grown ZnO NW cantilever had noticeably lower amplitude of vibration compared to the Au-coated NW. Importantly, only the Au-coated ZnO NW produced an observable electrical signal (Fig. 4.4).

At higher frequencies (up to 80 kHz), the amplitude of any other induced vibrations at atmospheric pressure was smaller than we could observe (~ 100 nm). The inset (Fig. 4.4) is a the Skove plot. A nearly circular polar plot validates the detection of electrical resonance. The low-frequency oscillatory behavior and absence of an electrical signal from as-grown ZnO NW (in the dark-field microscope setup) may be explained in terms of its wide band-gap and the static charge mechanism (discussion in section 2.4). Previous reports have ascribed dynamic charge induction as the fundamental mechanism for the oscillatory motion in ZnO NWs.[117, 138]

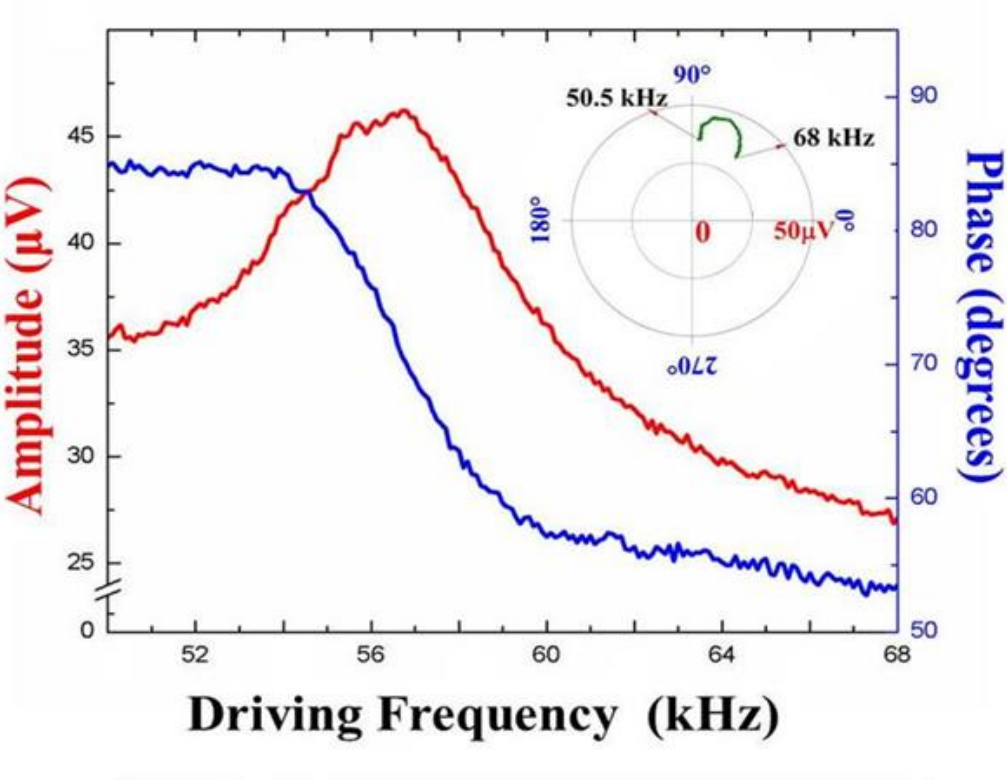

Figure 4.4: The 2nd harmonic HDR signal from a resonating Au-coated ZnO nanowhisker (amplitude-red; phase-blue). The resonance was detected, for both as-grown and Au-coated ZnO NWs under the optical microscope setup but the electrical signal was observed only for Au-coated ZnO NW. The inset is a Skove plot that shows the measured amplitude (r) and phase (θ) in a polar co-ordinate system. A nearly circular polar plot validates the detection of electrical resonance. [106]

It is worth noting that such experiments were performed in the presence of an e-beam (unlike the dark-field setup) and many of the proposed applications of ZnO NWs are based upon devices working under ambient conditions. Hence, it is important to decouple the e-beam effects from the intrinsic properties of ZnO NWs. To achieve this objective,

we next examined the mechanical response of as-grown ZnO NWs in the SEM setup described above.

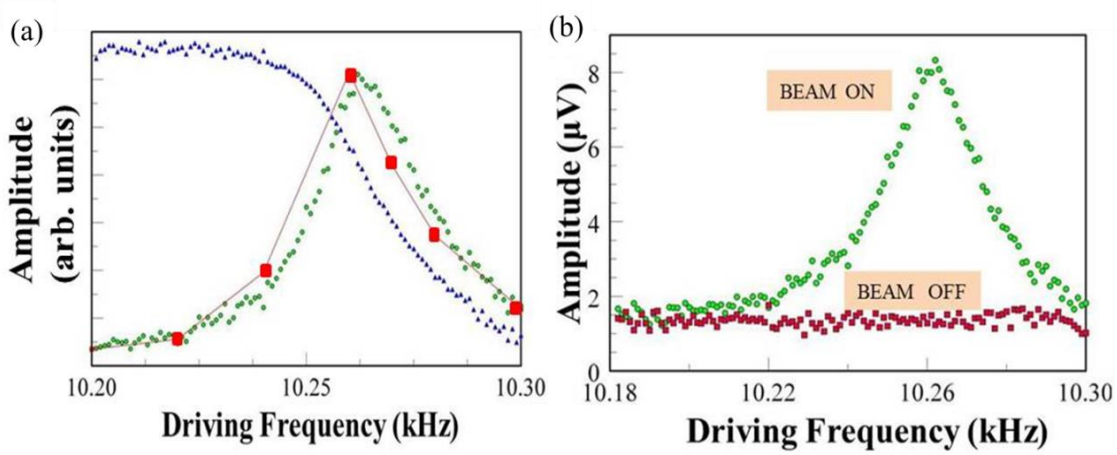

Figure 4.5: (a) Comparison of the squared "visual" amplitude in an SEM (red squares) and the electrically detected signal (green dots) of the mechanical motion of the as grown ZnO NW. The visual detection is done by measuring the physical amplitude of oscillation in the SEM. Clearly, the *Q-factor* of the electrical signal is comparable to the squared "visual" signal, highlighting the accuracy of the HDR measurement. Additionally, HDR provides the phase (blue triangles) of the cantilever motion which cannot be obtained visually. (b) Under the electron beam, HDR exhibited a resonance peak for the as-grown ZnO NW, and this peak vanished when the beam was turned off. [106]

The oscillatory motion of the as-grown NW was clearly seen in the SEM setup (Fig. 4.3b). Interestingly, a corresponding electrical signal was also observed for the as-grown ZnO NW in the SEM setup under similar driving conditions to those used in the dark-

field setup. Fig 4.5a shows that the magnitude of the electrical response scales almost exactly with the square of the observed mechanical amplitude, highlighting the correspondence between the two. In addition, the electrical signal allows the observation of the relative phase of the motion and further improves the sensitivity of the measurement of resonant behavior.

Remarkably, we did not observe any electrical signal from the as-grown ZnO NW when the e-beam was turned off (Fig. 4.5b). We found that the oscillatory motion of the as-grown NW (and hence the HDR output) is influenced by the interaction between the e-beam and the NW. We varied the SEM magnification and measured the resulting HDR output across the resonance frequency to confirm the effects of e-beam incidence on the HDR output signal. The behavior of NWs (as a function of magnification) may be categorized into three different regimes viz., low, medium and high magnification. Interestingly, no HDR output could be observed in the low magnification regime (1x-2000x). As shown in Fig. 4.6, the HDR output increases rapidly with increasing magnification in the medium magnification regime (2000-4000x). Above 4000x magnification the electrical amplitude could no longer be precisely determined as nonlinearities (for example, the Duffing[84, 139] behavior described in Fig. 5.8) associated with large cantilever deflection obscured the peak height of the HDR signal. The SEM magnification is the ratio of view screen area (computer screen) to the scanned sample area[140]. The raster coils (in the SEM) scan the sample line by line, left-to-right and top-to-bottom, much like reading a book. A higher magnification (achieved by

reducing the scanning area) increases the e-beam scan frequency. Consequently, increasing the magnification increases the interaction of the NW with the e-beam. Beyond a threshold magnification (2000x in this case), the interaction is strong enough to induce observable current (hence finite HDR output) into the sample. Furthermore, in the high magnification regime (> 4000x), the induced currents are sufficiently high to cause non-linearity in the NW motion.

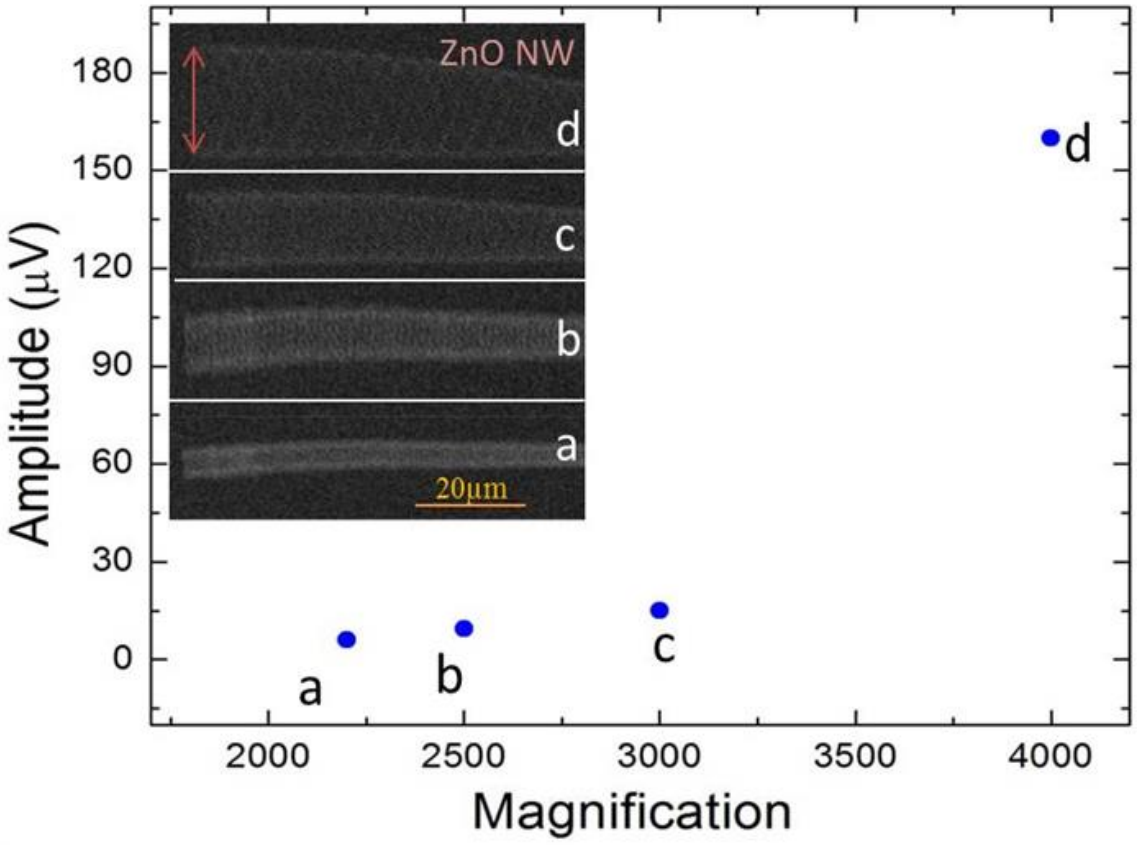

Figure 4.6: (a) A plot of the maximum electrical amplitude as a function of e-beam magnification *x*. The SEM images in the inset figure suggest a direct correlation between the measured electrical amplitude and the observed amplitude of the oscillating NW.

The results described in the preceding paragraph can be rationalized from the infrared spectrum depicted in Fig. 4.7. Several absorption peaks are present in the range of 1000-4000 cm^{-1} for as-grown ZnO NWs. The broad band at ~3500 cm^{-1} is attributed to chemisorbed hydroxyl groups (due to its hygroscopic nature) on the ZnO NW surface. The C-H stretch peaks at ~2800 cm^{-1}, symmetric and asymmetric carboxylate peaks at ~1385 cm^{-1} and 1630 cm^{-1} originate from reactive carbon-containing plasma species (from $Zn(Ac)_2$) physisorbed on the ZnO NW surface during synthesis. When exposed only to the relatively weak oscillating driving voltage (as in Fig. 4.3a), these polarized functional groups attached to NW may act as static bound charges and cause ZnO NW to oscillate at the same frequency as the driving frequency, consistent with the static charge mechanism (Fig. 2.8). However, as has been recently shown, e-beam irradiation in the SEM chamber (few kV) can increase ZnO NW's electrical conductivity by generating electron-hole pairs across its band gap of ~3.37 eV.[121] Thus, an increase in the SEM magnification leads to an increase in the electrical conductivity of the ZnO NW. Consequently, in the presence of the e-beam, the magnitude of both the electrical signal and the mechanical motion are significantly amplified due to dynamic charge induction that drives the ZnO NW at twice the driving frequency. In addition, this dynamic flow of charge gives rise to an electrical signal (Fig. 4.5).

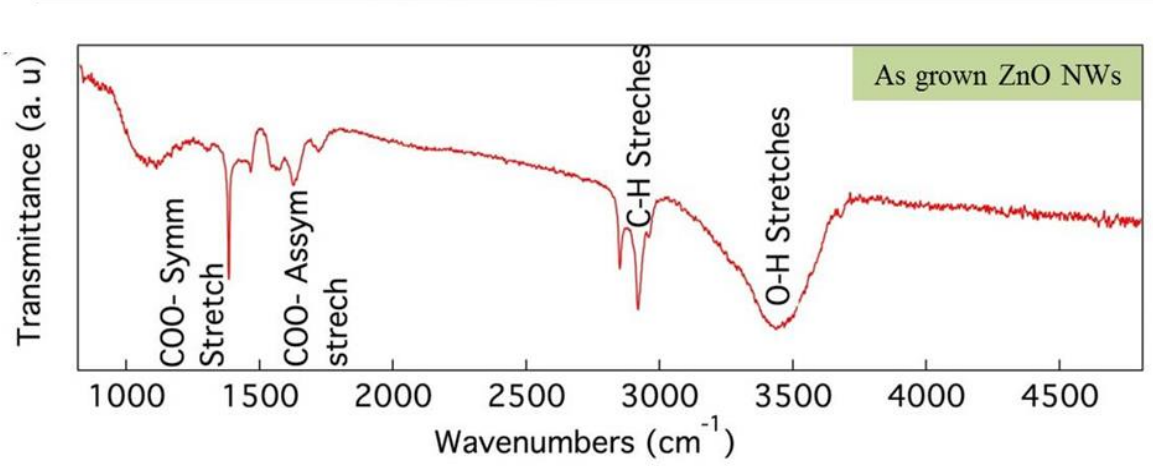

Figure 4.7: The infrared transmission spectrum of as-grown ZnO NWs reveals the nature of the many functional groups present on the surface of the NW. [106]

We note that the resonance peak at higher amplitudes shows non-linear effects (Duffing effect) (Fig. 4.8a). In this work the nonlinearities result in the peak amplitude occurring at higher frequencies with increasing amplitude, implying that there is a "spring hardening," rather than the spring softening seen in similar cantilevers at ambient and lower pressures. We expect the forces due to static charges to lead toward smaller spring softening than dynamic charges, which are always attractive between the cantilever and the counter electrode. Further studies are needed to understand the source and mechanism of the observed frequency increase.

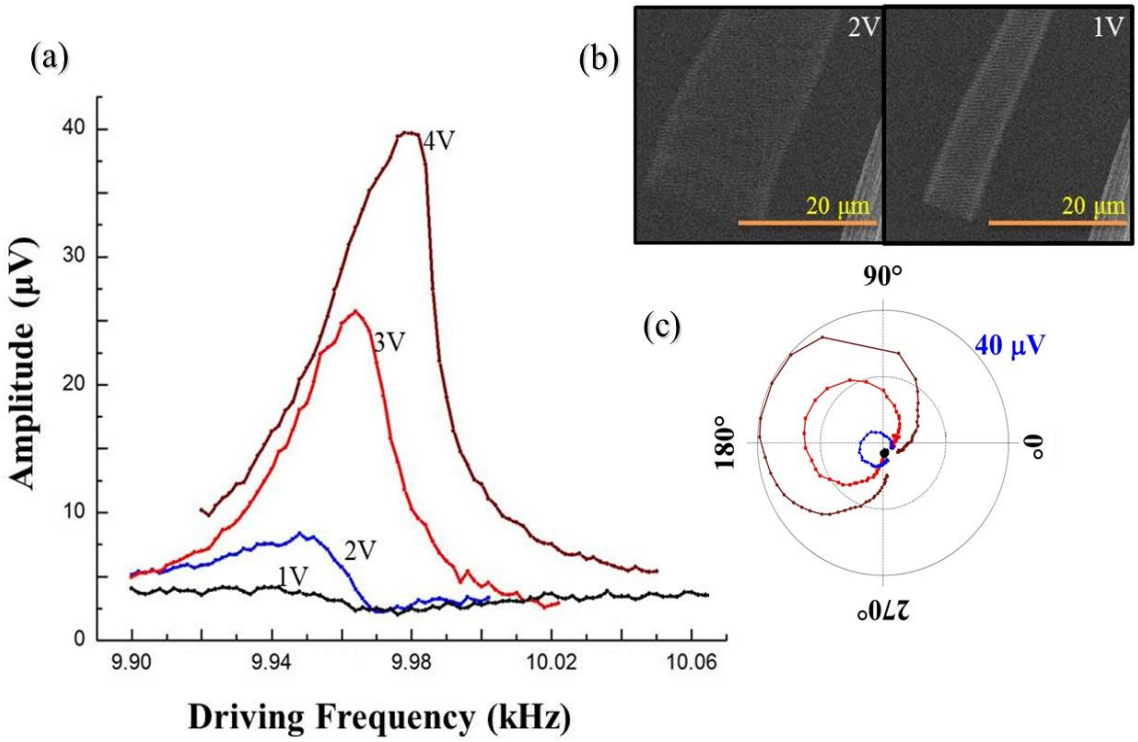

Figure 4.8: (a) The 2nd harmonic HDR signal of an as-grown ZnO NW (driven into resonance inside the SEM at a magnification of 2500x) as a function of the frequency of driving *ac* voltage. The observed asymmetry in the resonance peaks is due to the nonlinear oscillatory motion of the NW at a higher input voltage. Note that the Duffing-like nonlinearity drives the peak amplitude to higher frequencies, unlike what is generally observed for the other conducting nanostructure cantilevers[141]. (b) SEM images of a resonating ZnO NW at 2 Vp-p and 1 Vp-p *ac* signal. (c) Skove plots corresponding to the 2nd harmonic signals depicted in (a). For a damped simple harmonic oscillator the Skove plot is a circle. The non-circular Skove plots at higher voltages indicate the presence of increasing non-linearity at high actuation voltages. [106]

Heuristically, we can envision two distinct domains of NW oscillation as a function of the incident beam intensity. At low or no beam intensity (the static charge region), bound charges from polarized surface groups on the NW will dominate the driving mechanism. The physical motion will be constant with respect to intensity and the electrical and visual signals will be extremely small, virtually undetectable in all but the largest whiskers. For large beam intensities, sufficient free carriers can be generated, and the resonance will fall in the dynamically induced charge regime, with both the mechanical and electrical signals increasing with beam intensity. The exact oscillatory behavior of a given NW will depend on its density of surface-trapped holes, and on carrier density. [121]

4.5 Conclusion

We have presented a model, involving both static and induced charge mechanisms, to explain the observed resonance behavior of an electrostatically driven ZnO NW. The importance of checking the low frequency response of the cantilever to verify a static or dynamic actuation mechanism was discussed. Evidently, a semi-conducting as-grown ZnO NW yields a real-time electrical signal and provides a high precision amplitude signal in the presence of an e-beam, implying that the interaction of semi-conducting nanostructures with electron probe beams modifies their intrinsic electronic properties, and has led to incorrect identification of the actuation mechanism.

CHAPTER 5

PROBING MECHANICAL RESONANCES OF HELICALLY COILED NANOWIRE

5.1 Methods

In order to probe the mechanical behavior of the coiled cantilevers, we first synthesized a forest of randomly oriented HCNWs using a previously reported two–stage, liquid precursor based, thermal CVD method.[12] These as-prepared HCNWs were characterized using SEM (Hitachi SU-6600) and TEM (Hitachi 9500), see Fig. 5.1.

For HDR experiments, an isolated HCNW mounted on an electrochemically etched W-tip was used as the cantilever (see Appendix B for the set up). The W-tip was brought into contact with a double-sided conducting carbon adhesive tape (PELCO Tabs^{TM}; Ted Pella) and then used to isolate a single HCNW from a forest. The tip was then mounted on the SEM jig (Appendix B). The HDR setup was used within either an SEM chamber (Hitachi SU-6600 or S-3400) to provide a stable vacuum (< 1 Pa) which mitigated damping losses, or a dark-field optical. Importantly, the mechanical resonances observed under the SEM were simultaneously detected "electrically" using the HDR method. For all experiments discussed below, V_{dc} was held constant at 9 V while V_{ac} was varied within ± 9V. Briefly, in the HDR method, a cantilever is actuated by either static or dynamic charge induction depending on several factors such as the presence of static charges,

functional groups, and the intrinsic electrical conductivity of the cantilevered structure. In the absence of V_{dc}, the dynamic (static) charge induction mechanism often resulted in a vibration at twice (same) the driving frequency for well-grounded electrically conducting cantilevers.[106] Accordingly, the motion of a cantilevered HCNW was observed at ~1 Hz under the dark-field optical microscope to confirm the presence of the dynamic charge induction mechanism (see section 4.3 for the rationale) and ensure that the HCNW was properly grounded. However, HCNWs were always found to be positively charged when exposed to an electron beam, possibly due to the ejection of electrons. Nonetheless, the HCNWs were found to be neutral when the electron beam was turned off, as observed from our dark-field experiments.

In previous studies, we found a strong correlation between the presence of structural defects and the mechanical properties of nano-cantilevers in particular MWNT.[142] In view of this correlation and to eliminate the effects of sample heterogeneity in this study, all HCNWs were consistently selected from the same synthesis batch (HCNW1- HCNW4 shown in Table II). It is worth noting that the harmonics and resonance modes overlap in the traditional doubly clamped geometry, *e.g.*, strings in a guitar; therefore, we used the singly clamped geometry to distinguish the resonance modes of HCNWs from their harmonics.

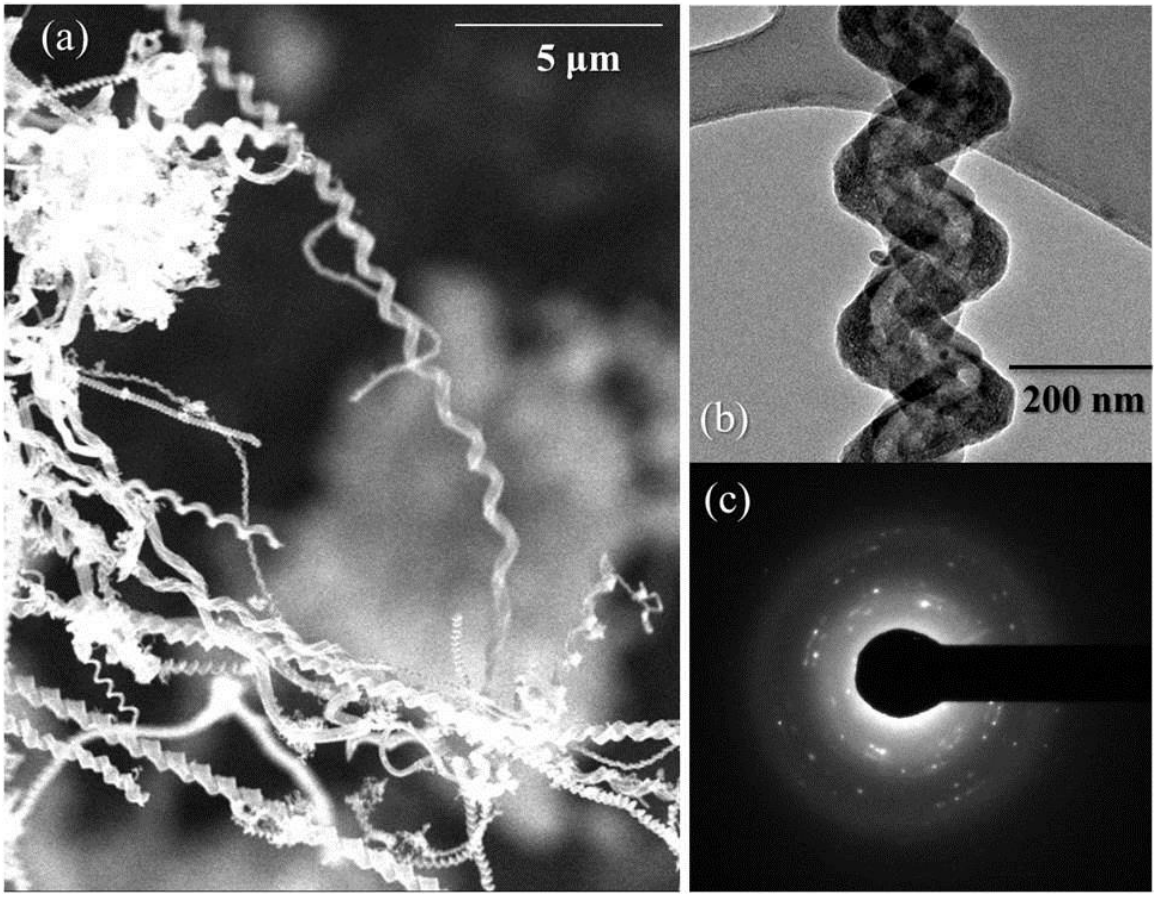

Figure 5.1: (a) Scanning electron microscope image of as-prepared HCNWs. (b) The coiled structures are solid wires as evident in the TEM image. (c) The selected area diffraction pattern reveals a polycrystalline structure of HCNWs.

The transverse resonance frequency (f) of a singly clamped cantilever can be calculated by the well-known relationship, $f = 1/2\pi\ (k/m_{eff})^{1/2}$ where k is the spring constant and m_{eff} is the effective mass of the cantilever.[143] In contrast to a straight cantilever, k for the transverse bending mode of a HCNW is a function of both E and G of the material, which makes it difficult to compute the resonance frequencies. This motivated us to adapt the

following protocol (Fig 5.2) to obtain an experimentally validated closed form expression for resonance frequency (f_{ANA}). We employed the HDR method to obtain the frequencies of first two modes (f_1 and f_2) of HCNWs and deduced their shear modulus by simultaneously validating experiments with analytical and numerical models.

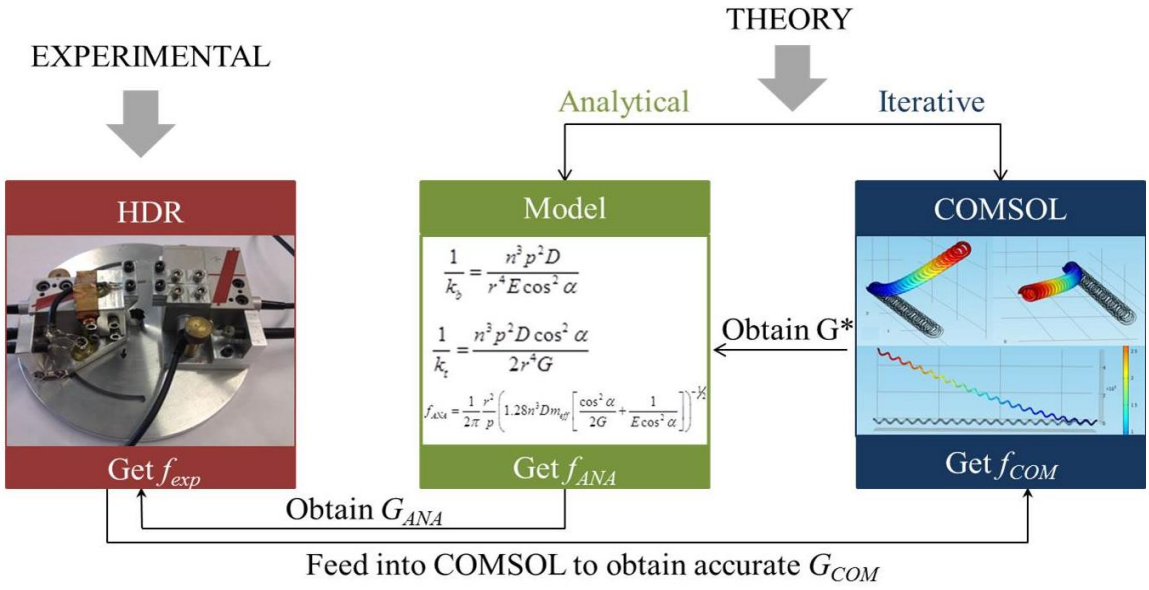

Figure 5.2: Protocol followed for probing the mechanical resonance of helically coiled carbon nanowires. The experimental technique (HDR) is used in tandem with analytical and iterative (finite element analysis based COMSOL® simulation) methods used for determining the shear modulus of the coiled cantilever.[107]

5.2 Modeling:

To begin with, the HCNWs were analytically modeled, primarily to understand the contribution of the twisting and bending upon application of a transverse moment on a coiled geometry. [107]

For further discussion, the following labels for the physical parameters of a HCNW are introduced (Fig 5.3):

r- radius of the wire;

D- diameter of HCNW;

p- pitch of HCNW;

n- number of turns;

l- length of HCNW (note that $l = n.p$);

M- Moment experienced by a turn of the HCNW upon bending with a radius of curvature γ; and α-pitch angle of HCNW.

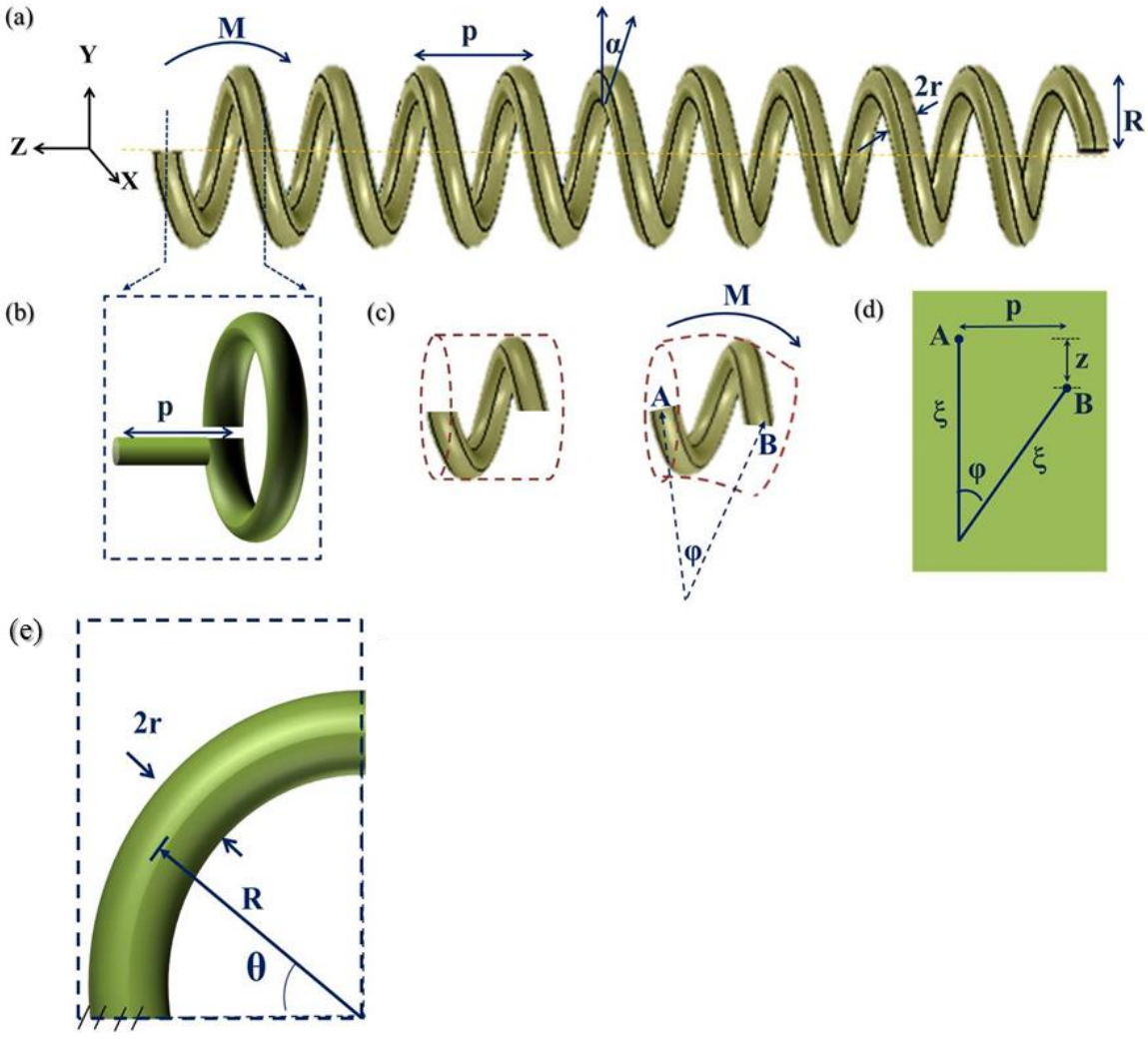

Figure 5.3: (a) Geometrical parameters of an HCNW (b) One turn of the coil modeled as a planar ring connected with a rigid rod, compensating for the pitch. (c) Left panel - one turn of the coil with no moment. Right Panel - Bending of the coil under moment M. An imaginary cylinder (dashed lines) is a guide to understand the bending mechanism. (d) Vector diagram of the displacements upon bending as seen in (c) (e) Dimensions of a quarter of a turn of the HCNW.[107]

Initially, one turn is considered under a moment (*M*) in the plane of the HCNW axis. To simplify the model, we approximated one HCNW turn as a planar ring connected with a rigid rod (Fig. 5.3b) as shown by Wahl.[144]. The deflection angle φ_q of a quarter turn of the coil (5.3 e) is a sum of the deformation due to bending ($\varphi_{b)}$ and torsional strain (φ_t) under moment M. The component of φ_q due to the bending strain (φ_b) is

$$\varphi_b = \frac{1}{EI}\int_0^{\pi/2} M\sin\theta\frac{D}{2}d\theta\sin\theta = \frac{MD}{2EI}\int_0^{\pi/2}\sin^2\theta d\theta = \frac{\pi MD}{8EI} \quad (5.1),$$

where $I = \pi r^4/4$ is the area moment of inertia, $M\sin\theta$ is the component of *M* along the axis of the wire, and the additional $\sin\theta$ is the ratio of φ to the component of bending in the plane of the wire, and θ is the angle along the quarter turn of the coil. Similarly the component of φ_q due to the torsional strain (φ_t) due to the moment *M* is:

$$\varphi_t = \frac{1}{GJ}\int_0^{\pi/2} M\cos\theta\frac{D}{2}d\theta\cos\theta = \frac{MD}{2GJ}\int_0^{\pi/2}\cos^2\theta d\theta = \frac{\pi MD}{8GJ} \quad (5.2),$$

where $J = \pi r^4/2$ is the polar moment of inertia, $M\cos\theta$ is the component of the moment *M* along the axis of the wire, and the additional $\cos\theta$ is the ratio of φ to the component of bending in the plane of the wire.

At larger pitch angles, the bending and twisting components of the HCNW are convoluted i.e. the twisting portions experience an additional bending. Hence, to compensate for this effect, we introduce a factor $\cos^2\alpha$ to the denominator of φ_b *(for*

increased bending) and to the numerator of φ_t (for reduced twisting). (See computational analysis section for details). Thus the equations (5.1) and (5.2) become

$$\varphi_b = \frac{\pi MD}{8EI\cos^2\alpha} \; ; \; \varphi_t = \frac{\pi MD\cos^2\alpha}{8JG} \qquad (5.3).$$

For a complete turn, the total deformation φ (under the M) = $4(\varphi_b + \varphi_t)$ *yielding*

$$\varphi = \frac{\pi MD}{2EI\cos^2\alpha} + \frac{\pi MD\cos^2\alpha}{2GJ} \qquad (5.4),$$

where the first turn is bending ($4\varphi_b$) and the second turn corresponds to shear deformation ($4\varphi_t$).

The spring constant *k* for a complete turn of the coil is defined as *F*/*z* where *F* is the force acting on a single turn, and *z* is the displacement resulting from *F*. *F* is related to the moment by *F* = *M*/*p*, where *p* is the pitch of coil. From Fig.5.3d, z may be expressed as

$$z = \xi - \xi\cos\phi \qquad (5.5).$$

Using the small angle approximation, we know that

$$p = \xi\phi \qquad (5.6)$$

Hence, from equations (5.5) and (5.6) we obtain the following

$$z = \frac{p}{\phi}(1-\cos\phi)$$

.

The series expansion of cos ϕ yields:

$$\cos\phi = 1 - \frac{1}{2}\phi^2 + \frac{1}{24}\phi^4 - \ldots$$

Under small angle approximation we can neglect the fourth and higher order terms. Thus we get

$$z = \frac{p}{\phi}\left(\frac{\phi^2}{2}\right)$$, that gives

$$z = p\left(\frac{\phi}{2}\right) \quad (5.7).$$

Combining these relations we obtain:

$$\frac{1}{k} = \frac{zp}{M} = \frac{\varphi}{M}\left(\frac{p^2}{2}\right) \quad (5.8).$$

On substituting φ *(equation 54)* in equation (5.8), we get tensile and shear spring constants for one complete turn.

$$\frac{1}{k_b} = \frac{p^2 D}{Er^4 \cos^2\phi} \quad (5.9),$$

$$\frac{1}{k_t} = \frac{p^2 D \cos^2\phi}{2Gr^4} \quad (5.10).$$

Finally, to obtain the combined spring constant we use the relation for adding springs in series:

$$\frac{1}{k} = \frac{1}{k_b} + \frac{1}{k_t} \quad (5.11),$$

which was validated by comparing to iteratively calculated resonance frequencies (see Fig 5.2).

Note that k is inversely proportional to the cube of the length for cantilever beams. Hence, an n^3 term was incorporated to accommodate the total number of the turns in the coil. The relation between number of coils n and k was verified using COMSOL® as follows:

We modeled an HCNW in COMSOL® and systematically varied n (and thus the length), keeping other geometrical parameters constant. We then calculated the mass of the COMSOL® generated HCNW by calculating its volume within COMSOL® and multiplying it with input material density. The f_{COM} for each of the HCNWs was obtained using the formula; $f=1/2\pi(k/m_{eff})^{1/2}$, we were able to calculate the corresponding k. Clearly from data fit (Fig. 5.4), k is directly proportional to n^{-3}.

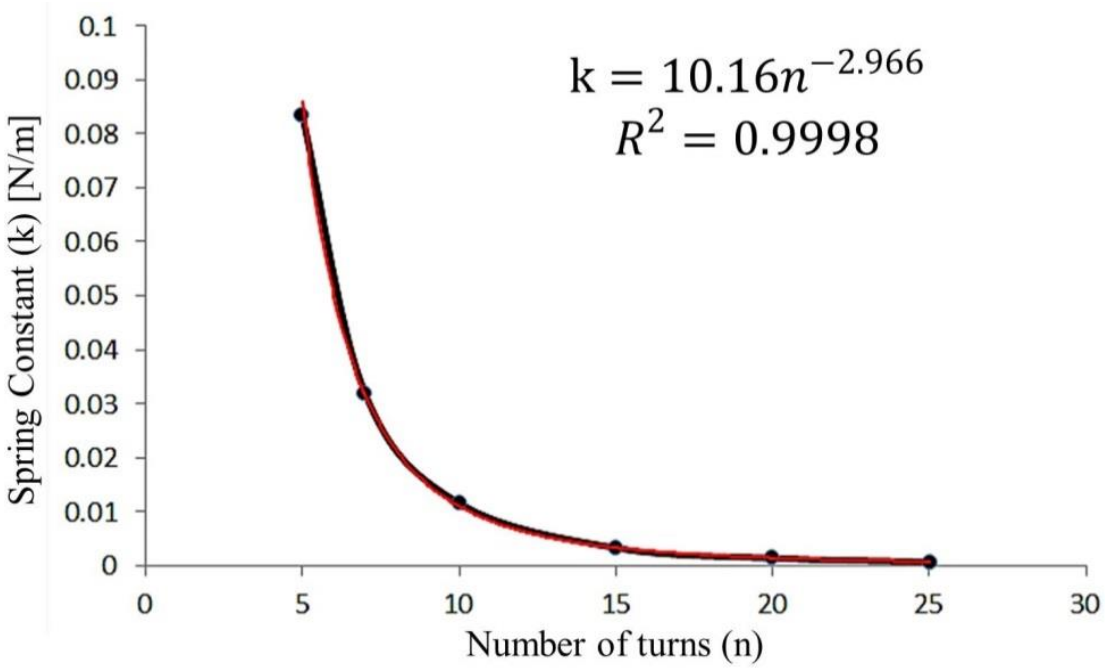

Figure 5.4: Spring Constant (*k*) vs number of turns (*n*) plot. The fitting clearly indicates that *k* varies with n^{-3}.*[107]*

Following the above analysis, for a HCNW of *n* turns, we can obtain the spring constant from equations (5.2) and (5.3) by incorporating an n^3 term. Thus, we get

$$\frac{n^3}{k_{turn}} = n^3\left[\frac{1}{k_b}+\frac{1}{k_t}\right] = \frac{1}{k}$$, yielding

$$\frac{1}{k} = \frac{n^3 p^2 D}{E r^4 \cos^2\phi} + \frac{n^3 p^2 D \cos^2\phi}{2Gr^4} \quad (5.11).$$

Hence, we can then obtain f_{ANA} as

$$f_{ANA} = \frac{1}{2\pi}\frac{r^2}{p}\left(n^3 D m_{eff}\left[\frac{\cos^2\alpha}{2G} + \frac{1}{E\cos^2\alpha}\right]\right)^{-1/2} \quad (5.12),$$

Similar to above analysis, on comparing the f_{ANA} and f_{COM} for different pitch angles, the $cos^2\alpha$ factor was obtained.

Next, we simulated the resonance frequency f_{COM} for various HCNWs with different geometric parameters (n, r, D, p). Based on our COMSOL® results, f_{ANA} matched within 12 % of f_{COM}. Thus the f_{ANA} was scaled by a dimensionless factor s = 0.88 to minimize the deviation from f_{COM}. The scaling accounts for the simplification of a HCNW to a planar ring attached to a rigid rod. Thus, we get the final expression

$$f_{ANA} = (0.88)\frac{1}{2\pi}\frac{r^2}{p}\left(n^3 D m_{eff}\left[\frac{\cos^2\alpha}{2G} + \frac{1}{E\cos^2\alpha}\right]\right)^{-1/2} \quad (5.13).$$

This closed-form expression (equation 5.13) is a solution for HCNW resonance frequency, which includes the effects of both E and G. As described in Fig. 5.2, experimentally obtained resonance parameters of HCNWs can be used in conjunction with equation 5.13 to obtain an estimate of G. It is noteworthy that equation 5.13 is not limited to HCNWs and may be used to estimate the G (or f) of any helically coiled geometry whose E and f (or G) are known.

5.3 Measuring Resonance Parameters

The flexural spring constant of HCNWs is expected to be lower than its axial spring constant due to their moderately high aspect ratio (ratio of length to diameter of the HCNW~10^2). Hence, the probability of actuating transverse resonance modes (perpendicular to the HCNW axis) is much higher relative to axial modes (parallel to the HCNW axis). Figs. 5.5a-5.5c and 5.5d-5.5e show the transverse modes for two different HCNWs, HCNW1(*r*- 64 nm; *D*-290 nm; *p*- 876 nm, *l*-13.35 μm) and HCNW2(*r*-142 nm; *D*-750 nm; *p*-1116 nm; *l*-26.78 μm). A direct *visual* examination under the SEM revealed that the HCNW1 (HCNW2) resonated at frequency f_1~30 kHz (82.35 kHz) at its first mode (Fig. 5.5b) and at f_2 ~190 kHz (547 kHz) at its second mode (Fig. 5.5c). The corresponding HDR amplitude signal for the first mode of HCNW2 (excited with 5 V_{ac} at ~1 Pa; Fig. 5.5f) showed a single transverse resonance peak with a *Q-factor* of ~150.

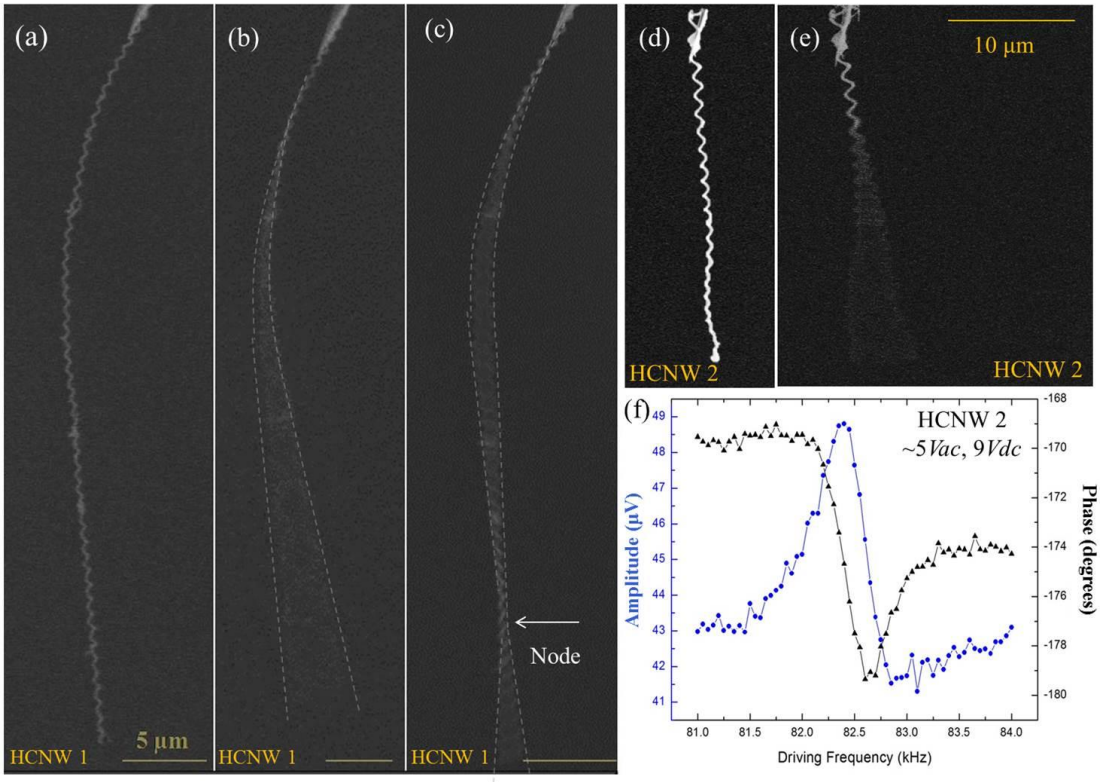

Figure 5.5: SEM image of a singly clamped HCNW (HCNW1- radius 64 nm; coil diameter 290 nm; pitch 876 nm): (a) off resonance, (b) first transverse mode at driving frequency f_1 ~ 30 kHz, (c) second transverse mode at driving frequency f_2 ~190 kHz. (d) Off resonance SEM image of HCNW2 (radius 142 nm; coil diameter-750 nm; pitch 1116 nm) (e) First transverse mode (f_1 ~ 82.5 kHz). (f) HDR signal for transverse mode for HCNW2 with driving voltages V_{ac} = 5 V , V_{dc} = 9 V. The resonance amplitude peak (blue) is similar that of a Si microcantilever. The black trace represents the phase signal. The dotted lines in (b) and (c) serve as a guide for the eye.[107]

To examine the coupling between bending and shearing moduli of 'geometrically' nonlinear HCNW cantilevers, we actuated HCNWs at a higher driving force by either increasing the ac driving voltage (~ $8V_{ac}$) or reducing the gap distance between HCNW and the CE. A higher driving force was observed to result in 'mechanical' nonlinearities such as the characteristic Duffing-like jumps in cantilever motion (see Fig. 5.7). Interestingly, as shown in Fig. 5.6, we found that: i) the HCNWs resonated in a non-planar circular mode when the driving voltage was increased > $8V_{ac}$ (or the gap distance is reduced < 5 μm), and ii) simultaneous with the observation of the circular mode, the HDR amplitude signal exhibited a bifurcation (Fig. 5.8) of an otherwise single transverse resonance peak (Fig. 5.5f).

Through visual comparison, we confirmed that the lower (higher) frequency peak corresponded only to the planar transverse (non-planar circular) resonance. As we varied the driving frequencies (from 85 to 95 kHz), we observed the onset of the non-planar modes between 90-94 kHz, and a clear rotation of the plane of resonance (circular mode as seen in Fig. 5.6). As shown in Fig. 5.7, the onset of non-planar motion was also evident for an independent HCNW3 (*r*-103 nm; *D*-330nm; *p*- 1.104μm; *l* - 44 μm). During the reverse frequency sweep, we observed a typical hysteresis (as indicated by the hatched area in Fig. 5.8) associated with mechanical nonlinearities (i.e., non-planar circular mode).

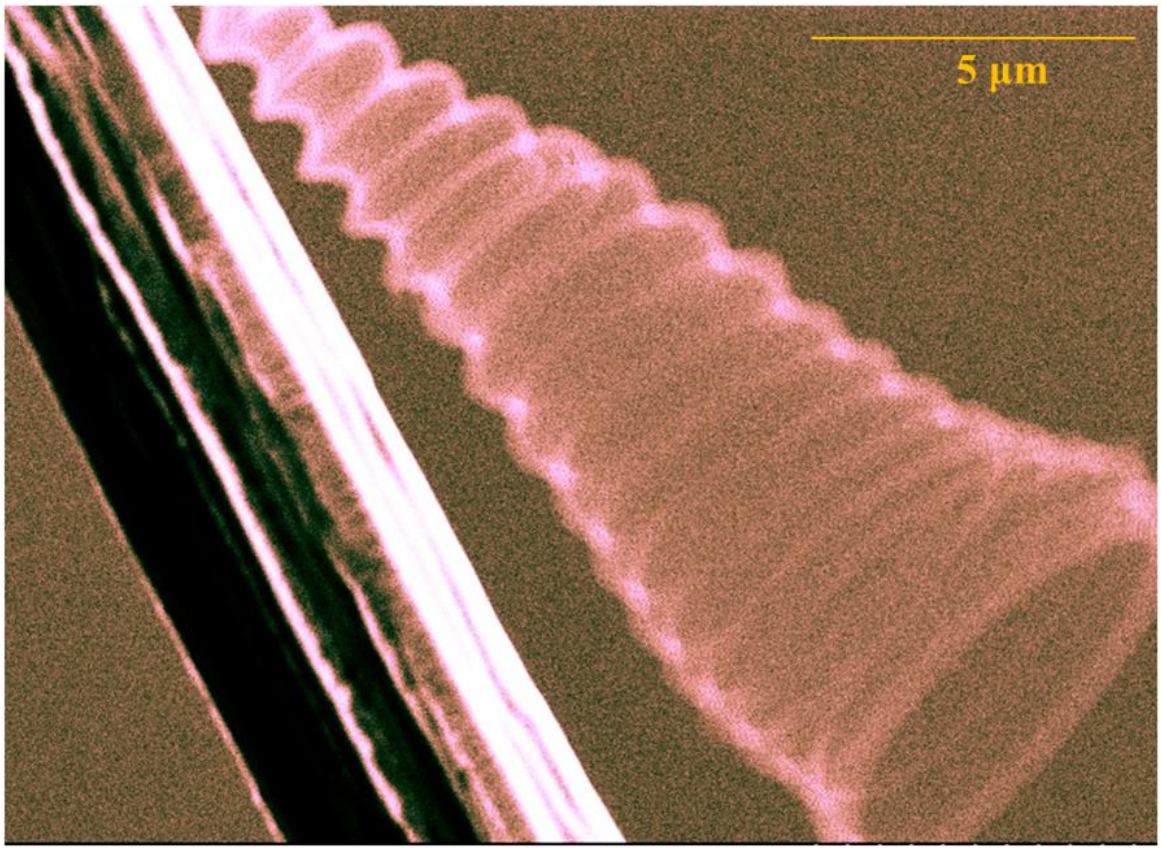

Figure 5.6: (a) SEM image of HCNW2 resonating in circular mode at a driving signal ~ 94 kHz.[107] (*Note: This figure was highlighted on the cover of the Clemson Glimpse magazine in 2013*).

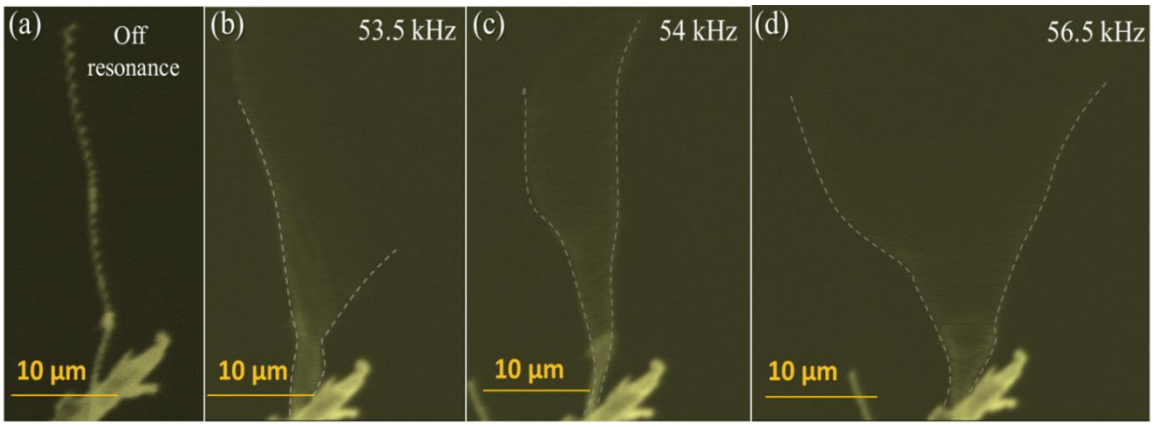

Figure 5.7: The circular resonance behavior can be seen in HCNW3 (wire radius103 nm; diameter 330 nm and pitch 1.014 µm) in (a) off resonance, (b) Ω = 53.5 kHz, (c) Ω = 54 kHz, and (d) Ω = 56.5 kHz, where Ω is the driving frequency. On applying relatively higher driving voltages, the nanocoil actuates in an in-plane transverse mode. On further sweeping the driving frequency, its motion is transformed into an elliptical mode (c) which becomes close to a circular motion when it hits the resonance frequency.

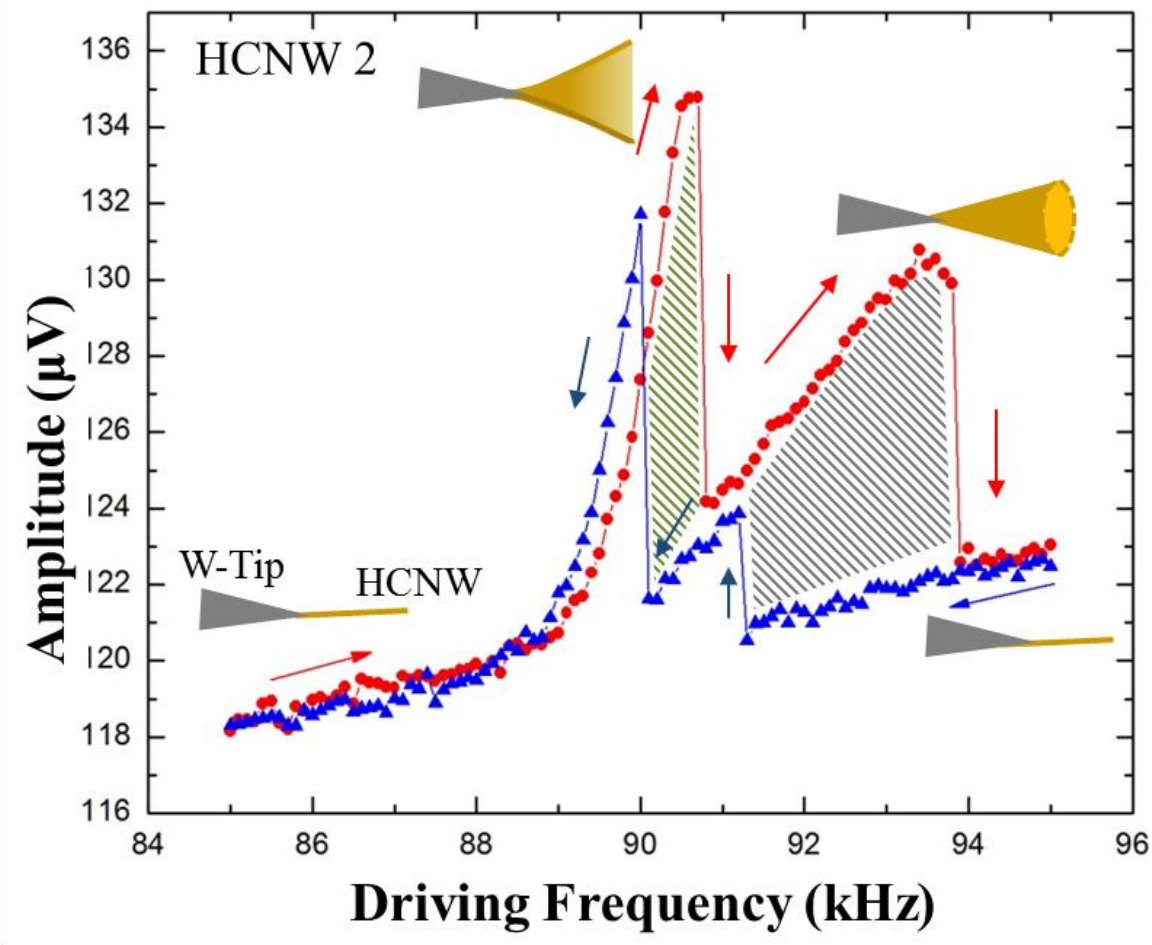

Figure 5.8: HDR signal shows a bifurcation in the resonance signal. The peak at ~90 kHz corresponds to an in-plane transverse resonance that occurs before the onset of the circular mode (peak at 93.5 kHz). [107]

The hysteresis was more prominent for the higher frequency peak or circular mode (gray) relative to the lower frequency peak or transverse mode (green). It is worth noting that the bifurcation of the resonance signal disappeared upon restoring the initial actuation conditions (i.e., V_{ac} ~5V) indicating that the difference between the driving forces

necessary for actuating planar vs. non-planar mechanical modes is significantly low for HCNWs than for straight cantilevers (e.g., multi-wall carbon nanotube or MWCNTs). Indeed, the high actuation threshold for non-planar modes in straight cantilevers has been a major bottleneck in understanding mechanical nonlinearities (e.g., Duffing-like circular modes). Although non-planar modes were reported previously in some straight nanocantilevers[145] (SiC nanowires, MWCNTs and Si nanocantilevers[146]), the necessary driving force was sufficiently large to destroy the samples impeding detailed studies of their nonlinear mechanical behavior. The helically coiled geometry plays a pivotal role in enabling the actuation of otherwise inaccessible non-planar modes at significantly lower ac voltages (~ 8V) due to two reasons: i) a low transverse *k* of HCNWs allows them to bend easily relative to their straight counterparts (e.g., MWCNT); and ii) the inherent asymmetry of HCNWs separates the otherwise degenerate *x*-, *y*-polarizations in mechanical resonance. As described below, our numerical analysis using COMSOL® also confirmed that the helically coiled geometry leads to non-degenerate *x*-, *y*-planar modes that can be actuated simultaneously to produce the observed non-planar modes (Fig 5.9). Although the nature of the electrical force in HDR experiments is such that it favors the excitation of only one of the two (*x or y*) modes, the coupling between bending and shear moduli in a HCNW provides a channel for the exchange of energy between x- and y-modes resulting in non-planar resonance. Therefore, the resonance analysis of other materials (e.g., Si and ZnO) in their helically coiled geometry will allow for elucidating the nonlinear mechanical properties without breaking or destroying the cantilever.

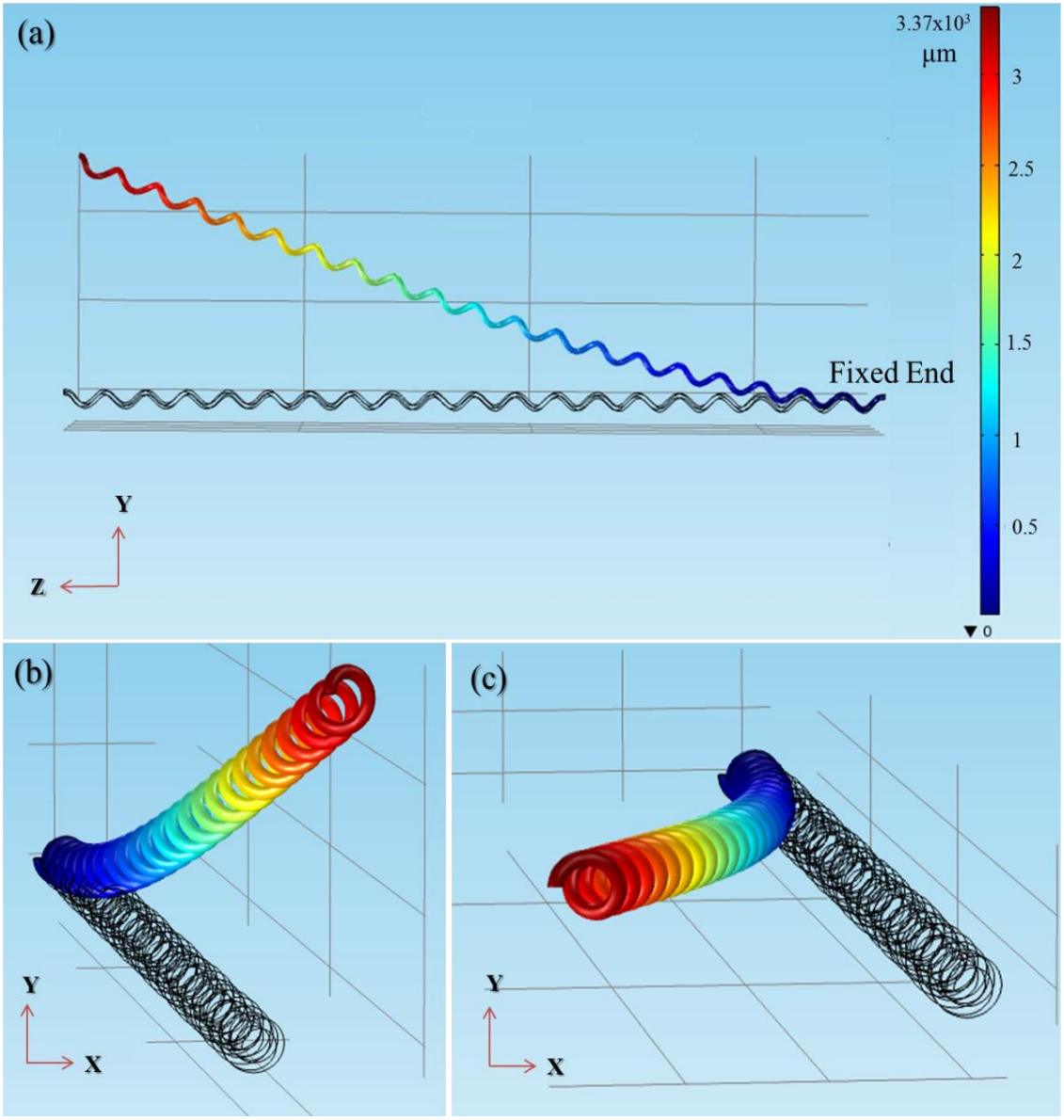

Figure 5.9: COMSOL® Simulated plots of representative helical coil geometry. (a) Off resonance (b) First transverse mode –Y polarization (b) First transverse mode- X Polarization.

We also attempted to actuate a purely axial mode parallel to the axis of HCNW by placing a blunt W-tip in tip-to-tip geometry (3 V_{ac}, 9-10 V_{dc}) with HCNW. However, the parametric nature of the driving force always resulted in an asymmetric combination mode (distinct from the circular mode) consisting of transverse resonance and axial stretching (Fig. 5.10).

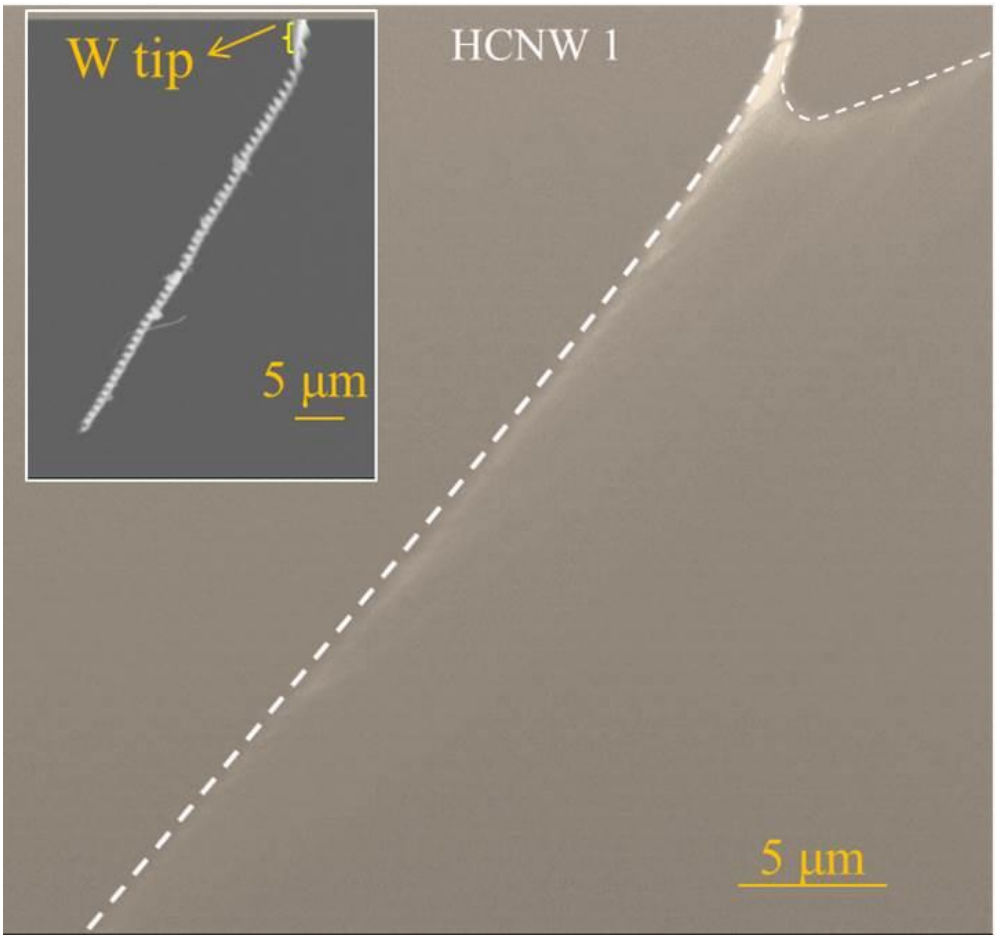

Figure 5.10: SEM images depicting a mixed resonance mode in HCNW1 detected at ~ 29.5 kHz. This asymmetric mode results from the mixing of axial and transverse motions of the nanocoil. The inset depicts the same when the HCNW is off resonance. The dotted line is a guide to the eye.

The analysis of transverse resonance modes in COMSOL® revealed that the ratio of the second and first modes (f_2/f_1) is 6.27- a ratio predicted by EB theory exclusively for straight cantilevers. Our HDR experiments showed that $f_2/f_1 \sim 6.75 \pm 0.38$ for 3 different HCNWs, deviating only slightly from the straight cantilever case, in agreement with COMSOL®. The experimental and COMSOL® results prove that although EB theory is insufficient to predict the motion of HCNWs accurately, the ratio f_2/f_1 is a true transcendental constant independent of the geometry of the resonating cantilever. Such an observation allows us to predict the second mode of transverse resonance by the following relation

$$f_2 = \frac{6.27}{2\pi}\sqrt{\frac{k}{m_{eff}}} \qquad (5.7).$$

The protocol described in Fig. 2.9 was applied to HCNWs to obtain their *G*. The HCNWs isolated for HDR studies were carefully characterized to accurately obtain *r, R, p and n*. We calculated the HCNW resonance frequency (f_{COM}) using Eigen-frequency study under the fixed-free boundary condition and a fine mesh construction for a numerically stable solution in COMSOL®. We used equation 5.6, experimental HDR results, and an estimated E=120 GPa (similar to MWCNTs) to obtain an initial estimate for G_{ANA} for HCNWs. Subsequently, we implemented a series of COMSOL® simulations on HCNWs 1-4 (see Table II) by varying $E \sim$ 80-200 GPa (in steps of ~20 GPa) and G~5-10 GPa (in steps of ~1 GPa) to obtain a f_{COM} that matched f_1. Since there could be more than one set of *E* & *G* values that could result in a $f_{com} \sim f_1$, we used the experimental and COMSOL®

data from HCNWs 1-4 to identify correct *E* and *G* values. As shown in Table II, HCNW 1-4 resulted in a G_{COM} value ranging from 5.8 to 10.3 GPa with an average value of ~8 ±2 GPa.

HCNW No.	f_1 (kHz)	r (nm)	D (nm)	P (nm)	n	a (degree)	G_{COM} (GPa)	
							E= 200 GPa (υ)	E = 80 GPa (υ)
1	30	63.5	290	876	48.4	43.9	8.6 (10.63)	10.0 (3)
2	82	112	750	1116	24	Variable	5.8 (16.24)	6.2 (5.45)
3	56	103	330	1014	40	44.4	7.9 (11.66)	8.3 (3.82)
4	70	73	256	1187	29.5	55.9	6.2 (15.13)	10.3 (2.88)
						Avg. =	7.1	8.7
						Std. Dev. =	1.3	1.9

Table II: Observed resonant frequency f_1; dimensions r, D, p, n, α; and transverse shear modulus G_{COM} (and corresponding Poisson Ratios) calculated using E = 200 and E = 80 GPa for the HCNWs.[107]

The Poisson ratio(υ=E/2G-1) of HCNWs was found to be as high as 2.88 – 16.24 based on the values of G_{COM} shown in Table II suggesting that the HCNWs may be anisotropic *i.e.*, the elastic properties are different in the direction parallel and perpendicular to the axis, or that HCNWs are inhomogeneous.

5.4 Conclusion

We mechanically resonated HCNWs and studied their resonance modes using the HDR technique. Clearly the HDR electrical signals were found to inherently carry the signature of the excited resonance mode (circular vs planar) as seen under an SEM. We developed a model (based on experimental, analytical, and numerical methods) capable of predicting the first and the second transverse resonance modes applicable to any helically coiled cantilevers irrespective of their dimensions. Our experiments showed that HCNWs had a G ~8 ±2 GPa. The corresponding Poisson ratios suggested a possible anisotropy in the HCNWs. Resonating coiled nanostructures offers a possible method of probing shear modulus using transverse resonance based HDR method.

CHAPTER 6

SUMMARY AND FUTURE WORK

Nanoscale materials provide an excellent platform for the ingenious harness of many intriguing phenomena. In the past decade, nanomaterials have emerged as the scaffolds for many practical applications in energy generation/storage, environment, health, and information technology. Of interest to this work is the understanding and accurate determination of mechanical response of isolated low-dimensional nanomaterials using facile non-destructive techniques. In this regard, we have developed a new instrument *viz*., the twister explained in chapter 3 to determine the components of shear tensor in nanofibers. The twister is expected to fill a niche among the various methods used for evaluating shear behavior of emerging fibers, thus enabling greater access to the measurement of their fundamental properties and development of new and useful devices. While the present work focused on the design, construction, calibration, and automation of the twister, future efforts will be directed towards the determination of shear properties of carbon nanotube yarns.[147, 148] Previously, Baughman et al., have shown that a dense forest of vertically aligned CNT array can be spun in to yarns, scrolls, and bi-scrolls of different architectures. Such fibers are expected to exhibit a high degree of anisotropy and non-uniformity due to inter-tube interactions, slipping, and creep. The twister can be used to study such properties and play a pivotal role in rationally designing fiber compositions for use in medical implants and automobiles.

This work (chapters 4 and 5) underscores the importance of selecting the "appropriate" detection techniques that can probe mechanical properties of individual nanostructures without changing their properties. While the electronic and mechanical properties of nanostructures such as ZnO NWs are considerably modified in the presence of the electron beam, such effects may be used to intentionally induce defects and monitor their influence in real time providing us new ways to understand materials properties. We developed a new empirical protocol based on experimental data, analytical, and numerical modeling to study the mechanical properties and determine the elastic moduli of individual helically coiled "spring-like" nanostructures. As a part of the future work, the harmonic detection of resonance technique could be used to study: i) the internal friction between the walls of nanotubes (viz., double walled and multi-walled) by determining the inverse of *Q-factor* of the resonance as a function of pressure, and ii) the mechanical robustness of single-layer atom-thick "flatsheets" (e.g., graphene) for next generation electronics and resonators. Indeed, coupling these 2D resonators with electrical detection may lead to new limits of sensitivities in bio-sensing.

APPENDICES

Appendix A

Characterization of ZnO Nanowhiskers

Raman Spectroscopy: The Raman spectrum was obtained using the Ar+ ion laser excitation at 514.5 nm in a Dilor XY triple grating spectrometer equipped with TE cooled CCD. Our samples showed first-order modes at 379 cm^{-1} (A_1 (TO)), 580 cm^{-1} (E_1 (LO)), and 437.5 cm^{-1} (E_2) in addition to the second order peak at ~337 cm^{-1}.

X-ray diffraction: The X-ray diffractogram of our samples is in agreement with the standard JCPDS data for wurtzite ZnO (powder diffraction file #36-145).

Photoluminescence: The PL spectra were obtained using a JY-Horiba Nanolog equipped with Liq. N_2 cooled Triax 550 single grating spectrometer and Xe lamp.

Appendix B

HDR set up under a Scanning Electron Microscope

This custom made jig is capable of micro-manipulating the cantilever HCNW w.r.t the W-tip to a desired orientation. The piezocontrollers enable precise alignment in X,Y & Z directions.

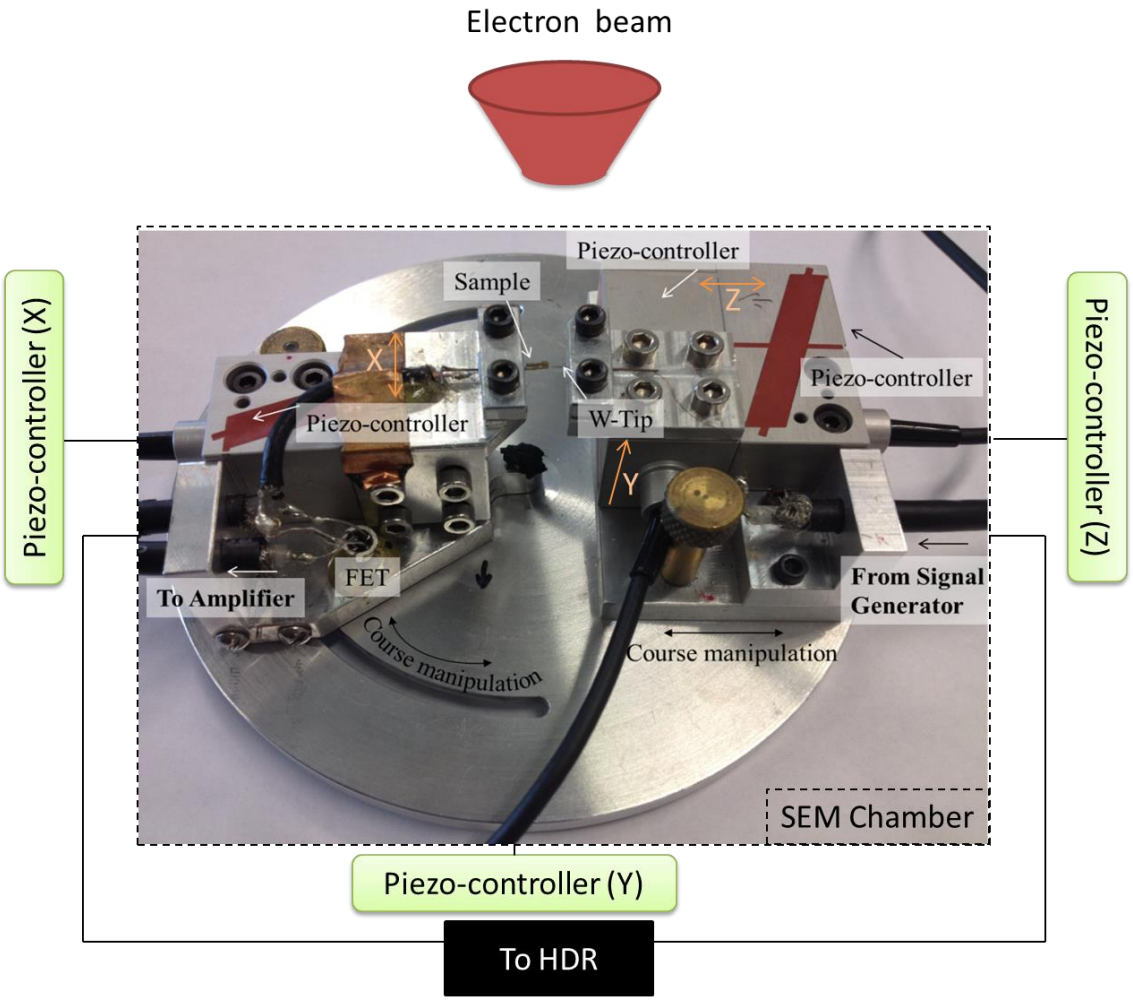

Figure B1: The jig used to hold the Cantilever-W Tip in the SEM. Voltages to the jig are controlled though the BNC connectors on the SEM chamber.

APPENDIX C

C.1 List of symbols used

Symbol	Description	Units
Q-factor	Quality factor	-
V_{ac}	AC voltage applied to Cantilever	V
V_{dc}	DC voltage applied to Cantilever	V
V_{net}	Total applied voltage	V
Ω	Driving frequency	Hz
ω	Angular Resonance frequency	rad/s
$\Delta\omega_{FWHM}$	Full width half maximum	Hz
E	Young's modulus	Pa
G	Shear modulus	Pa
ρ	Density	Kg/m^3
L	Length of cantilever	m
I	Moment of Inertia	Kgm^2
V_{out}	Output voltage of twister	V
f_1, f_2	First, second mode resonance frequency	Hz
r	Radius of the HCNW wire	m
D	Diameter of HCNW	m
p	Pitch of HCNW	m
n	Number of turns in HCNW	-
l	Length of HCNW	m
M	Moment experienced by one turn of HCNW	Nm
γ	Radius of curvature upon bending under M	m
α	Pitch angle of HCNW	radians
SBR	Signal-to-background-ratio	-

Note: $\omega=2\pi f$; For the sake of clarity, the terms ω and f are sometimes used interchangeably, depending on the context.

C.2 List of abbreviations

1. AFM: Atomic Force Microscopy
2. CE: counter Electrode
3. CE: Counter Electrode
4. CF: Carbon Fiber
5. CMOS: Complementary Metal-Oxide Semiconductor
6. CNT: Carbon Nanotube
7. CVD: Chemical Vapor Deposition
8. EB theory: Euler Bernoulli Theory
9. EOM: Equation of Motion
10. FIB: Focused Ion Beam
11. FIB: Focused Ion Beam
12. HCNW: Helically Coiled Nano Wire
13. HDR: Harmonic Detection of Resonance
14. (HR)TEM: (High Resolution) Transmission Electron Microscope
15. IC: Integrated Circuits
16. LDM: Low Dimensional Materials
17. MEMS: Micro Electromechanical System
18. MWCNT: Multi Walled Carbon Nanotube
19. NEMS: Nano Electromechanical System
20. NW: Nano Wires or Nano Whiskers
21. PSD: Position Sensitive Detector
22. PSD: Position Sensitive Detector
23. SEM: Scanning Electron Microscope
24. SWCNT: Single Walled Carbon Nanotube
25. W-tip: Tungsten tip

REFERENCES

1. Bogue, R., *MEMS sensors: past, present and future.* Sensor Review, 2007. **27**(1): p. 7-13.
2. Baltes, H., et al. *CMOS MEMS - present and future*. in *Micro Electro Mechanical Systems, 2002. The Fifteenth IEEE International Conference on*. 2002.
3. Senturia, S.D., *Perspectives on MEMS, past and future: The tortuous pathway from bright ideas to real products.* Boston Transducers'03: Digest of Technical Papers, Vols 1 and 2, 2003: p. 10-15.
4. Young, D., C. Zorman, and M. Mehregany, *MEMS/NEMS Devices and Applications*, in *Springer Handbook of Nanotechnology*, B. Bhushan, Editor 2004, Springer Berlin Heidelberg. p. 225-252.
5. Fu, Y., et al., *Fiber Supercapacitors Utilizing Pen Ink for Flexible/Wearable Energy Storage.* Advanced Materials, 2012. **24**(42): p. 5713-5718.
6. Jost, K., et al., *Knitted and screen printed carbon-fiber supercapacitors for applications in wearable electronics.* Energy & Environmental Science, 2013. **6**(9): p. 2698-2705.
7. Larsson, F. and L. Svensson, *Carbon, polyethylene and PBO hybrid fibre composites for structural lightweight armour.* Composites Part A: Applied Science and Manufacturing, 2002. **33**(2): p. 221-231.
8. Chand, S., *Review Carbon fibers for composites.* Journal of Materials Science, 2000. **35**(6): p. 1303-1313.
9. Rosentsveig, R. and R. Tenne. Available from: http://www.weizmann.ac.il/Chemical_Research_Support/EM_Unit/Ronit/current-activities.
10. Lingam, K., et al., *Evidence for Edge-State Photoluminescence in Graphene Quantum Dots.* Advanced Functional Materials, 2013. **23**(40): p. 5062-5065.
11. Koshino, M., et al., *Analysis of the reactivity and selectivity of fullerene dimerization reactions at the atomic level.* Nature Chemistry, 2010. **2**(2): p. 117-124.
12. Wang, W., et al., *Rational synthesis of helically coiled carbon nanowires and nanotubes through the use of tin and indium catalysts.* Advanced Materials, 2008. **20**(1): p. 179-+.
13. Wang, Z.L., *Nanostructures of zinc oxide.* Materials Today, 2004. **7**(6): p. 26-33.
14. Bandaru, P.R., et al., *Novel electrical switching behaviour and logic in carbon nanotube Y-junctions.* Nature Materials, 2005. **4**(9): p. 663-666.
15. Eda, G., et al., *Photoluminescence from Chemically Exfoliated MoS2.* Nano Letters, 2011. **11**(12): p. 5111-5116.
16. Gutiérrez, H.R., et al., *Extraordinary Room-Temperature Photoluminescence in Triangular WS2 Monolayers.* Nano Letters, 2012. **13**(8): p. 3447-3454.
17. Dresselhaus, M.S., et al., *Electronic, thermal and mechanical properties of carbon nanotubes.* Philosophical Transactions of the Royal Society a-Mathematical Physical and Engineering Sciences, 2004. **362**(1823): p. 2065-2098.

18. Dresselhaus, M.S., G. Dresselhaus, and P.C. Eklund, *Science of Fullerenes and Carbon Nanotubes*1996: Academic Press.
19. Morozov, S.V., et al., *Giant Intrinsic Carrier Mobilities in Graphene and Its Bilayer*. Physical Review Letters, 2008. **100**(1): p. 016602.
20. Cui, Y., et al., *High Performance Silicon Nanowire Field Effect Transistors.* Nano Letters, 2003. **3**(2): p. 149-152.
21. Li, P., Z. You, and T. Cui, *Graphene cantilever beams for nano switches.* Applied Physics Letters, 2012. **101**(9): p. -.
22. Liu, C., et al., *Graphene-Based Supercapacitor with an Ultrahigh Energy Density.* Nano Letters, 2010. **10**(12): p. 4863-4868.
23. Chang, S.P., et al., *A ZnO nanowire-based humidity sensor.* Superlattices and Microstructures, 2010. **47**(6): p. 772-778.
24. Lu, M.P., et al., *Piezoelectric Nanogenerator Using p-Type ZnO Nanowire Arrays.* Nano Letters, 2009. **9**(3): p. 1223-1227.
25. Cui, J.B., et al., *Carbon nanotube memory devices of high charge storage stability.* Applied Physics Letters, 2002. **81**(17): p. 3260-3262.
26. Nabar, B.P., Z. Celik-Butler, and D.P. Butler. *Self-powered, tactile pressure sensing skin using crystalline ZnO nanorod arrays for robotic applications*. in *Sensors, 2013 IEEE*. 2013.
27. Kranz, M.K., et al., *MEMS sensor suite on a chip*, 2010.
28. Mamin, H.J. and D. Rugar, *Sub-attonewton force detection at millikelvin temperatures.* Applied Physics Letters, 2001. **79**(20): p. 3358-3360.
29. Suijlen, M., et al., *MEMS pressure sensor*, 2011.
30. Hierlemann, A., *Integrated Chemical Microsensor Systems in CMOS Technology*. Microtechnology and MEMS, ed. H. Baltes, H. Fujita, and D. Liepmann2005: Springer.
31. Schilowitz, A.M. and D.G. Yablon, *Microcantilever stress sensor for fluid analysis*, 2010.
32. Schuh, W.C., *Dew point sensor using MEMS*, 2000.
33. Discenzo, F.M., *Lubricity measurement using mems sensor*, 2005.
34. Novotny, V.J., *Biosensor electronics*, 2012.
35. Voiculescu, I. and A.N. Nordin, *Acoustic wave based MEMS devices for biosensing applications.* Biosensors & Bioelectronics, 2012. **33**(1): p. 1-9.
36. Machauf, A., *Hydrogel-based mems biosensor*, 2009.
37. Kvisteroy, T., *Integrated Pedestal Mount for MEMS Structure*, 2007.
38. Hsiai, T.K., et al., *MEMS Vascular Sensor*, 2008.
39. Schnabel, C.M., et al., *Micro-electromechanical Sub-Assembly Having An On-Chip Transfer Mechanism*, 2010.
40. Casey, V., *Biomedical Interface Pressure Transducer for Medical Tourniquets*, 2012.
41. Yang, Y.T., et al., Nano Lett., 2006. **6**(4): p. 583.
42. Cao, G. and Y. Wang, *Nanostructures and Nanomaterials: Synthesis, Properties, and Applications*. 2nd ed. Vol. 2. 2011: World Scientific Publishing Co, Pte. Ltd.

43. Zande, A.M.v.d., et al., *Large-Scale Arrays of Single-Layer Graphene Resonators.* Nano Letters, 2010. **10**(12): p. 4869-4873.
44. Poncharal, P., et al., *Electrostatic Deflections and Electromechanical Resonances of Carbon Nanotubes.* Science, 1999. **283**(5407): p. 1513-1516.
45. Sazonova, V., et al., *A tunable carbon nanotube electromechanical oscillator.* Nature, 2004. **431**(7006): p. 284-287.
46. Knobel, R.G. and A.N. Cleland, *Nanometre-scale displacement sensing using a single electron transistor.* Nature, 2003. **424**(6946): p. 291-293.
47. Yu, M.F., et al., *Tensile loading of ropes of single wall carbon nanotubes and their mechanical properties.* Physical Review Letters, 2000. **84**(24): p. 5552-5555.
48. Wang, Z.L., et al., *In situ imaging of field emission from individual carbon nanotubes and their structural damage.* Applied Physics Letters, 2002. **80**(5): p. 856-858.
49. Gaillard, J., M. Skove, and A.M. Rao, *Mechanical properties of chemical vapor deposition-grown multiwalled carbon nanotubes.* Applied Physics Letters, 2005. **86**(23): p. 233109-233109-3.
50. Gröninger, M.A., M.J.V.D. Berg, and H.M.A. Wijshoff, *Inkjet system, method of making this system, and use of said system*, 2009.
51. Kuwajima, H. and K. Matsuoka, *Piezoelectric actuator and disk drive using the same*, 2008.
52. Augustine, B.H., S.H. Goodwin-Johansson, and L.N. Yadon, *Mems electrostatically actuated optical display device and associated arrays*.
53. DeReus, D.R., *Reduced voltage mems electrostatic actuation methods*, 2010.
54. Pantazi, A., et al., *High-speed electrostatic actuation of mems-based devices*, 2011.
55. Beeby, S., et al., *MEMS Mechanical Sensors*2004: Artech House, Inc.
56. Judy, J.W., R.S. Muller, and H.H. Zappe, *Magnetic microactuation of polysilicon flexure structures.* Journal of Microelectromechanical Systems, 1995. **4**(4): p. 162.
57. Papin, G., et al. *Optical actuation and detection of MEMS resonators: Behavioral modeling and phase noise simulations*. in *Frequency Control Symposium (FCS), 2012 IEEE International*. 2012.
58. Kolesar, E.S., *System and method for providing an improved electrothermal actuator for a micro-electro-mechanical device*, 2004.
59. Kawakatsu, H., *Homodyne laser interferometer probe and displacement measurement system using the same*, 2007.
60. Zeltzer, G., et al., *Scanning optical homodyne detection of high-frequency picoscale resonances in cantilever and tuning fork sensors.* Applied Physics Letters, 2007. **91**(17).
61. Kawakatsu, H., *Cantilever array, method of manufacturing the array, and scanning probe microscope, sliding device of guide and rotating mechanism, sensor, homodyne laser interferometer, and laser Doppler interferometer with specimen light excitation function, using the array and cantilever*, 2007.

62. Dandliker, R., S.M. Khanna, and J.F. Willemin, *Heterodyne interferometer*, 1989.
63. Molhave, K., A. setup, Editor 2006.
64. Su, Y., et al., *Characterization of a highly sensitive ultra-thin piezoresistive silicon cantilever probe and its application in gas flow velocity sensing.* Journal of Micromechanics and Microengineering, 2002. **12**(6): p. 780-785.
65. Arcamone, J. and E. Colinet, *Compensated micro/nano-resonator with improved capacitive detection and method for producing same*, 2013.
66. Blencowe, M.P. and M.N. Wybourne, *Sensitivity of a micromechanical displacement detector based on the radio-frequency single-electron transistor.* Applied Physics Letters, 2000. **77**(23): p. 3845.
67. Abbink, H.C., et al., *Method for optimizing direct wafer bond line width for reduction of parasitic capacitance in MEMS accelerometers*, 2011, Northrop Grumman Systems Corporation (Los Angeles, CA, US): United States.
68. Bertz, A., et al., *A single-crystal Si- resonator with on-chip readout amplifier in standard CMOS.* Sensors & Actuators: A. Physical, 2001. **93**(2): p. 163.
69. Zhu, J., *Pull-in instability of two opposing microcantilever arrays with different bending rigidities.* International Journal of Mechanical Sciences, 2008. **50**: p. 55.
70. Gaillard, J., et al., *Electrical detection of oscillations in microcantilevers and nanocantilevers.* Review of Scientific Instruments, 2006. **77**(7): p. 073907.
71. Saini., D., et al., *Harmonic Detection of Resonance: A Review.* Recent Patents on Materials Science, 2014. **7**(3): p. 173-194.
72. Scofield, J.H., *Frequency-Domain Description of a Lock-in Amplifier.* American Journal of Physics, 1994. **62**(2): p. 129-133.
73. Dickel, D., M.J. Skove, and A.M. Rao, *An analytic characterization of the harmonic detection of resonance method.* Journal of Applied Physics, 2009. **106**(4): p. 044515.
74. Tedesco, J.W., W.G. McDougal, and C.A. Ross, *Structural Dynamics Theory and Applications*. 1 ed1998: Prentice Hall.
75. Buchholdt, H.A., *Structural Dynamics for Engineers*. 1 ed1997: Thomas Telford Publications.
76. Davis, Z.J., et al., *Monolithic integration of mass sensing nano-cantilevers with CMOS circuitry.* Sensors and Actuators A: Physical, 2003. **105**(3): p. 311-319.
77. Isacsson, A., J.M. Kinaret, and R. Kaunisto, *Nonlinear resonance in a three-terminal carbon nanotube resonator.* Nanotechnology, 2007. **18**(19): p. 195203.
78. Zaitsev, S., et al. *Nonlinear dynamics in nanomechanical oscillators*. in *Proceedings of the 2005 International Conference on MEMS, NANO and Smart Systems*. 2005.
79. Pippard, A.B., *The Physics of Vibrations*. Vol. 1. 1978: Cambridge University Press.
80. Kozinsky, I., et al., *Tuning nonlinearity, dynamic range, and frequency of nanomechanical resonators.* Applied Physics Letters, 2006. **88**(25).
81. Postma, H.W.C., et al., *Dynamic range of nanotube- and nanowire-based electromechanical systems.* Applied Physics Letters, 2005. **86**(22).

82. Almog, R., et al., *Noise squeezing in a nanomechanical Duffing resonator.* Physical Review Letters, 2007. **98**(7).
83. De, S.K. and N.R. Aluru, *Full-Lagrangian schemes for dynamic analysis of electrostatic MEMS.* Microelectromechanical Systems, Journal of, 2004. **13**(5): p. 737-758.
84. Nayfeh, A.H. and D.T. Mook, *Nonlinear oscillations*. Pure and applied mathematics1979 New York: Wiley. xiv, 704 p.
85. Keskar, G., et al., *Ultra-Sensitive Duffing Behavior of a Microcantilever.* Ieee Sensors Journal, 2008. **8**(11-12): p. 1848-1855.
86. Elliott, B., et al., *Deconvolution of damping forces with a nonlinear microresonator.* Review of Scientific Instruments, 2011. **82**(5).
87. Behlow, J.H.W., et al., *Non-linear electrical actuation and detection*, 2013.
88. Rao, A.M., et al., *Diameter-selective Raman scattering from vibrational modes in carbon nanotubes.* Science, 1997. **275**(5297): p. 187-191.
89. Mamalis, A.G., *Recent advances in nanotechnology.* Journal of Materials Processing Technology, 2007. **181**(1–3): p. 52-58.
90. Daraio, C., et al., *Impact response by a foamlike forest of coiled carbon nanotubes.* Journal of Applied Physics, 2006. **100**(6).
91. Meric, I., et al., *Graphene field-effect transistors based on boron nitride gate dielectrics.* 2010 International Electron Devices Meeting - Technical Digest, 2010.
92. Happy, H., et al. *Graphene nano ribbon field effect transistor for high frequency applications*. in *Microwave Integrated Circuits Conference (EuMIC), 2011 European*. 2011.
93. Huntington, J., *Improving Satellite Protection with Nanotechnology.* Military Satellites: Issues, Goals and Challenges, 2009: p. 1-18.
94. Nye, J.F., *Physical Properties of Crystals: Their representation by Tensors and Matrices*: Oxford Science Publications.
95. Oliveira, L., et al., *Second- and Third-Order Elastic Constants of Filaments of HexTow® IM7 Carbon Fiber.* Journal of Materials Engineering and Performance, 2013: p. 1-8.
96. Qi, H.J., et al., *Determination of mechanical properties of carbon nanotubes and vertically aligned carbon nanotube forests using nanoindentation.* Journal of the Mechanics and Physics of Solids, 2003. **51**(11–12): p. 2213-2237.
97. Zhang, Y. and C. Pan, *Measurements of mechanical properties and number of layers of graphene from nano-indentation.* Diamond and Related Materials, 2012. **24**(0): p. 1-5.
98. Sohn, Y.S., et al., *Mechanical Properties of Silicon Nanowires.* Nanoscale Research Letters, 2010. **5**(1): p. 211-216.
99. Obitayo, W. and T. Liu, *A Review: Carbon Nanotube-Based Piezoresistive Strain Sensors.* Journal of Sensors, 2012. **2012**: p. 15.
100. Tanur, A.E., et al., *Diameter-Dependent Bending Modulus of Individual Multiwall Boron Nitride Nanotubes.* The Journal of Physical Chemistry B, 2012. **117**(16): p. 4618-4625.

101. Gouadec, G. and P. Colomban, *Raman Spectroscopy of nanomaterials: How spectra relate to disorder, particle size and mechanical properties.* Progress in Crystal Growth and Characterization of Materials, 2007. **53**(1): p. 1-56.
102. Ferralis, N., *Probing mechanical properties of graphene with Raman spectroscopy.* Journal of Materials Science, 2010. **45**(19): p. 5135-5149.
103. Zadler, B.J., et al., *Resonant Ultrasound Spectroscopy: theory and application.* Geophysical Journal International, 2004. **156**(1): p. 154-169.
104. Gao, R.P., et al., *Nanomechanics of individual carbon nanotubes from pyrolytically grown arrays.* Physical Review Letters, 2000. **85**(3): p. 622-625.
105. Behlow, H., et al., *Direct Measurement of Shear Properties of Microfibers.* (submitted), 2014.
106. Saini, D., et al., *Fundamental mechanism for electrically actuated mechanical resonances in ZnO nanowhiskers.* Physical Review B, 2012. **86**(20): p. 205312.
107. Saini, D., et al., *Mechanical Resonances of Helically Coiled Carbon Nanowires.* (submitted), 2014.
108. Adams, R.D. and D.H. Lloyd, *Apparatus for measuring the torsional modulus and damping of single carbon fibres.* Journal of Physics E: Scientific Instruments, 1975. **8**(6): p. 475-480.
109. Tsai, C.L. and I.M. Daniel, *Determination of shear modulus of single fibers.* Experimental Mechanics, 1999. **39**(4): p. 284-286.
110. Kawabata, S., *Micro-measurement of the Mechanical Properties of Single Fiber*, in *Modern Textile Characterization Methods*, M. Raheel and M. Dekker, Editors. 1996.
111. Available from: http://www.triprinceton.org/testing/hair-testing-services/torsion-twisting.
112. Wang, Z.L. and J.H. Song, *Piezoelectric nanogenerators based on zinc oxide nanowire arrays.* Science, 2006. **312**(5771): p. 242-246.
113. Wang, Z.L., *ZnO nanowire and nanobelt platform for nanotechnology.* Materials Science & Engineering R-Reports, 2009. **64**(3-4): p. 33-71.
114. Arnold, M.S., et al., *Field-effect transistors based on single semiconducting oxide nanobelts.* Journal of Physical Chemistry B, 2003. **107**(3): p. 659-663.
115. Wang, X.D., et al., *Piezoelectric field effect transistor and nanoforce sensor based on a single ZnO nanowire.* Nano Letters, 2006. **6**(12): p. 2768-2772.
116. Shibata, T., et al., *Characterization of sputtered ZnO thin film as sensor and actuator for diamond AFM probe.* Sensors and Actuators a-Physical, 2002. **102**(1-2): p. 106-113.
117. Huang, Y.H., X.D. Bai, and Y. Zhang, *In situ mechanical properties of individual ZnO nanowires and the mass measurement of nanoparticles.* Journal of Physics-Condensed Matter, 2006. **18**(15): p. L179-L184.
118. Ni, H. and X.D. Li, *Young's modulus of ZnO nanobelts measured using atomic force microscopy and nanoindentation techniques.* Nanotechnology, 2006. **17**(14): p. 3591-3597.
119. Hoffmann, S., et al., *Fracture strength and Young's modulus of ZnO nanowires.* Nanotechnology, 2007. **18**(20).

120. Chen, C.Q., et al., *Size Dependence of Young's Modulus in ZnO Nanowires.* Physical Review Letters, 2006. **96**(7): p. 075505.
121. Zhang, Q., et al., *Diameter-dependent internal gain in ZnO micro/nanowires under electron beam irradiation.* Nanoscale, 2011. **3**(8): p. 3060-3063.
122. Ji, H., et al., *Electron beam tuning of carrier concentrations in oxide nanowires.* Journal of Applied Physics, 2011. **110**(1).
123. Joo-han, C., et al., *Nano-Elastic Memory Device and Method of Manufcturing the Same*, S.E.C. Ltd, Editor 2010.
124. Xu, F., W. Lu, and Y. Zhu, *Controlled 3D Buckling of Silicon Nanowires for Stretchable Electronics.* Acs Nano, 2010. **5**(1): p. 672-678.
125. Faraby, H.M., A.M. Rao, and P.R. Bandaru, *Modeling High Energy Density Electrical Inductors Operating at THz Frequencies Based on Coiled Carbon Nanotubes.* Ieee Electron Device Letters, 2013. **34**(6): p. 807-809.
126. Chen, X., et al., *Mechanics of a Carbon Nanocoil.* Nano Letters, 2003. **3**(9): p. 1299-1304.
127. Poggi, M.A., et al., *Measuring the Compression of a Carbon Nanospring.* Nano Letters, 2004. **4**(6): p. 1009-1016.
128. Volodin, A., et al., *Imaging the elastic properties of coiled carbon nanotubes with atomic force microscopy.* Physical Review Letters, 2000. **84**(15): p. 3342-3345.
129. Volodin, A., et al., *AFM detection of the mechanical resonances of coiled carbon nanotubes.* Applied Physics A, 2001. **72**(1): p. S75-S78.
130. Volodin, A., et al., *Coiled Carbon Nanotubes as Self-Sensing Mechanical Resonators.* Nano Letters, 2004. **4**(9): p. 1775-1779.
131. Love, A.E.M., *The propagation of waves of elastic displacement along a helical wire*. Transactions of the Cambridge Philosophical Society. Vol. 18. 1899.
132. Lee, J. and D.J. Thompson, *DYNAMIC STIFFNESS FORMULATION, FREE VIBRATION AND WAVE MOTION OF HELICAL SPRINGS.* Journal of Sound and Vibration, 2001. **239**(2): p. 297-320.
133. Sato, S., et al., *Resonant vibration of cantilevered carbon nanocoil.* Microprocesses and Nanotechnology 2007, Digest of Papers, 2007: p. 468-469.
134. Taylor, J.D., et al., *Harmonic Detection of Resonance methods for micro- and nano cantilevers:Theory and selected applications*, in *The Oxford Handbook of Nanoscience and Technology*, A.V. Narlikar and Y.Y. Fu, Editors. 2010, Oxford University Press: New York. p. 249-284.
135. Adams, R.D., *The dynamic longitudinal shear modulus and damping of carbon fibres.* Journal of Physics D: Applied Physics, 1975. **8**(7): p. 738-748.
136. McAllister, Q.P., J.W. Gillespie, and M.R. VanLandingham, *Evaluation of the three-dimensional properties of Kevlar across length scales.* Journal of Materials Research, 2012. **27**(14): p. 1824-1837.
137. Podila, R., et al., *Evidence for surface states in pristine and Co-doped ZnO nanostructures: magnetization and nonlinear optical studies.* Nanotechnology, 2011. **22**(9).

138. Shi, Y., et al., *Determination of the natural frequency of a cantilevered ZnO nanowire resonantly excited by a sinusoidal electric field.* Nanotechnology, 2007. **18**(7).
139. Keskar, G., et al., *Ultra-Sensitive Duffing Behavior of a Microcantilever.* Ieee Sensors Journal, 2008. **8**(11-12): p. 1848-1855.
140. Goldstein, J., *Scanning electron microscopy and x-ray microanalysis*. 3rd ed2003, New York: Kluwer Academic/Plenum Publishers. xix, 689 p.
141. Keskar, G., et al., *Ultra-Sensitive Duffing Behavior of a Microcantilever.* Sensors Journal, IEEE, 2008. **8**(11): p. 1848-1855.
142. Gaillard, J., M. Skove, and A.M. Rao, *Mechanical properties of chemical vapor deposition-grown multiwalled carbon nanotubes.* Applied Physics Letters, 2005. **86**(23): p. 233109.
143. Younis, M.I., *MEMS Linear and Nonlinear Statics and Dynamics.* Mems Linear and Nonlinear Statics and Dynamics, 2011: p. 107-108.
144. Wahl, A.M., *Mechanical Springs*1963: McGraw-Hill Book Company.
145. Perisanu, S., et al., *Beyond the linear and Duffing regimes in nanomechanics: Circularly polarized mechanical resonances of nanocantilevers.* Physical Review B, 2010. **81**(16): p. 165440.
146. Villanueva, L.G., et al., *Nonlinearity in nanomechanical cantilevers.* Physical Review B, 2013. **87**(2).
147. Chun, K.Y., et al., *Hybrid carbon nanotube yarn artificial muscle inspired by spider dragline silk.* Nature Communications, 2014. **5**.
148. Zhang, M., K.R. Atkinson, and R.H. Baughman, *Multifunctional carbon nanotube yarns by downsizing an ancient technology.* Science, 2004. **306**(5700): p. 1358-1361.